

Non-equilibrium Phase Transitions and Steady States in Biased Diffusion of Two Species

György Korniss

Dissertation submitted to the Faculty of the
Virginia Polytechnic Institute and State University
in partial fulfillment of the requirements for the degree of

Doctor of Philosophy
in
Physics

Beate Schmittmann, Chair
James R. Heflin
Guy J. Indebetouw
Clayton D. Williams
Royce K. P. Zia

April 21, 1997
Blacksburg, Virginia

Keywords: driven lattice gas, order-disorder transition, Monte Carlo simulations, continuum field theory

Non-equilibrium Phase Transitions and Steady States in Biased Diffusion of Two Species

György Korniss

Committee Chairman: Beate Schmittmann

Physics

(ABSTRACT)

We investigate the dynamics of a three-state stochastic lattice gas, consisting of holes and two oppositely “charged” species of particles, under the influence of an “electric” field, at zero total charge. Interacting only through an excluded volume constraint, particles can hop to nearest neighbor empty sites, but particle-particle exchange between oppositely charged particles is also allowed on a separate time scale. Controlled by this relative time scale, particle density and drive, the system orders into a charge-segregated state. Using a combination of Monte Carlo simulations and continuum field theory techniques, we study the order of these transitions and map out the steady state phase diagram of the system. On a single sheet of transitions, a line of multicritical points is found, separating the first order and continuous transitions. Furthermore, we study the steady-state structure factors in the *disordered* phase where homogeneous configurations are stable against small harmonic perturbations. The *average* structure factors show a discontinuity singularity at the origin which in real space predicts an intricate crossover between power laws of different kinds. We also seek for generic statistical properties of these quantities. The probability distributions of the structure factors are *universal* asymmetric exponential distributions.

This research was supported in part by grants from the National Science Foundation through the Division of Materials Research.

To my Family, Friends and Ildi

Acknowledgments

First of all, I would like to express my special thanks to my Ph.D. thesis advisor Prof. Beate Schmittmann. Besides introducing me into the field of non-equilibrium systems, she provided me with her friendship, encouragement, and permanent moral and financial support, throughout the years of my graduate studies. For the same reasons, I am also deeply indebted to Prof. Royce Zia. I should not pass without mentioning the numerous discussions with both of them, that I greatly benefited from. Thanks to Beate and Royce, I was able to enjoy a creative and fruitful working environment.

I would like to express my appreciation toward the efforts made by Prof. Lay Nam Chang, since he has been the Chair of the Physics Department. It has been impossible not to notice the changes that effected the lifes of graduate students in the most positive manner.

I also thank to my Diploma thesis advisor, Prof. Jenő Sólyom, for maintaining his friendship, support and interest in my progress, from overseas.

I would like to thank Prof. Zoltán Rácz and his family, for helping me through the first (and probably the most difficult) year of mine here at Virginia Tech. I greatly appreciate his constant interest toward my life and research, despite of the physical distance now between us. I am also proud, that the tradition of the Saturday afternoon soccer games, of which he was one of the founders here, did not die out, but has only improved in the past three years, since he left.

I thank my friend and coworker, Zoltán Toroczka, for his constant interest in my work and for simply making life more fun.

I deeply appreciate the efforts of the Department's Computer Systems Manager, Roger Link, who has always, sometimes despite of all odds, managed to keep us on-line.

I am indebted to Chris Thomas, Cindy Davis, Barbara Day, as well as the Department's other secretaries, for assisting me in all kinds of matters, typical of graduate students'.

Finally, I thank my family, friends and Ildi for their love and constant support so that despite being far away from home, we could still share what we had done before.

Contents

1	Introduction	1
1.1	The Standard Model	3
1.2	Multi-species Models	4
1.2.1	The Polarized Lattice Gas	4
1.2.2	Biased Diffusion of Two Species	5
1.3	Overview of the Dissertation	7
2	Observables and Phase Diagram of the Two Species Model	8
2.1	The Microscopic Model and Order Parameters	8
2.2	Monte Carlo Results	13
2.2.1	Order Parameters, Currents and Histograms	14
2.2.2	Density Profiles in the Ordered Phase	22
2.3	Mean-field Theory	24
2.3.1	Equations of Motion	25
2.3.2	Homogeneous and Inhomogeneous Solutions	28
2.3.3	Linear Stability Analysis	32
2.3.4	Adiabatic Elimination of the Fast Modes	34
2.3.5	Conductivity Near the Continuous Transitions	38
2.4	Summary	40
3	The Ω-expansion for the Two Species	42
3.1	Expansion of the Master Equation	42
3.1.1	Mean-field Equations of Motion	46
3.1.2	The Fokker-Planck Equation	47
3.2	The Associated Langevin Equations	48
3.3	Some General Remarks	50
4	Structure Factors and Correlations in the Disordered Phase	52
4.1	Microscopic Observables and Histograms	53

4.2	Exact Results at Zero Field	55
4.3	Coarse-grained Description	60
4.3.1	Steady-state structure factors	63
4.3.2	Equal-time spatial correlations	65
4.3.3	The $\gamma = 1$ case	68
4.3.4	Distribution of structure factors	69
4.4	Discussion	72
5	Summary and Outlook	76
A	Typical Fortran Source Code for the Simulations	83
B	Momentum-space Integrals for the Correlation Functions	93
B.1	A Formal Way	93
B.2	A Rigorous Way	95
C	Long Distance Asymptotic Behavior of the Correlation Functions	97
D	A Special Determinant	100
Vita		102

List of Figures

2.1	Ordered and Disordered Configurations	12
2.2	Monte Carlo Phase Diagram	14
2.3	Observables Near the First Order Transition	15
2.4	Time Trace and Histogram Near the First Order Transition	16
2.5	Observables Near the Continuous Transition	17
2.6	Histograms Near the Continuous Transition	18
2.7	Fast and Slow Modes Near the Continuous Transition	19
2.8	Observables Near the Continuous Transition for different L_{\perp}	20
2.9	Observables Near the Continuous Transition for different L_{\parallel}	21
2.10	Critical Exponent for the Order Parameter	22
2.11	Observables Near the Continuous Transition as Varying γ	23
2.12	Characteristic Profiles in the Ordered Phase	24
2.13	Simulation Profiles vs. Discrete Equation of Motion	29
2.14	Mean-field Linear Stability Boundary of the Homogeneous Phase	34
4.1	Zero Field Structure Factors	56
4.2	Structure Factors for $\gamma = 0.02$	57
4.3	Structure Factors for $\gamma = 1$	58
4.4	Structure Factor Time Series for $\mathbf{k} = \frac{2\pi}{L}(0, 1)$	59
4.5	Structure Factor Time Series for $\mathbf{k} = \frac{2\pi}{L}(1, 0)$	60
4.6	Structure Factor Histograms for $\mathbf{k} = \frac{2\pi}{L}(0, 1)$	61
4.7	Structure Factor Histograms for $\mathbf{k} = \frac{2\pi}{L}(1, 0)$	62

List of Tables

2.1	Mapping the Parameters of the Numerical Profiles onto Simulation Ones	32
4.1	Fit Parameters for the Structure Factors at $\gamma = 0.02$	72
4.2	Fit Parameters for the Structure Factors at $\gamma = 1$	73
4.3	Calculated Decay Factors of the Theoretical Distributions for $\mathbf{k} = \frac{2\pi}{L}(0, 1)$	74
4.4	Calculated Decay Factors of the Theoretical Distributions for $\mathbf{k} = \frac{2\pi}{L}(1, 0)$	74

Chapter 1

Introduction

In nature, equilibrium systems are exceptions rather than a rule; non-equilibrium phenomena are overwhelmingly more common in real systems of interest not only to physics, but to materials science, chemistry, biology and economics as well. When studying systems in thermal equilibrium, one can always utilize the framework provided by Gibbs [1], namely, once the microscopic Hamiltonian, \mathcal{H} , of the system is specified, averages of time-independent observables can be computed, at least in principle. For example, in the canonical ensemble where the system is coupled only to a heat bath, the stationary probability distribution is just the Boltzmann factor $e^{-\beta\mathcal{H}}$, up to normalization. On the other hand, in non-equilibrium systems the generically time-dependent probability distribution is not known to start with, but is rather the solution of the associated master equation, which is often hard or impossible to find exactly.

In analogy with equilibrium systems and as a first step to study nonequilibrium ones, one can study systems which have reached a non-equilibrium steady-state (NESS), where the distribution is time-independent but still non-Hamiltonian and there is no equivalent of Gibbs measures. Thus, there still remains the fundamental problem of finding the stationary distribution, which typically cannot be expressed in terms of the internal energies of the system. One can then start with a master equation of the model

$$\partial_t P[t, C] = \sum_{C'} \{W(C' \rightarrow C) P[t, C'] - W(C \rightarrow C') P[t, C]\} \quad (1.1)$$

and look for time-independent solutions. Here $P[t, C]$ is the probability of finding the system in configuration C at time t with a given initial condition. The microscopic dynamics is specified by the transition rates $W(C \rightarrow C')$. It is quite transparent that (1.1) is nothing but a balance equation. The first sum on the right hand side represents the “gain” terms, i.e., summing over all configurations from which configuration C could possibly result. Similarly, the terms with the minus sign are the “loss” terms, containing all possibilities how the system can leave configuration C . Then the NESS is fully described

by $P^*[C] = P[t \rightarrow \infty, C]$ at the microscopic level. When modeling systems in equilibrium, we have to ensure that $P^*[C] = P_{\text{eq}}[C]$, which can be most conveniently imposed in the form of detailed balance:

$$\frac{W(C' \rightarrow C)}{W(C \rightarrow C')} = \frac{P_{\text{eq}}[C]}{P_{\text{eq}}[C']} = \exp(\beta\Delta\mathcal{H}) , \quad (1.2)$$

where $\Delta\mathcal{H} = \mathcal{H}[C'] - \mathcal{H}[C]$. For modeling NESS, there is no such constraint. Further, to obtain a stationary solution of the master equation, does not require that each term of the sum in (1.1) yields zero by pair-wise cancellation of the probability currents between configurations. In fact, for the majority of NESS, there is a non-vanishing uniform “current” in the configuration space.

Much work has been done on systems which are weakly perturbed so that they remain close to equilibrium. The behavior of these systems can be well understood within the framework of linear response theory [2], which is essentially based on Gibbs measures. In this dissertation we will rather focus on systems *far from equilibrium*, for which these well known approaches break down.

To understand collective behavior in many-particle systems, it is extremely important to build simple models which have relevance to real systems and capture the essence of the physics involved. Studying even very simple model systems can provide us with important pieces of information on real physical systems. Motivated by these reasons, Lenz introduced the Ising model [3] in 1925, to investigate phase transitions in ferromagnets. The most important questions to be answered were: how short range microscopic interactions result in long range order and how a perfectly analytic microscopic Hamiltonian can exhibit truly non-analytic behavior at a critical temperature, where the phase transition occurs. The reason why the Ising model has become the most fundamental one in statistical mechanics in this century, is because it turned out to be exactly solvable. Onsager [4] in 1944 managed to carry out an analytic solution to this problem in two dimensions and in zero external field and indeed demonstrated how the model exhibits a phase transition displayed as a non-analytic behavior in the thermodynamic functions at the critical point. From this point on the Ising model has served as a test ground and benchmark for new techniques and approximations. The most remarkable one was clearly the modern theory of critical phenomena and the renormalization group (RG) [5] in the late 60’s and early 70’s. This powerful technique was developed to “deal” with infinitely many degrees of freedom near and at the critical temperature as a result of a diverging length scale (correlation length). It illustrates how apparently different microscopic models result in the same effective (coarse-grained) Hamiltonian near the critical point and provides a systematic way to compute critical exponents for the thermodynamic functions. Also, with more and more powerful computers on the rise, another method has become widespread in statistical physics: the Monte Carlo simulations. Its dependability and how to take finite size effects into account

were extensively tested on the Ising model (see e.g. [6]). It is clear, that even with today's computers, one cannot study realistic system sizes ($\mathcal{O}(10^{23})$ particles). However, with appropriate finite size scaling, the relevant physical behavior can be extracted and it is no surprise that simulations have become one of the most important investigative tools for many-particle systems.

1.1 The Standard Model

Following the above spirit to build a correct “minimal” non-equilibrium model, Katz, Lebowitz and Spohn [7] in 1983 introduced the *driven* Ising lattice gas as the “standard model” for studying NESS. In the lattice gas representation, each site can be empty or occupied by a single particle. In addition to this excluded volume constraint, the particles also interact via nearest neighbor Ising interaction, thus the internal energy of the system takes the form

$$\mathcal{H} = -J \sum_{\text{n.n.}} n_i n_j , \quad (1.3)$$

where $n_i = 0, 1$ is the occupation number on site i and the summation runs over nearest neighbor pairs on the lattice. $J > 0$ represents an attractive interaction. Subject to *periodic boundary conditions* and in addition to a nearest neighbor attractive interaction, particles respond to an external, *uniform* electric field E . The role of the external drive is to bias hopping rates along a particular direction on the lattice. Particle-hole exchanges follow the (conserved) Kawasaki dynamics [8] with the Metropolis rates [9]:

$$W_{ph} = \min \{1, \exp[-\beta(\Delta\mathcal{H} - E\Delta y)]\} , \quad (1.4)$$

where $\Delta\mathcal{H}$ is the change of the internal energy of the system and Δy is the change of the coordinate of the particle, parallel to the field, due to the jump. On a finite lattice, the system reaches a particle current carrying NESS. Since the system is not only coupled to a heat bath but also to an external field, there is a steady-state energy current through the system as well. Through Monte Carlo Simulation, this system (at half filling) was shown to undergo a continuous transition, at a field dependent critical temperature, from a disordered to a phase-segregated steady-state configuration. Theoretical understanding of these results is severely limited by the lack of Boltzmann-like factors which describe such stationary, but non-equilibrium states. Nevertheless, *dynamic* field theoretic RG techniques [10] can be applied so that the critical properties associated with the continuous transition can be computed. The fixed point is non-Hamiltonian and is best displayed as a dynamic functional [11]. A number of the critical exponents, distinct from those in the Ising universality class, are confirmed by simulations [12]. Also, the system exhibits generic long range spatial correlations *at all temperatures* above criticality [13] which are not associated with

a divergent correlation length, but rather the breakdown of the traditional fluctuation-dissipation theorem (FDT) [14]. A recent review of this early model, as well as the multitude of variations, can be found in [15]. Experimental motivations for studying this model came from the physics of fast ionic conductors [16] where one or more species of ions have higher mobility as a result of a large number of interstitial lattice sites. Here the signal of the order-disorder transition is an abrupt increase in the conductivity. It should be noted, that in most experimental situations so far, data were taken at small external fields, where linear response theory would be an adequate framework for theoretical investigations. Setting up large fields for superionic conductors would fall out of the experimentally accessible regime. Also, most of the novel features of the model occur when the nearest neighbor interaction is attractive, while this is not the case for some of the solid electrolytes. Nevertheless, during the past decade, the standard model played the role of a proto model to describe systems far from equilibrium, due to its simplicity and numerous generic non-equilibrium features.

1.2 Multi-species Models

One natural generalization of the standard model is a lattice gas of more than one species of particles. The motivations come from both theoretical interests and real physical systems. We start with listing some of the latter. There are certain ionic conductors, where two different mobile ion species are present and act as charge carriers [17]. Also, water-in-oil microemulsions, with small droplets carrying electric charges, typically given by $\pm e$ [18] can be considered as a multi-species system. The dynamics of polymer chains [19], in the process called gel electrophoresis (to separate e.g. DNA fragments by molecular weight [20]), can be mapped onto a driven lattice gas with two charged species [21]. Finally, modeling traffic flow [22] is often related to multi-species systems, e.g., species with different jump rates can be interpreted as cars moving with different velocities. From a theoretical viewpoint, anticipating drastically changed behavior if the symmetry of the stochastic variable is modified, it is of great interest to study the effects of external drives on not just the Ising model, but on models with rich equilibrium phase structures, e.g. Potts [23], Blume-Emery-Griffiths [24], etc. To begin with, one can think of a lattice where the sites can be occupied by particles of two different species, subject to excluded volume constraint. Since the sites can also be empty, this system is effectively a three state lattice gas.

1.2.1 The Polarized Lattice Gas

In this subsection we discuss a three dimensional Monte Carlo simulation by Aertsens *et al.* [25] of the polarized lattice gas which is to model water-in-oil microemulsions, already mentioned in the above examples. The model consists of two species of particles which are referred to as \pm charges. Regardless of their charges, they interact via the usual nearest

neighbor attractive Ising interaction. Particles can jump to nearest and *next nearest* neighbor empty sites and the jump probabilities against the field are exponentially suppressed, following the usual Metropolis rates [9]. In addition to the above particle-hole exchange, nearest and next nearest neighbor opposite charges are also allowed to exchange, again with exponentially suppressed jump rates against the force. In particular, after each attempt for a particle-hole exchange, the charge exchange algorithm is performed $N \geq 1$ times, to account for the experimental observation, that charge exchange takes place on a faster time scale than diffusion. This new mechanism strongly reduces the excluded volume constraint. In real microemulsions neutral particles also do occur, but in the above model they are not allowed, thus creation and annihilation of charges cannot occur.

Now we briefly discuss the steady-state phase diagram of the polarized lattice gas. At high temperatures, the system is disordered. As one reduces the temperature at small electric fields, the particles gather into compact clusters. Within these clusters, the charge exchange mechanism causes the segregation of opposite charges, leading to the polarization of these droplets. As long as the field is low, the nearest neighbor attractive interaction dominates, preventing the break-up of the droplets. With increasing electric fields, clusters begin to stretch as result of biased hopping rates, until the elongated clusters span the whole system parallel to the field. Also, when in this phase, the current is significantly greater than in the previous two cases, by virtue of the charge exchange mechanism. Within the spanning clusters, charges are distributed homogeneously. If the field is increased further, the possibility of next nearest neighbor jumps along the “downstream” lattice diagonals causes the clusters to break up (random stirring in the transverse direction) and the system disorders again. The order of this latter transition is suspected to be first order, indicated by a sharp change in the nearest neighbor correlations and the current.

The three dimensional simulation of the polarized lattice gas may provide a realistic model for microemulsions, but as a result of its relative complexity, it is more difficult to extract generic physical properties.

1.2.2 Biased Diffusion of Two Species

Now we introduce the model most closely related to the one that we will study in this dissertation. We will follow the path of building the simplest two-species model which exhibits generic non-equilibrium behavior, possibly including phase transitions and criticality.

Schmittmann *et al.* [26], in 1992, proposed the simplest “generalization” of the standard model. They considered a fully periodic two dimensional $L_x \times L_y$ lattice, where each site can be empty or occupied by either a positive or a negative particle. Thus, it is natural to define two occupation variables for each site, $n_{\mathbf{x}}^+$ and $n_{\mathbf{x}}^-$, with n being 0 or 1, depending on whether a positive or a negative particle is present at site \mathbf{x} . Opposite charges are driven into opposite directions by a uniform external field, E , which points in the $+y$ direction.

However, there are *no* interparticle interactions, apart from the excluded volume constraint. Thus the rate of the particle-hole exchange takes the simple form:

$$W_{ph} = \min \{1, \exp(qE\Delta y)\} , \quad (1.5)$$

where q is the charge of the particle attempting a jump which would cause a change Δy in its coordinate, parallel to the field. Also note that the inverse temperature β has been absorbed into E . Thus, this system may be interpreted as the large field, high temperature limit ($E \rightarrow \infty, T \rightarrow \infty$), with fixed E/T , of a more complicated interacting one. With equal number of +’s and -’s this system reaches a stationary steady state. Monte Carlo simulations in two dimensions [26, 27] and mean-field studies [26, 27, 28] show that there is a transition, controlled by overall (average) particle density and drive, from a spatially homogeneous (disordered) phase to a charge segregated one, where the excluded volume constraint leads to the mutual blocking of particles. The charges gather into a single strip, transverse to the field, while the rest of the lattice remains essentially empty. With E pointing in the $+y$ direction, the lower (upper) half of the particle strip is mainly occupied by positive (negative) particles. Also, as a result of having very few holes in the compact particle strip, the current drops dramatically in the ordered phase. When studying the transition, in addition to the current, an appropriate order parameter was defined, to signal the onset of inhomogeneities:

$$Q = \left\langle \frac{1}{L_y} \sum_y \left[\frac{1}{L_x} \sum_x (n_{\mathbf{x}}^+ - n_{\mathbf{x}}^-) \right]^2 \right\rangle . \quad (1.6)$$

Note that the quantity in the straight brackets is just the charge density profile of a given configuration as function of y . Up to finite size effects, Q is zero in the disordered phase and increases characteristically when inhomogeneous profiles develop.

Extensive simulations were performed with overall particle densities below 0.70, and indicated a line of first order transition in the density-field parameter space. On the other hand, a mean-field analysis [28] suggested that the first order transition crosses over to a continuous one for small fields and high densities, through a possible “tricritical” point. The absence of the line of continuous transitions in the simulations can be accounted for as follows: as we shall see later in Chapter 1, Q serves as a good order parameter in signaling discontinuous transitions but may not be sensitive enough to the onset of continuous transitions (i.e. to small amplitude, long wavelength harmonic density fluctuations). Also, the mean-field theory predicts this crossover at higher densities, where it is increasingly difficult to simulate the system, due to the frozen dynamics when only a small number of holes are present.

We have not mentioned so far that the structure of the ordered phase can differ significantly from the one described above, when the aspect ratio of the system is varied. In

particular, for $L_x/L_y > 1$, Bassler *et al.* [29] discovered that although strips transverse to the field are still found, the system also often orders into a *tilted* strip with non-zero integer winding number by virtue of periodic boundary conditions. The continuum mean-field equations of the model also allow for this type of solution, in agreement with simulations.

To generalize the above two species model, we can allow particles to exchange among themselves. Since we have interpreted the action of the drive on the particles as an external electric field on oppositely “charged” particles, we may refer to this new process as “charge exchange”. In particular, we will introduce the ratio γ , which is the overall rate of charge exchanges relative to particle-hole exchanges. To model ions of different species [17], γ should be vanishingly small. On the other hand, to model charged water droplets, as in the polarized lattice gas [25], we are obligated to let γ be large, since charges move between droplets much faster than the droplets diffuse. Since we restrict ourselves to the non-interacting case, we do not expect any interesting phase transitions in the large γ limit where the charge exchange mechanism completely dominates over the mutual blocking of opposite species. Therefore, we will explore the $0 < \gamma \leq 1$ regime [31]. Note, however, that even for larger γ , the system may display anomalous diffusion [30] and generic long range correlations.

We should mention that in one dimension the steady state distribution of this model is known analytically [32, 33]. It was shown that the steady state is always disordered: although there are particle clusters in the system, their typical length does not scale with the system size, thus no long range order results [33]. Further, a similar system with *open boundaries* displays the unexpected phenomenon of spontaneous symmetry breaking even in one spatial dimension [34]. Our interest focuses on higher dimensions, in which richer critical phenomena typically take place.

1.3 Overview of the Dissertation

We finish the Introduction by outlining the remainder of this Dissertation. In Chapter 2, we define in detail the microscopic model of biased diffusion of two species with charge exchange. Focusing on “phenomenology” first, we try to find the appropriate order parameters, explore the phase diagram of the system and investigate the nature of phase transitions. We present the results of the Monte Carlo simulations and compare those to the findings of a simple mean-field theory. In Chapter 3, we provide a systematic way to arrive at the “coarse-grained description” of the model. This will be done by using a general framework, called the Ω -expansion. Then, in Chapter 4, using the resulting Langevin equations, we will study structure factors and correlations in the disordered phase of the model and compare those to simulation results. Chapter 5 is devoted to a brief summary of our work and possible extensions of future research.

Chapter 2

Observables and Phase Diagram of the Two Species Model

In this Chapter we define the microscopic model and give some details of the Monte Carlo simulations. We will report the main simulation results: the extension of the density-field phase diagram in Ref. [26] to a third dimension, spanned by γ . Theoretical understanding of the shape and nature of the order-disorder phase boundary will also be achieved within a mean-field approach.

2.1 The Microscopic Model and Order Parameters

We consider a two dimensional fully *periodic* lattice with $L_{\perp} \times L_{\parallel}$ sites, each of which can be empty or occupied by either a positive or a negative particle. Therefore we define two occupation variables, $n_{\mathbf{x}}^{+}$ and $n_{\mathbf{x}}^{-}$, in the usual way, i.e.,

$$\begin{aligned} n_{\mathbf{x}}^{+} &= \begin{cases} 1 & \text{if site } \mathbf{x} \text{ is occupied by a positive particle} \\ 0 & \text{otherwise} \end{cases} \\ n_{\mathbf{x}}^{-} &= \begin{cases} 1 & \text{if site } \mathbf{x} \text{ is occupied by a negative particle} \\ 0 & \text{otherwise} \end{cases} \end{aligned} \quad , \quad (2.1)$$

with the constraint $n_{\mathbf{x}}^{+}n_{\mathbf{x}}^{-} = 0$, and $\mathbf{x} = (x, y)$ represents discrete lattice sites in two dimensions. Our model is “non-interacting” in the sense that, apart from the excluded volume constraint, there are no other interparticle interactions. In particular, though we refer to these particles as “charged” ones, they do not interact via the Coulomb potential. Instead, they are coupled to a uniform external “electric” field, E , directed along the y axis. We restrict ourselves to zero total charge

$$\sum_{\mathbf{x}} [n_{\mathbf{x}}^{+} - n_{\mathbf{x}}^{-}] = 0 \quad , \quad (2.2)$$

i.e., the total number of +’s and –’s are the same.

The dynamics consists of two processes: particle-hole and particle-particle exchanges. In the absence of the drive, it does not distinguish between different species. Both types hop randomly to a nearest neighbor empty site with rate Γ . In addition, if a nearest neighbor site is occupied by an oppositely charged particle, they may exchange with rate $\gamma\Gamma$. Since charge is the only attribute of the particles, the latter process is also referred to as “charge exchange”. In the presence of the field, the rates of moving against the “force” will be suppressed exponentially.

During one Monte Carlo step, $L_{\perp}L_{\parallel}$ nearest neighbor bonds are chosen randomly, and their contents are updated according to the following rules:

(i.) If one site is occupied and the other is empty, a particle-hole exchange occurs with rate:

$$W_{ph} = \Gamma \min\{1, \exp(qE \Delta y)\} , \quad (2.3)$$

where $q = \pm 1$ is the charge of the particle and $\Delta y = 0, \pm 1$ is the change in the y coordinate of the particle due to the jump.

(ii.) If the two sites are occupied by opposite charges, a particle-particle exchange (or, charge transfer) is attempted with the rate:

$$W_{pp} = \gamma\Gamma \min\{1, \exp(E \Delta y)\} , \quad (2.4)$$

where now Δy is the change in the y coordinate of the *positive* particle due to the jump. Needless to say, it is irrelevant whether exchange takes place or not, if both sides carry identical content. For our simulations, we set $\Gamma = 1$. A typical Fortran source code for these simulations can be found in Appendix A.

It is important to note that in the presence of the field, our transition probabilities do not even satisfy “local detailed balance”: while W_{ph} in (2.3) reflects the work done locally by the electric field when moving a charge by one lattice site parallel to the field, W_{pp} should have $2E$ in the exponent (2.4) when two opposite charges are exchanged. If we chose this latter rate for W_{pp} and imposed “brick wall” boundary conditions in the field direction, the system would relax to its equilibrium steady state, consistent with the global Hamiltonian

$$\mathcal{H} = -E \sum_{\mathbf{x}} yn_{\mathbf{x}}^+ + E \sum_{\mathbf{x}} yn_{\mathbf{x}}^- . \quad (2.5)$$

Our choice of boundary conditions, namely, periodic, together with the biased hopping rates (2.3) and (2.4), inherently induce current-carrying non-equilibrium steady states and there is no underlying Hamiltonian. Also, as we will see in section 2.3, using these rates will yield only one coarse-grained field, as opposed to two, for the two separate exchange processes, thus they will provide a simpler framework for analytic investigations.

The microscopic dynamics defined above clearly conserves the number of each species separately. These two conserved quantities may also be chosen to be the total particle

number and the net charge, which we will associate with the terms “mass” and “charge”, respectively. As we have already mentioned, we restrict ourselves to *zero net charge*, but vary the overall mass density:

$$\bar{m} \equiv \frac{1}{L_{\perp} L_{\parallel}} \sum_{\mathbf{x}} [n_{\mathbf{x}}^{+} + n_{\mathbf{x}}^{-}] . \quad (2.6)$$

Since an equal number of positive and negative charges are driven into opposite directions, the average mass current through the system vanishes. In contrast, the average charge current is highly non-trivial, distinguishing between ordered and disordered states. To summarize, we have three control parameters: \bar{m} , E and γ . In addition, to investigate finite size effects, we have used several system sizes, varying both L_{\perp} and L_{\parallel} .

This model can be described by $P[t, C]$, the probability of finding our system in configuration $C \equiv \{n_{\mathbf{x}}^{+}, n_{\mathbf{x}}^{-}\}$ at time t . Its time evolution is governed by a master equation:

$$\partial_t P[t, C] = \sum_{C'} \{W(C' \rightarrow C) P[t, C'] - W(C \rightarrow C') P[t, C]\} , \quad (2.7)$$

where $W(C' \rightarrow C)$ is the transition rate from C' to C . Of course, C and C' can differ by just one nearest neighbor pair of occupation numbers, with W being one of the rates, W_{ph} and W_{pp} specified above. Starting our system in some initial, e.g. random, configuration, we expect it to reach a stationary state with distribution $P^*[C]$. By imposing periodic boundary conditions, we expect a *non-equilibrium*, t -independent steady state, with violation of detailed balance in general:

$$W(C' \rightarrow C) P^*[C'] \neq W(C \rightarrow C') P^*[C] . \quad (2.8)$$

In principle, finding $P^*[C]$ involves nothing more than solving a linear equation (2.7), with 0 on the left. In practice, however, this is impossible in higher than one dimension, except for special values of \bar{m} , E and γ . These particular exceptions are:

- (i.) The $E = 0$ plane. This is an equilibrium, “non-interacting” system. The particles diffuse randomly, both densities are homogeneous and $P^* \propto 1$ is the trivial solution.
- (ii.) The $\bar{m} = 1$ plane with $\gamma > 0$. Here, there are no holes, so that charge exchange is the only dynamics. Relabeling negative charges as “holes” and positive charges as “particles”, the system reduces to the biased diffusion of a single, non-interacting species. The steady state is, though non-equilibrium, also known exactly [35]: $P^* \propto 1$. While the densities are again homogeneous, the current no longer vanishes here.
- (iii.) The $\gamma = 1$ plane. Here the full distribution, $P^*[\{n_{\mathbf{x}}^{+}, n_{\mathbf{x}}^{-}\}]$, is not known but the marginal distribution of either species can be simply found. With equal rates $W_{ph} = W_{pp}$, a positive (negative) charge can no longer distinguish a negative (positive) particle from a hole. Thus, a positive (negative) particle experiences biased diffusion, slowed only by

encounters with other positive (negative) particles, just as in the case of a single, non-interacting species, and spatial inhomogeneities are again impossible for either charge density. More precisely, the marginal distribution of either species is uniform, i.e.,

$$P^* \left[\{n_{\mathbf{x}}^\pm\} \right] = \sum_{\{n_{\mathbf{x}}^\pm\}} P^* \left[\{n_{\mathbf{x}}^+, n_{\mathbf{x}}^-\} \right] \propto 1. \quad (2.9)$$

However, the full distribution (unfortunately not known) is far from being trivial, and it can result in many interesting phenomena, e.g., “hidden” long range correlations between opposite charges, in this otherwise innocent looking case.

(iv.) Finally, note that the $\bar{m} = 1$, $\gamma = 0$ line is singular in the sense that the system remains completely frozen in its initial configuration.

None of the above special cases display non-trivial spatial structures. The most interesting feature of this model is the spontaneous breaking of translational invariance, and the associated phase transitions to the *inhomogeneous* steady states are typically found through Monte Carlo simulations of P^* . A quick scan through the parameter space reveals that for small fields, the system is disordered while for larger ones, it orders (Fig. 2.1). The spontaneous formation of spatial structures, resembling a single, transverse strip of predominantly positive charge, blocking a similar strip of mostly negative charge, with the rest of the lattice being nearly empty, is easily observed. However, a quantitative phase diagram can only be drawn if one or more suitable order parameters are defined and measured. Even though the steady state currents are natural candidates, they are rather indirectly related to the steady state being disordered or ordered. Thus, it is reasonable to focus on the average density profiles themselves. In the range of investigated aspect ratios L_\perp/L_\parallel , inhomogeneities along the x (transverse) direction were never observed. Consequently, we focus on profiles averaged over x .

Instead of $n_{\mathbf{x}}^\pm$, we find it more convenient to use the local hole- and charge densities, defined as follows:

$$\begin{aligned} \phi_{\mathbf{x}} &= 1 - (n_{\mathbf{x}}^+ + n_{\mathbf{x}}^-) \\ \psi_{\mathbf{x}} &= (n_{\mathbf{x}}^+ - n_{\mathbf{x}}^-). \end{aligned} \quad (2.10)$$

The corresponding profiles of interest are denoted by

$$\begin{aligned} \phi(y) &= \frac{1}{L_\perp} \sum_x \phi_{xy} \\ \psi(y) &= \frac{1}{L_\perp} \sum_x \psi_{xy}. \end{aligned} \quad (2.11)$$

Based on the latter, the quantity

$$Q = \frac{1}{\bar{m}L_\parallel} \left\langle \sum_y [\psi(y)]^2 \right\rangle \quad (2.12)$$

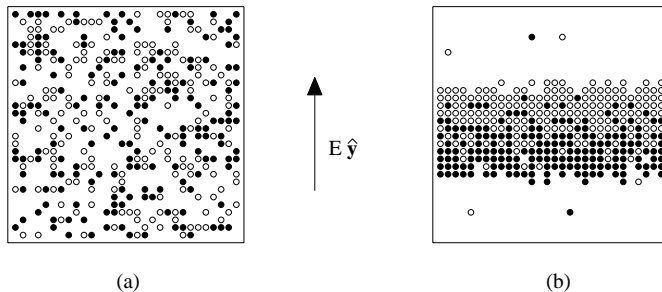


Figure 2.1: Typical configurations observed in the simulations for a 30×30 system at $\bar{m} = 0.40$ and $\gamma = 0.02$: (a) disordered at $E = 0.50$; (b) ordered at $E = 3.00$. Filled circles represent positive charges while open circles denote negative ones.

was used as an order parameter earlier [26, 31], where $\langle \dots \rangle$ denotes average over the (Monte Carlo) run, once the system reached the steady state. It is clear that Q is unity for a completely ordered system, and zero (actually, $\mathcal{O}(1/L_{\perp})$ due to finite size effects) in the completely disordered, homogeneous state. Though Q would serve us well while investigating discontinuous transitions, we find that it is not sensitive enough to signal the appearance of small amplitude, long wavelength harmonic fluctuations at a continuous transition. Indeed, this deficiency might explain why the second order transition line in the $\gamma = 0$ model had not been detected, even though it was expected theoretically [28]. Here, due to $\gamma > 0$, we expect continuous transitions to play a more prominent role. Therefore, we seek an order parameter which is more sensitive to the onset of small spatial inhomogeneities. A natural choice, designed to single out a transverse strip as well, comes from the longest wavelength Fourier component of the profile, as in the single species models [12]. Defining the transforms

$$\begin{aligned}
\phi_{\mathbf{k}} &= \frac{1}{L_{\perp}L_{\parallel}} \sum_{\mathbf{x}} \phi_{\mathbf{x}} e^{-i\mathbf{k}\mathbf{x}} \\
\psi_{\mathbf{k}} &= \frac{1}{L_{\perp}L_{\parallel}} \sum_{\mathbf{x}} \psi_{\mathbf{x}} e^{-i\mathbf{k}\mathbf{x}},
\end{aligned}
\tag{2.13}$$

where $\mathbf{k} = (k_{\perp}, k_{\parallel})$, we see that the relevant components of the profiles (2.11) are the ones with the shortest longitudinal wave-vector, i.e., $\mathbf{k} = (0, 2\pi/L_{\parallel})$. In particular, we focus on

$$\begin{aligned}
\Phi &\equiv \left| \phi_{0\frac{2\pi}{L_{\parallel}}} \right| \\
\Psi &\equiv \left| \psi_{0\frac{2\pi}{L_{\parallel}}} \right|,
\end{aligned}
\tag{2.14}$$

i.e., the *amplitudes* of the longest wavelength longitudinal Fourier components, which are the most transparent quantities for simulations. From (2.12), it is clear that Q is the sum over all longitudinal modes ($\psi_{0k_{\parallel}}$), while Ψ is only the lowest one. As we will show later in this Chapter when discussing a mean-field approach, only this mode becomes soft near a continuous transition. In this sense, the signal of such a transition is possibly obscured by the presence of other, hard modes in Q . In the next section, we will see that the simulation data are entirely consistent with this picture.

To summarize, we choose $\langle\Phi\rangle$ and $\langle\Psi\rangle$ as order parameters. The average charge current density, $\langle J\rangle$ is also studied, as in [26]. To find these quantities, we simulate our model on both square and rectangular shapes, with L_{\perp} and L_{\parallel} ranging from 20 up to 60. Near the transition line, runs are started from both random and completely ordered configurations. Elsewhere in the phase diagram, runs are started from random configurations. To map out the phase diagram, we perform runs of 10^5 MCS (Monte Carlo steps per site), discarding the first 20K MCS, to ensure that the system reached the steady state (which typically occurs already after 10K MCS). Data are taken after every 100 MCS. To analyze the nature of the transitions, we perform longer runs (5×10^5 MCS), discarding the first 62.5K MCS and sampling after 125 MCS. These measurements are then averaged over a run to give $\langle\dots\rangle$.

2.2 Monte Carlo Results

The phase diagram in the $(\overline{m}, E, \gamma)$ space has been investigated in some detail at three different γ 's: 0.02, 0.2 and 0.4, using 30×30 lattices (Fig. 2.2). For small values of \overline{m} and E , typical steady state configurations are disordered, characterized by homogeneous densities and large charge current, $\langle J\rangle$. For sufficiently large values of γ , the system remains in this phase for all \overline{m}, E . In contrast, for smaller γ , the excluded volume constraint dominates the charge exchange mechanism, and spatial inhomogeneities develop in both charge and mass density as E is increased beyond a mass- and γ -dependent threshold $E_c(\overline{m}, \gamma)$, shown as

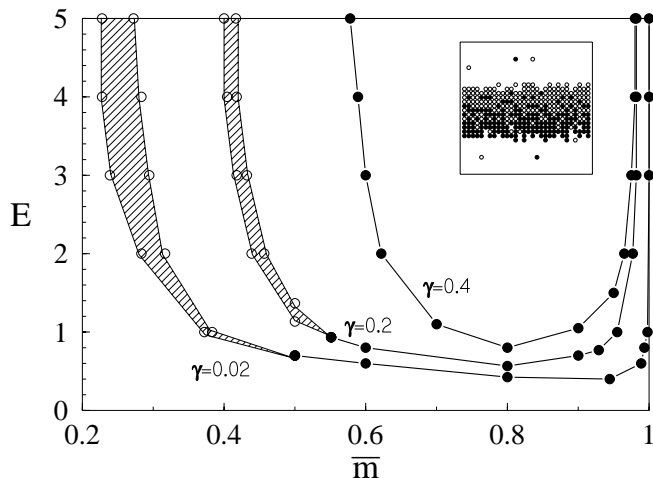


Figure 2.2: Phase diagram for a 30×30 system, in the (\bar{m}, E) plane for three different values of γ . The filled circles mark the line of continuous transitions, while the open circles denote the spinodal lines associated with first order transition. The inset shows a typical ordered configuration at $\bar{m} = 0.40$, $E = 3.00$ and $\gamma = 0.02$ with the filled (open) circles representing positive (negative) charges.

the U-shaped curves in Fig. 2.2. The particles gather into a single strip, transverse to the field, while the rest of the lattice remains essentially empty. The particle-rich strip itself is structured into two distinct regions: the “down-stream” half is dominated by negative charges, while the “up-stream” segment consists mostly of positive charges (inset of Fig. 2.2). Since the two types of charges impede each other, $\langle J \rangle$ is very small in this phase, which we refer to as “ordered”.

2.2.1 Order Parameters, Currents and Histograms

Focusing on the detailed nature of this order-disorder transition, we first describe the region of small γ (0.02 and 0.2 in our simulations), with mass density \bar{m} less than a characteristic threshold $\bar{m}_0(\gamma)$. As we vary E across the transition line $E_c(\bar{m}, \gamma)$, we observe abrupt changes in $\langle \Phi \rangle$, $\langle \Psi \rangle$ and $\langle J \rangle$ (Fig. 2.3a,b), signaling a first order transition. To confirm this assignment, we search for another distinct signal of this transition type, i.e.,

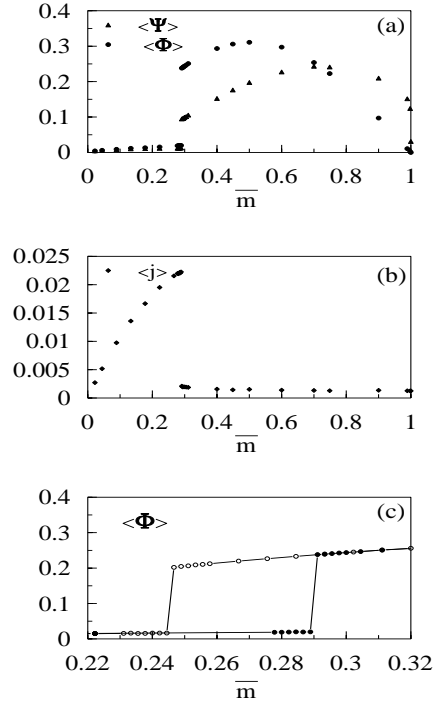


Figure 2.3: Typical observables, as functions of density \bar{m} , near the first order transition for a 30×30 system, at $E = 3.0$ and $\gamma = 0.02$. In (a) and (b), runs are started from initially random configurations. (a) Order parameters $\langle\Phi\rangle$ and $\langle\Psi\rangle$; (b) Conductivity $\langle j \rangle = \langle J \rangle / \varepsilon$; (c) Hysteresis loop across the first order transition. Open (closed) circles refer to runs started from ordered (random) initial configurations.

hysteresis. Starting from ordered (disordered) initial configurations, we perform a series of runs, decreasing (increasing) \bar{m} through the transition region, at fixed E . Both order parameters and the charge current exhibit hysteresis loops, marking the *local* stability boundary of the two phases, under these conditions. An example is displayed in Fig. 2.3c. Needless to say, the width of the hysteresis region (shown hatched in Fig. 2.2 for runs of 10^5 MCS in a 30×30 system) will vary with system size and length of runs. To demonstrate that, close to the transition, a *finite* system will switch back and forth between the ordered and disordered states, the time trace of Φ was measured during long runs of 5×10^5 MCS (Fig. 2.4a). To ease the “unlocking” of ordered configurations, a sufficiently small value of E was chosen, so that jumps against the force occur with significant probability. Based on the time trace of Φ , we construct a histogram for this variable in the usual way: we divide the interval between the smallest and the largest observed value of Φ into equal size bins, and count how many times the results of the measurements fall into each bin. Then, with proper normalization, this set of relative numbers of occurrence represents $P(\Phi)$,

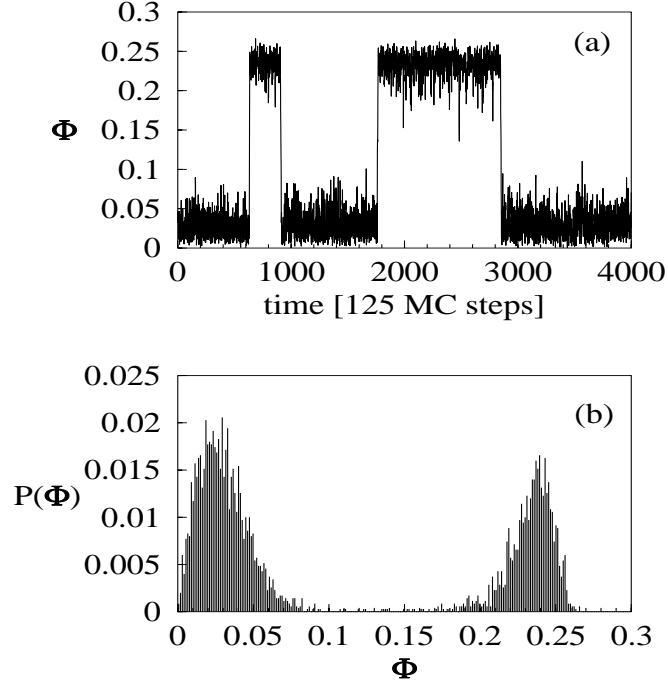


Figure 2.4: Time trace (a) and histogram (b) for the order parameter $\langle\Phi\rangle$, at $E = 1.0$, $\bar{m} = 0.38$ and $\gamma = 0.02$ for a 30×30 system.

the probability distribution for the order parameter Φ . The resulting histogram exhibits two well-separated peaks (Fig. 2.4b), corresponding to the two phases. These findings clearly support the transition being first order in this region, similar to the $\gamma = 0$ case [26]. Unfortunately, lacking the equivalent of the equilibrium free energy here, we cannot establish the precise location of the transition line without considerable computational effort.

As \bar{m} increases, the hysteresis loops exhibited by $\langle\Phi\rangle$, $\langle\Psi\rangle$ and $\langle J\rangle$ shrink, becoming unobservable for $\bar{m} \geq \bar{m}_0(\gamma)$. Instead, the order parameters and the current vary continuously (Fig. 2.5a,b) upon crossing the line $E_c(\bar{m}, \gamma)$, typical of second, rather than first order transition. The non-zero values at small E are due entirely to finite size effects, being of $\mathcal{O}((L_\perp L_\parallel)^{-1/2})$. Unlike the $\bar{m} < \bar{m}_0(\gamma)$ case above, the histograms for $\langle\Phi\rangle$ show a single peak, which moves smoothly away from the origin as the transition line is crossed (Fig. 2.6). At the transition, the distribution broadens considerably (Fig. 2.6c), reflecting an increase in the order parameter fluctuations. These data strengthen our belief that this transition is continuous in nature where the order parameter changes smoothly, and its fluctuations exhibit a relatively sharp peak at the transition. Further, we traced the

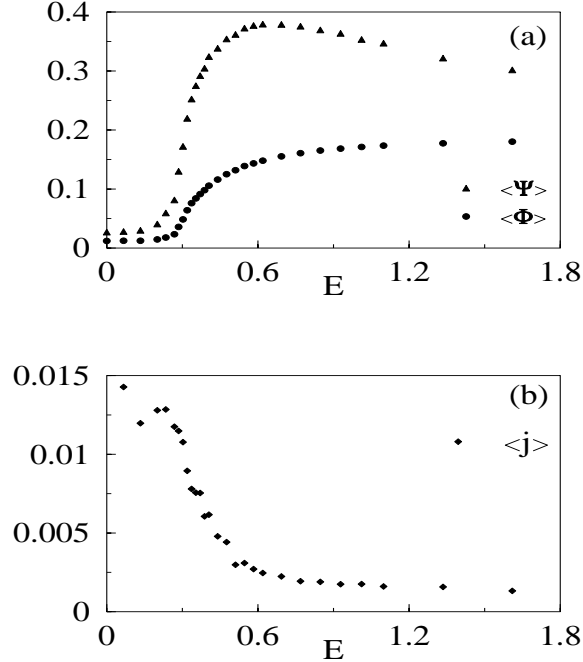


Figure 2.5: Typical observables, as functions of E , near the continuous transition for a 30×30 system, at $\bar{m} = 0.8$ and $\gamma = 0.02$. Runs started from initially random or ordered configurations collapse onto the same curve. (a) Order parameters $\langle\Phi\rangle$ and $\langle\Psi\rangle$; (b) Conductivity $\langle j\rangle = \langle J\rangle/\varepsilon$.

amplitudes and the fluctuations, of the first five longitudinal modes of the charge density, i.e., $\langle |\psi_{02\pi m_{\parallel}/L_{\parallel}}| \rangle$, with $m_{\parallel} = 1, 2, 3, 4, 5$ (Fig. 2.7). Except for the “slow” mode ($m_{\parallel} = 1$), they show absolutely no characteristic changes on crossing the line of continuous transition, fully supporting our choice of order parameters as discussed in section 2.1.

To investigate the transition in more detail, we perform long (5×10^5 MCS) runs on a series of rectangular lattices, focusing on $\langle\Phi\rangle$, its fluctuations $\langle(\Delta\Phi)^2\rangle$ and $\langle J\rangle$, at several values of E , just above and below the transition, keeping γ and \bar{m} fixed. Anticipating a result from the mean-field theory analysis (section 2.3), we plot our data versus the scaling variable $\zeta = \varepsilon L_{\parallel}$, where $\varepsilon = 2 \tanh(E/2)$ is the “coarse-grained” field. We emphasize that our objective here is to confirm the existence of a continuous transition, and to gain initial insights into the finite-size and aspect-ratio dependence of characteristic quantities. We do not attempt, at this point, to systematically measure all critical exponents. The latter endeavor would require a detailed finite-size scaling analysis, focused on the critical region, where we may expect to observe deviations from the simple mean-field scaling adopted above. Currently, such a quantitative analysis is severely hampered by the absence of

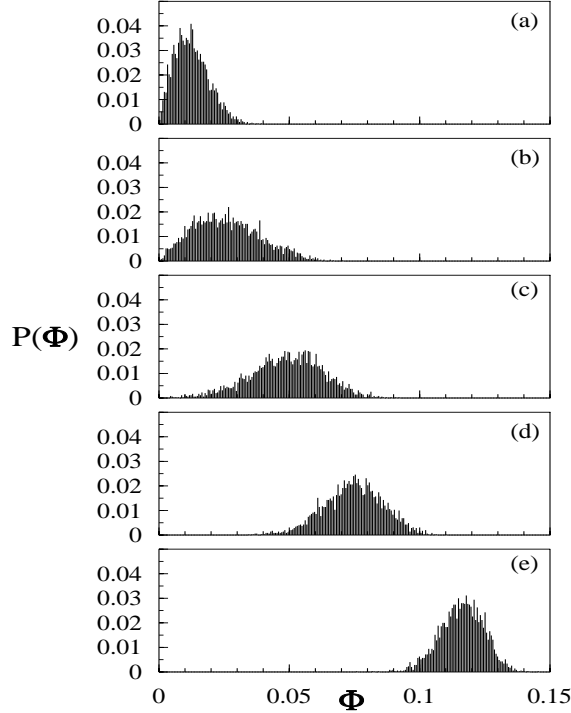


Figure 2.6: Histograms for order parameter $\langle\Phi\rangle$, near the continuous transition, for a 30×30 system at $\bar{m} = 0.8$ and $\gamma = 0.02$, for a series of E : (a) $E = 0.13$; (b) $E = 0.27$; (c) $E = 0.30$; (d) $E = 0.34$; (e) $E = 0.44$.

reliable field theory predictions for the leading universal scaling behavior of our model.

Returning to the data, Fig. 2.8 shows our results for lattices with $L_{\parallel} = 20$ fixed, and $L_{\perp} = 20, 40$ and 60 , while Fig. 2.9 corresponds to $L_{\parallel} = 20, 40$ and 60 with L_{\perp} fixed at 20 . With the exception of a finite-size tail, $\langle\Phi\rangle$ is essentially independent of L_{\perp} , depending on L_{\parallel} only through the scaling variable ζ (Fig. 2.8a, 2.9a). From these figures we see that the critical point occurs at $\zeta_c \simeq 8.85$. Keeping the limited accuracy of our data in the critical region in mind, a log-log plot of $\langle\Phi\rangle$ versus $\zeta - \zeta_c$ for $\zeta > \zeta_c$, yields a first estimate for the order parameter exponent, $\beta \simeq 0.37$ (Fig. 2.10). This value is to be taken with great caution since we have not performed a systematic finite size scaling, incorporating strong anisotropies.

A reliable indication for the presence of a continuous transition is provided by the fluctuations $\langle(\Delta\Phi)^2\rangle$ (Fig. 2.8b, 2.9b), normalized to 1 in the fully random phase ($E = 0$). While the height of the peak centered about ζ_c appears to be only weakly dependent on L_{\parallel} (Fig. 2.9b), it increases significantly with L_{\perp} (Fig. 2.8b). This intriguing size dependence is born out by our theoretical analysis (section 2.3). Finally, we focus on the conductivity

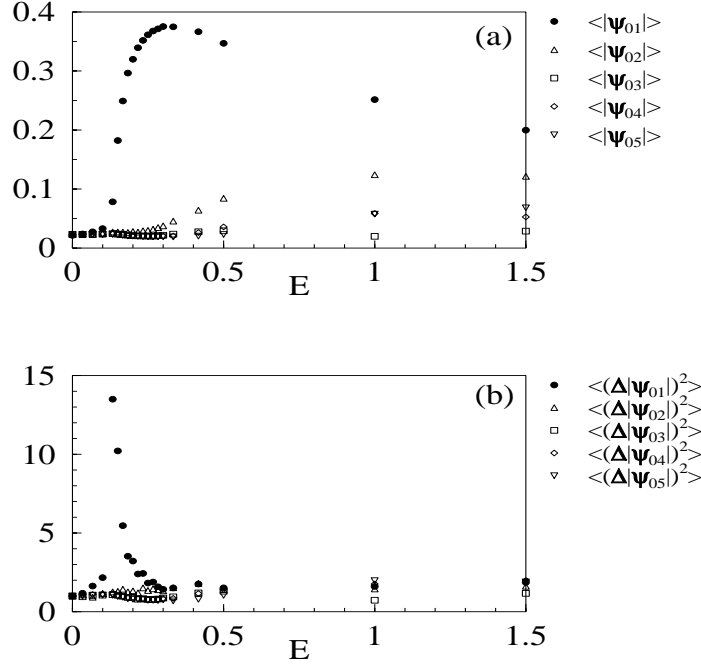


Figure 2.7: Amplitudes (a) and their fluctuations (b), of the first five longitudinal Fourier components of the charge density as functions of E , near the continuous transition for a 20×60 system, at $\bar{m} = 0.8$ and $\gamma = 0.02$. For short-hand, $\langle |\psi_{0 m_{\parallel}}| \rangle$ represents the $(0, 2\pi m_{\parallel}/L_{\parallel})$ the Fourier component.

$\langle j \rangle = \langle J \rangle / \varepsilon$ (Fig. 2.8c, 2.9c). To ease comparison with analytic results, the conductivity was rescaled by the factor $1/(1 + e^{-|E|})$. This “normalization” is suggested by the explicit E -dependence of the “parallel” component of the diffusion matrix in the mean-field theory (section 2.3). We find that it improves data collapse significantly in the case where systems with different L_{\parallel} ’s were considered (Fig. 2.9c). Fluctuating about a constant value in the disordered phase, $\langle j \rangle$ appears to exhibit a discontinuity in its slope, upon crossing the transition line into the ordered region. Beyond the transition, it decreases monotonically, approaching a small limiting value deep in the ordered phase. This value is proportional to γ , which fits well with the picture that particle-hole exchanges are rare in this regime and $\langle j \rangle$ is dominated by the charge exchange mechanism. To summarize, all of these characteristics are consistent with the scenario of a continuous transition. Clearly, the scaling of the critical parameter, ζ_c , with the longitudinal system size L_{\parallel} , is crucial: for $L_{\parallel} \rightarrow \infty$, the transition shifts to $E = 0$.

For $\gamma = 0.2$, the behavior of the system is qualitatively similar to the case $\gamma = 0.02$. The major differences are as follows.

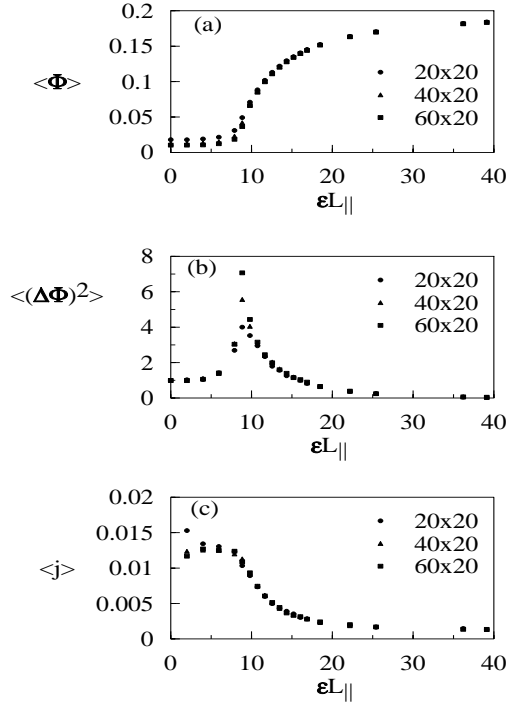


Figure 2.8: Characteristic observables, as functions of $\zeta = \epsilon L_{\parallel}$, near the continuous transition for an $L_{\perp} \times 20$ system, with L_{\perp} ranging from 20 to 60, at $\bar{m} = 0.8$ and $\gamma = 0.02$. (a) Order parameter $\langle \Phi \rangle$; (b) Normalized order parameter fluctuations $\langle (\Delta \Phi)^2 \rangle$; (c) Conductivity $\langle j \rangle$.

- (i.) Since larger γ favors the disordered phase, the whole transition line is shifted upwards.
- (ii.) The region between the spinodals is narrower.
- (iii.) The point $\bar{m}_0(\gamma)$ shifts to slightly higher densities.
- (iv.) Finally, there appears to be a *finite* region of disorder for all E , just below complete filling.

Concerning the last point, we have some further remarks. Clearly, the plane $\bar{m} = 1$ itself must be disordered, given that the associated steady state distribution is homogeneous. However, for $\gamma = 0.02$, $E \gtrsim 3.0$ and $L_{\perp} = L_{\parallel} = 30$, the removal of just two particles suffices to induce spatial inhomogeneities, with the two holes performing a biased random walk which leaves a charge segregated region in its wake. For $\gamma = 0.2$, on the other hand, the system remains disordered until the density of holes exceeds 0.02 on a 30×30 lattice. We should caution, however, that considerably more work is required here before a reliable conclusion, concerning the details of the phase diagram near $\bar{m} = 1$ for different system sizes, can be reached.

Once γ has reached 0.4, $\bar{m}_0(\gamma)$ appears to have vanished, in that we no longer observe

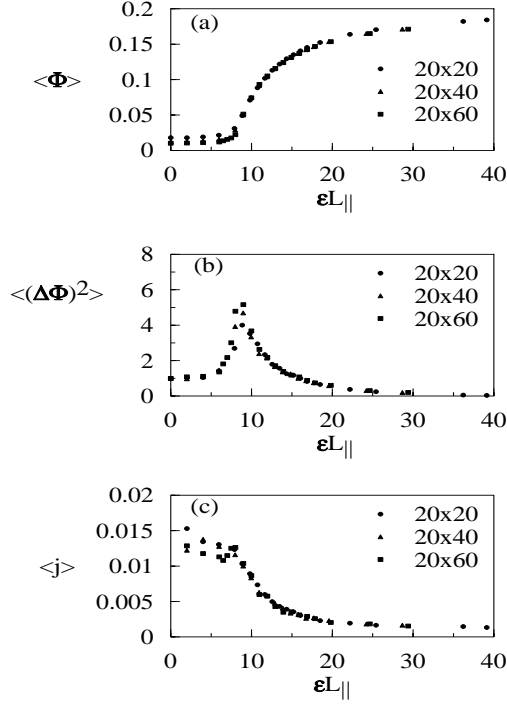


Figure 2.9: Characteristic observables, as functions of $\zeta = \varepsilon L_{\parallel}$, near the continuous transition for an $20 \times L_{\parallel}$ system, with L_{\parallel} ranging from 20 to 60, at $\bar{m} = 0.8$ and $\gamma = 0.02$. (a) Order parameter $\langle \Phi \rangle$; (b) Normalized order parameter fluctuations $\langle (\Delta \Phi)^2 \rangle$; (c) Conductivity $\langle j \rangle$.

any indications of metastability or hysteresis. Thus, the line $E_c(\bar{m}_0(\gamma), \gamma)$, being a line of multicritical points, separates a surface of first order transition from a surface of continuous ones.

To complete the phase diagram, we also investigate the transition as γ varies, for fixed (\bar{m}, E) , in a system of size 30×30 . Consistent with our previous findings for $E_c(\bar{m}_0(\gamma), \gamma)$, the order of the transition depends on where the order-disorder transition surface is crossed. In particular, we vary γ at $\bar{m} = 0.8$ and $E = \infty$ for a 30×30 system. Here the transition is clearly continuous, indicated by a continuous change in $\langle \Phi \rangle$ and $\langle \Psi \rangle$ (Fig. 2.11a), a peak in their fluctuations $\langle (\Delta \Phi)^2 \rangle$ and $\langle (\Delta \Psi)^2 \rangle$ (Fig. 2.11b) and a slight discontinuity in the slope of the current $\langle j \rangle$ (Fig. 2.11c), on crossing the transition surface. For $\gamma > \gamma_{max} \simeq 0.62$, the charge exchange mechanism suppresses the ordered phase entirely.

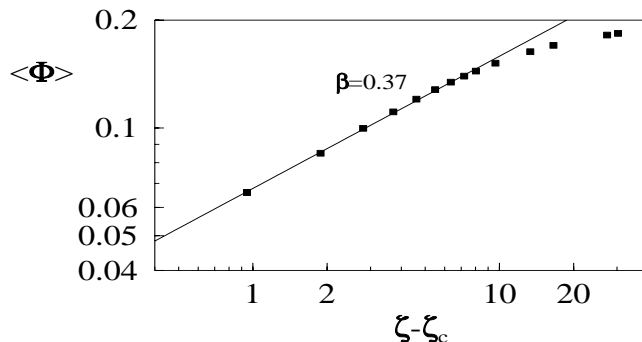


Figure 2.10: A log-log plot of $\langle \Phi \rangle$ versus $\zeta - \zeta_c$, where $\zeta = \varepsilon L_{\parallel}$ is the scaling variable and $\zeta_c = 8.85$. Here we used the data for the 60×20 system at $\bar{m} = 0.8$ and $\gamma = 0.02$.

2.2.2 Density Profiles in the Ordered Phase

While the Fourier components $\langle \Phi \rangle$ and $\langle \Psi \rangle$ allow us to distinguish easily between the disordered and ordered phases, the full profiles, $\phi(y)$ and $\psi(y)$, carry far more detailed information about the structure of the ordered phase itself. In particular, characteristic profiles measured near the first order transition differ significantly from their counterparts near the continuous transition. Focusing on the ordered phase, just beyond the first order transition line, the charge and hole density profiles are similar to those found in [26, 28] for $\gamma = 0$, i.e., the particle-rich strip exhibits three fairly sharp interfaces: two of these separate particles from holes at either end of the strip, while the third one is located in the middle of the strip, marking the boundary between positive and negative charges (Fig. 2.12a). The hole density vanishes in the central region of the strip, so that the small residual current in this locked state is almost entirely due to charge exchange. In stark contrast, near the second order transition line, both charge and hole density profiles resemble harmonic functions, and the hole profile never vanishes, so that the system orders, but does not lock up fully (Fig. 2.12b).

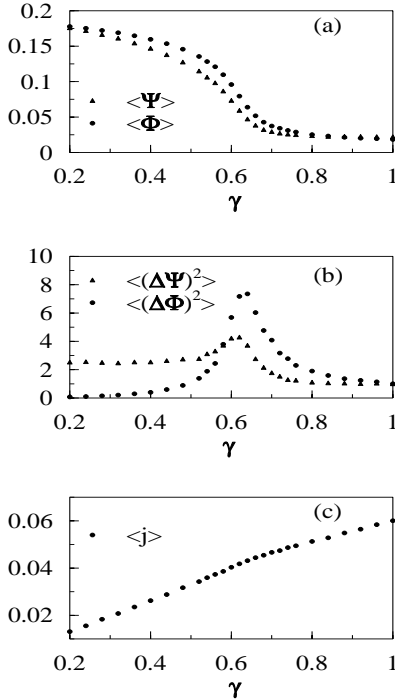


Figure 2.11: Typical observables, as functions of γ , near the continuous transition for a 30×30 system, at $\bar{m} = 0.8$ and $E = \infty$. (a) Order parameters $\langle \Phi \rangle$ and $\langle \Psi \rangle$; (b) Normalized order parameter fluctuations $\langle (\Delta \Phi)^2 \rangle$ and $\langle (\Delta \Psi)^2 \rangle$; (c) Conductivity $\langle j \rangle$.

Moving deeper into the ordered phase, one might expect to find profiles similar to Fig. 2.12a. Instead, for larger particle densities, the central interface begins to soften, so that the strip, reminiscent of a sandwich, develops three, rather than two, regions. While its lower (upper) part still consists of mainly of + (−) charges, there is now a distinct middle section which shows both species mixing by virtue of charge exchange (Fig. 2.12c). At the same time, the interfaces between particles and holes remain quite sharp. Finally, turning to ordered profiles near complete filling, the middle section of a strip has widened even further, bounded by two regions of either charge at the ends. Simultaneously, the two particle-hole interfaces have approached one another so closely that the few remaining holes are confined to just two or three rows. In fact, it is intriguing to track the dynamics of the ordering process here, starting from an initially random configuration: each hole acts as a catalyst for the charge segregation process, creating a predominantly positive domain separated by a sharp interface from a similar, negatively dominated region located “up-stream”. For the system sizes considered here, these partially ordered regions quickly merge into a single strip, trapping the holes in the interfacial region (Fig. 2.12d).

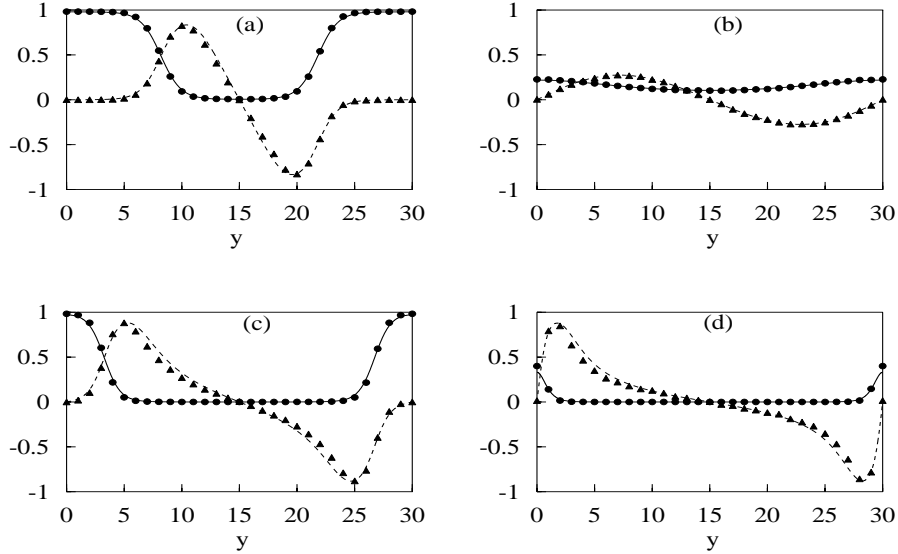


Figure 2.12: Characteristic Profiles in the Ordered Phase. Circles and triangles denote simulation results for the hole density profile $\phi(y)$ and the charge density profile $\psi(y)$, respectively. The system size is 30×30 , $\gamma = 0.02$. Solid (dashed) lines are mean-field theory profiles for the hole (charge) density. (a) $\bar{m} = 0.46$ and $E = 1.35$ ($\varepsilon L_{\parallel} = 35.29$); (b) $\bar{m} = 0.84$ and $E = 0.28$ ($\varepsilon L_{\parallel} = 8.45$); (c) $\bar{m} = 0.78$ and $E = 1.84$ ($\varepsilon L_{\parallel} = 43.51$); (d) $\bar{m} = 0.98$ and $E = 2.97$ ($\varepsilon L_{\parallel} = 54.16$).

2.3 Mean-field Theory

We now turn to the analytic description of our model, in order to develop a better understanding of the nature of the order-disorder transition discussed in the previous section. As already indicated, this also provides the framework in which first predictions, concerning, e.g., the size dependence of characteristic observables, can be made. Aiming towards universal properties, we will construct a set of coarse-grained equations of motion, in continuous space and time, for the two conserved densities in our system. While the master equation (2.7) is far too difficult to solve, even for stationary states, it serves as a convenient starting point for this approach. A standard procedure is to derive a hierarchy of evolution equations for the densities and higher order correlations, based on that of the probability density, $P[t, C]$, itself. Here we only consider the mean-field approximation, which consists of truncating higher order density-density correlations [27], so that a closed

set of equations for the *average* densities alone results. This level is sufficient to analyze the simulation results discussed in the previous section. In the next Chapter, however, we will go further and perform a systematic way to analyze not only averages, but the density fluctuations as well, which will reveal more about collective behavior in our system.

Using the mean-field equations, explicit stationary solutions to these equations will be found, corresponding to spatially homogeneous and inhomogeneous steady states. A linear stability analysis around the former will be presented. Our goal is to establish a parallel to the simulation results. By associating stable homogeneous solutions with the disordered phase, and inhomogeneous ones with typical ordered configurations, we are able to predict the characteristic behavior of the order parameters, the currents and the density profiles. Finally, using an adiabatic elimination procedure, we project out an equation of motion for the slow mode, resulting in an analytic expression for the “tricritical” line which separates first order from continuous transitions. Since this analytic approach provides us with good qualitative agreement with simulation results, we believe that considerable insight into the nature of these transitions is gained.

2.3.1 Equations of Motion

Defining the average densities of positive and negative particles,

$$\langle n_{\mathbf{x}}^{\pm} \rangle \equiv \sum_C P[t, C] n_{\mathbf{x}}^{\pm}, \quad (2.15)$$

their time evolution follows from that of $P[t, C]$:

$$\partial_t \langle n_{\mathbf{x}}^{\pm} \rangle = \sum_C \partial_t P[t, C] n_{\mathbf{x}}^{\pm}. \quad (2.16)$$

Exploiting the master equation (2.7) with rates (2.3,2.4) and $\Gamma = 1$, we obtain for, e.g., $\langle n_{\mathbf{x}}^+$

$$\begin{aligned} \partial_t \langle n_{xy}^+ \rangle = & \\ & - \langle n_{xy}^+ (\phi_{x-ay} + \phi_{x+ay} + \phi_{xy-a} e^{-E} + \phi_{xy+a}) \rangle \\ & + \langle \phi_{xy} (n_{x-ay}^+ + n_{x+ay}^+ + n_{xy-a}^+ + n_{xy+a}^+ e^{-E}) \rangle \\ & - \gamma \langle n_{xy}^+ (n_{x-ay}^- + n_{x+ay}^- + n_{xy-a}^- e^{-E} + n_{xy+a}^-) \rangle \\ & + \gamma \langle n_{xy}^- (n_{x-ay}^+ + n_{x+ay}^+ + n_{xy-a}^+ + n_{xy+a}^+ e^{-E}) \rangle, \end{aligned} \quad (2.17)$$

where a is the lattice constant. This equation, just like the master equation itself, is a balance equation, now for the average density n_{xy}^+ . For example, the first term in (2.17), $-\langle n_{xy}^+ \phi_{x-ay} \rangle$, represents the jump of a positive particle at site (x, y) to a nearest neighbor

empty site, $(x - a, y)$. The rest of the terms are related similarly to the microscopic dynamics. We see that the right hand side of (2.17) contains second order correlations. The mean-field approximation consists of truncating these correlations and replacing $\langle nn \rangle$ by $\langle n \rangle \langle n \rangle$. For simplicity we drop the $\langle \dots \rangle$ symbols so that $n_{\mathbf{x}}^{\pm}$ denotes *time*- and space-dependent average densities. Also we find it useful to define the following new parameters:

$$\begin{aligned}\Gamma_{\perp} &= 1 \\ \Gamma_{\parallel} &= \frac{1}{2} (1 + e^{-|E|}) \\ \varepsilon &= 2 \tanh(E/2).\end{aligned}\tag{2.18}$$

Then the equation of motion for $n_{\mathbf{x}}^{+}$ can be written as

$$\begin{aligned}\partial_t n_{xy}^{+} &= \\ &\Gamma_{\perp} \left[-n_{xy}^{+} (\phi_{x-ay} + \phi_{x+ay}) + \phi_{xy} (n_{x-ay}^{+} + n_{x+ay}^{+}) \right] + \\ &\Gamma_{\parallel} \left[-n_{xy}^{+} \phi_{xy-a} \left(1 - \frac{\varepsilon}{2}\right) - n_{xy}^{+} \phi_{xy+a} \left(1 + \frac{\varepsilon}{2}\right) + \phi_{xy} n_{xy-a}^{+} \left(1 + \frac{\varepsilon}{2}\right) + \phi_{xy} n_{xy+a}^{+} \left(1 - \frac{\varepsilon}{2}\right) \right] + \\ &\gamma \Gamma_{\perp} \left[-n_{xy}^{+} (n_{x-ay}^{-} + n_{x+ay}^{-}) + n_{xy}^{-} (n_{x-ay}^{+} + n_{x+ay}^{+}) \right] + \\ &\gamma \Gamma_{\parallel} \left[-n_{xy}^{+} n_{xy-a}^{-} \left(1 - \frac{\varepsilon}{2}\right) - n_{xy}^{+} n_{xy+a}^{-} \left(1 + \frac{\varepsilon}{2}\right) + n_{xy}^{-} n_{xy-a}^{+} \left(1 + \frac{\varepsilon}{2}\right) + n_{xy}^{-} n_{xy+a}^{+} \left(1 - \frac{\varepsilon}{2}\right) \right].\end{aligned}\tag{2.19}$$

To obtain the time evolution of $n_{\mathbf{x}}^{-}$, we simply have to replace $n_{\mathbf{x}}^{\pm}$ by $n_{\mathbf{x}}^{\mp}$ and ε by $-\varepsilon$, reflecting a symmetry of the system. For our theoretical analysis, it turns out to be more convenient to consider the densities in continuous space as well. Thus, we take a naive continuum limit so that $n_{\mathbf{x}}^{\pm}(t) \rightarrow \rho^{\pm}(\mathbf{x}, t)$ and similarly for the hole and charge densities, i.e., $\phi(\mathbf{x}, t) = 1 - (\rho^{+}(\mathbf{x}, t) + \rho^{-}(\mathbf{x}, t))$ and $\psi(\mathbf{x}, t) = \rho^{+}(\mathbf{x}, t) - \rho^{-}(\mathbf{x}, t)$. Since we assume that ρ^{\pm} are slowly varying (coarse-grained) densities, we can neglect higher than second order spatial derivatives. Choosing unit lattice constant we obtain

$$\partial_t \rho^{\pm} = -\nabla \Gamma \left\{ [\rho^{\pm} \overset{\leftrightarrow}{\nabla} \phi \pm \varepsilon \hat{y} \rho^{\pm} \phi] + \gamma [\rho^{\pm} \overset{\leftrightarrow}{\nabla} \rho^{\mp} \pm \varepsilon \hat{y} \rho^{\pm} \rho^{\mp}] \right\},\tag{2.20}$$

where

$$\Gamma = \begin{pmatrix} \Gamma_{\perp} & 0 \\ 0 & \Gamma_{\parallel} \end{pmatrix}\tag{2.21}$$

is the diffusion matrix, ε is the coarse-grained drive and \hat{y} is the unit vector along the y direction. $\overset{\leftrightarrow}{\nabla}$ is the asymmetric gradient operator, i.e., for any two functions f and g , $f \overset{\leftrightarrow}{\nabla} g = f \nabla g - g \nabla f$. Equations (2.20) are clearly continuity equations as a result of the particle conserving dynamics. They also manifest the equivalent structure of particle-hole and charge exchanges, the ratio of the associated rates being γ . Setting $\gamma = 0$, we recover

the equations of motion first proposed in [26], for a model without charge exchange. Thus the second term in the $\{\dots\}$ brackets, being proportional to γ , models the new process. The full expression under the $\{\dots\}$ brackets is just the current density \mathbf{j}^\pm of the \pm particles.

Equations (2.20) may also be regarded as the “coarse-grained” version of the microscopic dynamics, especially if we “add” Langevin noise terms. In fact, we will pursue this direction in a systematic way in Chapter 3. As already mentioned, the important symmetry here, under the combined operation $\rho^\pm \rightarrow \rho^\mp$ and $\varepsilon \rightarrow -\varepsilon$, is evident.

A helpful alternate perspective of (2.20) can be gained by using, instead of ρ^+ and ρ^- , the hole and charge densities, $\phi(\mathbf{x}, t)$ and $\psi(\mathbf{x}, t)$, respectively. Their time evolutions are governed by

$$\begin{aligned}\partial_t \phi &= \nabla \Gamma \{ \nabla \phi + \varepsilon \hat{\mathbf{y}} \phi \psi \} \\ \partial_t \psi &= \nabla \Gamma \left\{ \gamma \nabla \psi + (1 - \gamma) \phi \overleftrightarrow{\nabla} \psi - \varepsilon \hat{\mathbf{y}} \phi (1 - \phi) - \frac{\gamma}{2} \varepsilon \hat{\mathbf{y}} [(1 - \phi)^2 - \psi^2] \right\} .\end{aligned}\tag{2.22}$$

To complete the specification we impose periodic boundary conditions (PBC) on the densities and constraints due to \overline{m} and zero net charge:

$$\begin{aligned}\int dV \phi(\mathbf{x}, t) &= (1 - \overline{m}) L_\perp L_\parallel \\ \int dV \psi(\mathbf{x}, t) &= 0 .\end{aligned}\tag{2.23}$$

Simulation Profiles and Stationary Solutions of the Discrete Equations of Motion

Before proceeding with the solution of the continuum version of the mean-field equations (2.22), we make a check on their discrete version, to see how closely the steady state simulation profiles “satisfy” those equations. In particular, we consider the equation of motion for the hole density. Looking for stationary solutions and assuming no variations along the transverse (x) direction, on a lattice we have

$$\begin{aligned}0 &= \Gamma_\parallel \left\{ \phi(y+1) - 2\phi(y) + \phi(y-1) \right. \\ &\quad \left. + \frac{\varepsilon}{2} \{ \psi(y) [\phi(y+1) - \phi(y-1)] + \phi(y) [\psi(y+1) - \psi(y-1)] \} \right\} ,\end{aligned}\tag{2.24}$$

rather than (2.22). Note that Γ_\parallel is just a positive constant. Now we take the simulation profiles as defined in eqs. (2.11), averaged over the time series in the steady state, and construct the following functional with them:

$$I_\varepsilon[\phi(y), \psi(y)] = \sum_y \left\{ f[\phi(y)] + \varepsilon g[\phi(y), \psi(y)] \right\}^2 ,\tag{2.25}$$

where

$$\begin{aligned} f[\phi(y)] &= \phi(y+1) - 2\phi(y) + \phi(y-1) \\ g[\phi(y), \psi(y)] &= \frac{1}{2} \{ \psi(y) [\phi(y+1) - \phi(y-1)] + \phi(y) [\psi(y+1) - \psi(y-1)] \} . \end{aligned} \quad (2.26)$$

Here we consider ε as a phenomenological parameter, rather than a quantity known from microscopics. To find the best fit value of this parameter, for which the simulation profiles satisfy eqn. (2.24) with the smallest deviation (2.25), it is sufficient to minimize I_ε with respect to ε , yielding:

$$\varepsilon^* = - \frac{\sum_y f[\phi(y)] g[\phi(y), \psi(y)]}{\sum_y \{g[\phi(y), \psi(y)]\}^2} . \quad (2.27)$$

We can visualize the results of the minimization by recasting eqn. (2.24) in the form

$$f[\phi(y)] = -\varepsilon g[\phi(y), \psi(y)] , \quad (2.28)$$

and plotting the left, and the right hand side of this equation independently, using the simulation profiles and the corresponding ε^* (Fig. 2.13). Fig. 2.13a shows the hole and charge density profiles, obtained from simulation, for a 30×30 system at $\bar{m} = 0.8$, $E = 0.928$ and $\gamma = 0.02$. For the same profiles, Fig. 2.13b illustrates the left, and the right hand side of equation (2.28), i.e., f and $-\varepsilon^*g$, respectively.

The question naturally arises: how closely ε^* matches $2 \tanh(E/2)$, i.e., its mean-field value (2.18). To test this, we performed the above procedure for a series of simulation profiles for the same system size, \bar{m} and γ , while we varied E . The results are shown in Fig. 2.13c. It is clear that for $E \gtrsim 0.3$, ε^* 's fall on the theoretical (mean-field) curve, while below this value, they deviate significantly from it. It is worthwhile to refer to Fig. 2.5 and realize that $E \simeq 0.3$ is just the value of the external drive above which spatial inhomogeneities are starting to appear. Below this value, the simulation profiles are homogeneous (up to finite size fluctuations), and fitting equation (2.28) clearly does not make any sense.

We also considered the discrete equation of motion for ψ and found that the discrepancy, when fitting that equation to simulation profiles, was far greater than in the previous case. We do not pursue adding additional terms, representing lowest order correction to our mean-field theory, but just note that such an attempt has been made in related models [36]. The symmetry of such correction terms is such that they cancel in the equation for the hole density, but contribute an extra term in the equation for the charge density, being consistent with our results.

2.3.2 Homogeneous and Inhomogeneous Solutions

In this subsection, we investigate the stationary solutions of (2.22), i.e., solutions satisfying $\partial_t \phi = \partial_t \psi = 0$, subject to PBC and the constraints (2.23). By virtue of the second equation

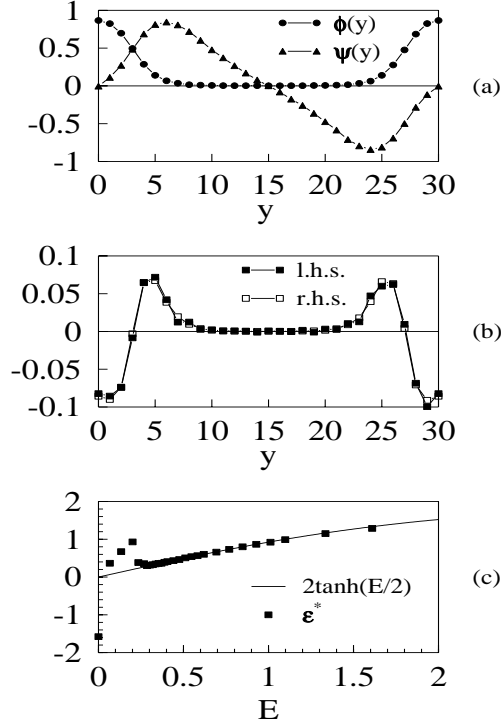


Figure 2.13: Fitting equation (2.24) to simulation profiles. Substituted profiles are obtained from simulations of 30×30 systems at $\bar{m} = 0.8$ and $\gamma = 0.02$. (a) Hole ($\phi(y)$) and charge ($\psi(y)$) density profiles at the above values of parameters and at $E = 0.928$; (b) The left hand side (l.h.s) and right hand side (r.h.s.) of equation (2.28) using the same profiles as in (a) and with the best-fit value of ϵ ; (c) A series of fittings, for different E 's. The data points represent the fitted drive, ϵ^* , while the solid line is the mean-field curve.

of (2.23), it is immediately clear that such solutions can carry no hole (or mass) current: since the densities of positive and negative charges are equal, the mass current through any surface will vanish in the steady state. The charge current, on the other hand, can, and will be, non-trivial. Being continuity equations, eqs. (2.22) are trivially satisfied by homogeneous hole and charge densities:

$$\begin{aligned}\phi(\mathbf{x}, t) &\equiv 1 - \bar{m} \\ \psi(\mathbf{x}, t) &\equiv 0.\end{aligned}\tag{2.29}$$

Inserting these into (2.22), we may identify the charge current density associated with these homogeneous solutions:

$$J_H = \epsilon \left[\bar{m}(1 - \bar{m}) + \frac{\gamma}{2} \bar{m}^2 \right]\tag{2.30}$$

Thus, the conductivity, $j_H \equiv J_H/\varepsilon$, is independent of ε . Comparing to Fig. 2.5b, and Fig. 2.8c, Fig. 2.9c, we note that this is approximately satisfied by our simulation results.

Next we demonstrate the existence of inhomogeneous solutions. To mirror typical ordered configurations, we seek for solutions of the form $\phi(\mathbf{x}, t) \equiv \phi(y)$, $\psi(\mathbf{x}, t) \equiv \psi(y)$, displaying a spatial dependence in y only. Inserting this ansatz, we can integrate eqs. (2.22) once. The integration constants are just the hole and charge current densities carried by $\phi(y)$, $\psi(y)$. By symmetry, only the latter, denoted by J_I , can be non-zero. Rescaling the coordinate $y \rightarrow z \equiv \varepsilon y$ and introducing the conductivity $j_I \equiv J_I/\varepsilon$, we cast eqs. (2.22) into the form:

$$0 = \phi' + \phi\psi \quad (2.31)$$

$$-j_I = \gamma\psi' + (1 - \gamma)(\phi\psi' - \psi\phi') - \phi(1 - \phi) - \frac{\gamma}{2} [(1 - \phi)^2 - \psi^2] , \quad (2.32)$$

where ϕ and ψ are simply functions of z , and the prime denotes differentiation with respect to z . Equation (2.31) allows us to eliminate $\psi = -\phi'/\phi$ in favor of ϕ so that (2.32) reduces to an ordinary differential equation for ϕ . Unlike in the model without charge exchange [26], however, the substitution $\chi(z) \equiv 1/\phi(z)$ *does not* lead directly to an equation of potential form for χ'' . There, the resulting equation was equivalent to the one describing the motion of a particle in a one dimensional potential:

$$\chi'' = -\frac{d}{d\chi}W(\chi) . \quad (2.33)$$

Here, suppressing the subscript on j , we obtain

$$\chi'' = \frac{1}{1 - \gamma + \gamma\chi} \left\{ -j\chi^2 + \chi - 1 + \frac{\gamma}{2} [(\chi - 1)^2 + (\chi')^2] \right\} , \quad (2.34)$$

which reduces to the potential form only upon setting $\gamma = 0$. However, defining a new function $u(\chi(z))$ via

$$u \equiv \sqrt{1 - \gamma + \gamma\chi} > 0 , \quad (2.35)$$

we transform (2.34) into the desired form for $\gamma > 0$. Thus,

$$u'' = -\frac{d}{du}V(u) , \quad (2.36)$$

where

$$V(u) = \frac{2j - \gamma}{8\gamma} u^2 - \frac{1 - \gamma}{\gamma} j \ln(u) - \frac{2(1 - \gamma)^2 j + \gamma}{8\gamma} \frac{1}{u^2} . \quad (2.37)$$

By definition, χ is restricted to the interval $[1, \infty)$, and from (2.35), so is u . In order to find periodic solutions for u which map into spatially inhomogeneous solutions for ϕ and ψ , $V(u)$ must possess a local minimum in that range. The extrema of $V(u)$ are given by

$$\left. \frac{dV}{du} \right|_{u^*} = \frac{2j - \gamma}{4\gamma} u^* - \frac{1 - \gamma}{\gamma} j \frac{1}{u^*} + \frac{2(1 - \gamma)^2 j + \gamma}{4\gamma} \frac{1}{u^{*3}} = 0, \quad (2.38)$$

yielding

$$(u_{\pm}^*)^2 = \frac{2j(1 - \gamma) \pm \gamma \sqrt{1 - 2j(2 - \gamma)}}{2j - \gamma}. \quad (2.39)$$

For $0 < \gamma < 1$, u_+^* is the local minimum while u_-^* is the local maximum as it can be seen from

$$\begin{aligned} \left. \frac{d^2V}{du^2} \right|_{u_{\pm}^*} &= \frac{1}{\gamma} \left[(2j - \gamma) - (1 - \gamma) 2j \frac{1}{u_{\pm}^{*2}} \right] \\ &= \left(\frac{2j}{\gamma} - 1 \right) \left[1 - \frac{1}{1 \pm \frac{\gamma}{2j(1 - \gamma)} \sqrt{1 - 2j(2 - \gamma)}} \right], \end{aligned} \quad (2.40)$$

provided that

$$\frac{\gamma}{2} < j < \frac{1}{4 - 2\gamma}. \quad (2.41)$$

Since the potential $V(u)$ here is quite complicated, the solutions of (2.36) cannot be found in a closed form, unlike the $\gamma = 0$ case [26, 28]. However, the hole and charge density profiles can easily be obtained by numerical integration. As initial conditions, we choose a value for j in the range specified by (2.41), and set $u(0) \equiv u_0$, $u'(0) = 0$. To compare with a simulation, the integration constants u_0 and j must be mapped onto the relevant microscopic parameters, i.e., \bar{m} , E and L_{\parallel} . $\gamma = 0.02$ is taken to be the same for both numerical integration and simulation. It is clear that L_{\perp} does not appear in the mean-field equations. Further, we set $L_{\parallel} = 30$ so that we can compare the numerical profiles to the ones obtained by simulations with this longitudinal size. Once a mean-field profile $\phi(z)$ is obtained, first, we can read off its period, l . Since $z = \varepsilon y$ was the rescaled coordinate, $l = \varepsilon L_{\parallel}$. With a given longitudinal system size ($L_{\parallel} = 30$) this provides us with E , via $E = 2 \tanh^{-1}(\varepsilon/2)$ (2.18). Then we determine the overall mass density, \bar{m} , by $\int dz \phi(z) = l(1 - \bar{m})$. These steps are summarized in Table 2.1. Finally, scaling “back” the mean-field profiles, so that they depend on the original y coordinate, we can compare them to the simulation results with the parameters obtained above. It is clear that through this procedure, there are no fit parameters! The resulting profiles, obtained by numerical integration of our mean-field theory and simulation at the associated points in the phase diagram, are shown in Fig.

$L_{\parallel} = 30$	j	u_0	$l = \varepsilon L_{\parallel}$	E	\bar{m}
(a)	0.02	1.00021	35.29	1.35	0.46
(b)	0.125	1.035	8.45	0.28	0.84
(c)	0.011	1.0003	43.51	1.84	0.78
(d)	0.0103	1.020	54.16	2.97	0.98

Table 2.1: Mapping the parameters of the numerical integration (j, u_0), onto the microscopic parameters (\bar{m}, E) with $L_{\parallel} = 30$.

2.12. The agreement is impressive. In particular, near complete filling the profiles clearly reflect the localization of the hole density at the steep plus-minus interface. To conclude, we note that small deviations from the Monte Carlo data are confined to the regions of largest ϕ' and ψ' and can be possibly reduced further by including higher derivatives in (2.20, 2.22).

2.3.3 Linear Stability Analysis

Recalling the homogeneous solutions, we see that, from eqn. (2.29) and (2.30), one such solution exists at *every point* of (\bar{m}, E, γ) space. However, our mean-field analysis has not yet provided any insight into their *stability*, with respect to small perturbations. In order to explore this issue, we must return to the full time-dependent set of equations, e.g., (2.22). To investigate the evolution of small harmonic perturbation about the homogeneous phase, $\bar{\phi} \equiv 1 - \bar{m}$, $\bar{\psi} \equiv 0$, we write

$$\begin{aligned}\phi(\mathbf{x}, t) &= \bar{\phi} + \sum_{\mathbf{k} \neq \mathbf{0}} \phi_{\mathbf{k}} e^{-\tau t + i\mathbf{k}\mathbf{x}} \\ \psi(\mathbf{x}, t) &= \sum_{\mathbf{k} \neq \mathbf{0}} \psi_{\mathbf{k}} e^{-\tau t + i\mathbf{k}\mathbf{x}},\end{aligned}\tag{2.42}$$

where $\mathbf{k} = (k_{\perp}, k_{\parallel}) = (\frac{2\pi n}{L_{\perp}}, \frac{2\pi m}{L_{\parallel}})$, with integer n, m , due to PBC. Assuming small amplitudes, $\phi_{\mathbf{k}}$ and $\psi_{\mathbf{k}}$, we may linearize (2.22) about the constant hole and charge densities. Defining

$$\boldsymbol{\xi}_{\mathbf{k}} \equiv \begin{pmatrix} \phi_{\mathbf{k}} \\ \psi_{\mathbf{k}} \end{pmatrix},\tag{2.43}$$

we write the linearized equation as

$$-\tau \boldsymbol{\xi}_{\mathbf{k}} = \mathbf{L}_{\mathbf{k}} \boldsymbol{\xi}_{\mathbf{k}},\tag{2.44}$$

where the matrix $\mathbf{L}_{\mathbf{k}}$ is given by

$$\mathbf{L}_{\mathbf{k}} = \begin{pmatrix} -\mathbf{k}\mathbf{\Gamma}\mathbf{k} & i\bar{\phi}\varepsilon\Gamma_{\parallel}k_{\parallel} \\ i[\gamma(1-\bar{\phi}) - (1-2\bar{\phi})]\varepsilon\Gamma_{\parallel}k_{\parallel} & -[\gamma(1-\bar{\phi}) + \bar{\phi}]\mathbf{k}\mathbf{\Gamma}\mathbf{k} \end{pmatrix}. \quad (2.45)$$

The diffusion matrix, $\mathbf{\Gamma}$, and the coarse-grained drive, ε , are given in eqns. (2.18) and (2.21). The two eigenvalues of $\mathbf{L}_{\mathbf{k}}$ determine the two branches of the dispersion relation, $\tau = \tau_{\mathbf{k}}^{\pm}$:

$$\tau_{\mathbf{k}}^{\pm} = -\frac{\text{Tr}(\mathbf{L}_{\mathbf{k}})}{2} \pm \sqrt{\left(\frac{\text{Tr}(\mathbf{L}_{\mathbf{k}})}{2}\right)^2 - \det(\mathbf{L}_{\mathbf{k}})}. \quad (2.46)$$

The homogeneous phase is stable as long as $\tau_{\mathbf{k}}^{\pm}$ (or its real part) is positive for each \mathbf{k} . Note that $-\frac{1}{2}\text{Tr}(\mathbf{L}_{\mathbf{k}}) = \frac{1}{2}[\gamma(1-\bar{\phi}) + 1 + \bar{\phi}]\mathbf{k}\mathbf{\Gamma}\mathbf{k}$ is positive definite, thus, regardless whether the “positive” square root in (2.46) is real or imaginary, the modes $\tau_{\mathbf{k}}^+$ are always stable against small harmonic fluctuations. The “lower” branch, $\tau_{\mathbf{k}}^-$, however, is only stable as long as $\det(\mathbf{L}_{\mathbf{k}}) > 0$. It is also easy to see that $\tau_{k_{\perp}=0}^{\pm} \propto k_{\perp}^2 > 0$. Further, since $\text{Re}\{\tau_{k_{\perp}=k_{\parallel}}^{\pm}\} > \text{Re}\{\tau_{0k_{\parallel}}^{\pm}\}$ and the most relevant perturbation is the one associated with the smallest positive eigenvalue, we need to focus only on the $k_{\perp} = 0$ modes. Not surprisingly, among this set, the slowest mode is associated with the lowest wave-vector, i.e., $k_{\parallel} = 2\pi/L_{\parallel}$. Setting $\tau_{02\pi/L_{\parallel}}^- = 0$ thus yields the first onset of instability. The result is that a specific homogeneous solution with mass density \bar{m} will become unstable when ε exceeds a critical $\varepsilon_H(\bar{m}, \gamma)$, given by $\det(\mathbf{L}_{02\pi/L_{\parallel}}) = 0$, i.e.,

$$\varepsilon_H L_{\parallel} = 2\pi \sqrt{\frac{1 - \bar{m} + \gamma\bar{m}}{(1 - \bar{m})[(2 - \gamma)\bar{m} - 1]}}. \quad (2.47)$$

Since (2.47) is real only in the range $\frac{1}{2-\gamma} \equiv \bar{m}_{min} < \bar{m} < 1$ and diverges at the end points, the homogeneous solutions are always stable outside this interval (or more directly, one can trace it back to $\det(\mathbf{L}_{\mathbf{k}}) > 0$ outside this interval). In particular, if $\gamma \geq 1$, they are always stable. For three smaller values of γ , the resulting linear stability boundary is plotted in Fig. 2.14. Since we have neglected nonlinear terms as well as fluctuations, we cannot identify eqn. (2.47) directly with the observed phase boundary (Fig. 2.2). However, it does mirror the shape of the transition line surprisingly well, and predicts, in particular, the vanishing of the ordered phase beyond a critical γ_{max} .

Of course, a linear stability analysis cannot provide us with information on the nature of the phase transition. In particular, if the transition is first order, this study yields at best the spinodal line. A similar stability analysis for the inhomogeneous phase is needed. If that state becomes unstable at the same points in the phase diagram, we claim that a continuous transition is present. If the stability limits occur at another line, we would identify that line with the second spinodal, so that the first order transitions would be located in between the two spinodals. Unfortunately, such a linear stability analysis for the

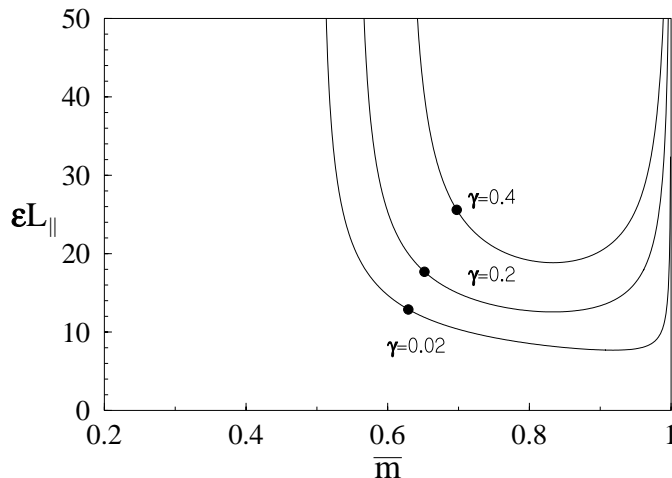


Figure 2.14: Mean-field linear stability boundary of the homogeneous phase in the $(\bar{m}, \varepsilon L_{\parallel})$ plane for three values of γ . For a fixed γ , the solid circle denotes the “tricritical” point $(\bar{m}_0(\gamma), L_{\parallel} \varepsilon_H(\gamma, \bar{m}_0))$, defined via $g(1 - \bar{m}_0, \gamma) = 0$.

inhomogeneous solutions is considerably more arduous and remains to be performed [37]. In its absence, we can obtain some insight into the nature of the transitions by going beyond the terms linear in perturbations about the homogeneous solution. In the next subsection, we show the results of this approach, which exploits the method of adiabatic elimination [38] to project an equation of motion for the slow mode out of the full non-linear dynamics (2.22).

2.3.4 Adiabatic Elimination of the Fast Modes

Next, we want to find an effective equation of motion for the slow mode (which is our order parameter) when approaching the linear stability boundary of the homogeneous phase. In the previous subsection we saw that in the limit $\tau_{02\pi/L_{\parallel}}^- \rightarrow 0^+$, there is only one slow mode, corresponding to this eigenvector of $\mathbf{L}_{\mathbf{k}}$. Let us denote it symbolically by M and we will give its precise definition below. At the linear level, all other modes will decay rapidly. Therefore, at the quadratic level (the only non-linearity in (2.22)), the only modes with

slow decay are those “driven” by M^2 . Our analysis shows that there is only one such mode, which, in turn, is coupled back to M through a non-linear term. The result is a non-linear equation of motion for M alone. In this subsection, we will give a few details of this approach [38].

As we will be dealing with non-linear contributions, we cannot make the same ansatz as in (2.42). Instead, we must write the fields ϕ , ψ and $\boldsymbol{\xi}$ with their full time dependence:

$$\begin{aligned}\phi(\mathbf{x}, t) &= \bar{\phi} + \sum_{\mathbf{k} \neq \mathbf{0}} \phi_{\mathbf{k}}(t) e^{i\mathbf{k}\mathbf{x}} \\ \psi(\mathbf{x}, t) &= \sum_{\mathbf{k} \neq \mathbf{0}} \psi_{\mathbf{k}}(t) e^{i\mathbf{k}\mathbf{x}},\end{aligned}\tag{2.48}$$

and

$$\boldsymbol{\xi}_{\mathbf{k}}(t) \equiv \begin{pmatrix} \phi_{\mathbf{k}}(t) \\ \psi_{\mathbf{k}}(t) \end{pmatrix}.\tag{2.49}$$

In Fourier space, eqn. (2.22) now takes the form:

$$\partial_t \boldsymbol{\xi}_{\mathbf{k}}(t) = \mathbf{L}_{\mathbf{k}} \boldsymbol{\xi}_{\mathbf{k}}(t) + \mathbf{N}_{\mathbf{k}}[\{\boldsymbol{\xi}_{\mathbf{k}'}(t)\}].\tag{2.50}$$

Here $\mathbf{N}_{\mathbf{k}}[\{\boldsymbol{\xi}_{\mathbf{k}'}(t)\}]$ is a two-component vector, representing the non-linear terms in Fourier space, quadratic in ϕ and ψ :

$$\mathbf{N}_{\mathbf{k}}[\{\boldsymbol{\xi}_{\mathbf{k}'}(t)\}] = \begin{pmatrix} N_{\mathbf{k}}^{\phi}[\{\boldsymbol{\xi}_{\mathbf{k}'}(t)\}] \\ N_{\mathbf{k}}^{\psi}[\{\boldsymbol{\xi}_{\mathbf{k}'}(t)\}] \end{pmatrix},\tag{2.51}$$

with

$$\begin{aligned}N_{\mathbf{k}}^{\phi}[\{\boldsymbol{\xi}_{\mathbf{k}'}(t)\}] &= i \varepsilon \Gamma_{\parallel} k_{\parallel} \sum_{\mathbf{k}'} \phi_{\mathbf{k}'}(t) \psi_{\mathbf{k}-\mathbf{k}'}(t) \\ N_{\mathbf{k}}^{\psi}[\{\boldsymbol{\xi}_{\mathbf{k}'}(t)\}] &= (1 - \gamma) \sum_{\mathbf{k}'} [\mathbf{k}' \Gamma \mathbf{k}' - (\mathbf{k} - \mathbf{k}') \Gamma (\mathbf{k} - \mathbf{k}')] \phi_{\mathbf{k}'}(t) \psi_{\mathbf{k}-\mathbf{k}'}(t) \\ &\quad + i \left(1 - \frac{\gamma}{2}\right) \varepsilon \Gamma_{\parallel} k_{\parallel} \sum_{\mathbf{k}'} \phi_{\mathbf{k}'}(t) \phi_{\mathbf{k}-\mathbf{k}'}(t) \\ &\quad + i \frac{\gamma}{2} \varepsilon \Gamma_{\parallel} k_{\parallel} \sum_{\mathbf{k}'} \psi_{\mathbf{k}'}(t) \psi_{\mathbf{k}-\mathbf{k}'}(t).\end{aligned}\tag{2.52}$$

From the discussion in the previous paragraph, it is clear that we will never need to consider the $k_{\perp} \neq 0$ sector. Focusing only on longitudinal modes, we define, for short:

$$\begin{aligned}\boldsymbol{\xi}_m &\equiv \boldsymbol{\xi}_0 \frac{2\pi m}{L_{\parallel}}(t) \\ \mathbf{L}_m &\equiv \mathbf{L}_0 \frac{2\pi m}{L_{\parallel}} \\ \mathbf{N}_m &\equiv \mathbf{N}_0 \frac{2\pi m}{L_{\parallel}}[\{\boldsymbol{\xi}_{\mathbf{k}'}(t)\}].\end{aligned}\tag{2.53}$$

Note that due to the reality of $\phi(\mathbf{x}, t)$ and $\psi(\mathbf{x}, t)$, $\boldsymbol{\xi}_{-m} = \boldsymbol{\xi}_m^*$.

In this notation, the slow mode is part of $\boldsymbol{\xi}_1$. If we denote the eigenvectors of \mathbf{L}_1 by \mathbf{e}^\pm , associated with the eigenvalues $\tau_{02\pi/L_\parallel}^\pm$, then the slow mode (M) can be identified through the decomposition

$$\boldsymbol{\xi}_1(t) = M(t)\mathbf{e}^- + F(t)\mathbf{e}^+ . \quad (2.54)$$

Explicitly (up to normalization),

$$\mathbf{e}^- = \left(\begin{array}{c} 1 \\ \frac{2\pi}{i\phi\varepsilon L_\parallel} \end{array} \right) . \quad (2.55)$$

By virtue of momentum conservation, we see from eqn. (2.52), that $\boldsymbol{\xi}_m$ couples only to $\boldsymbol{\xi}_n\boldsymbol{\xi}_{m-n}$, for all integer n . Near the transition, we expect that the dominant parts of all $\boldsymbol{\xi}_n$ $n > 1$ decay much faster than $\boldsymbol{\xi}_1$, since their corresponding eigenvalues stay finite while $\tau_{02\pi/L_\parallel}^- \rightarrow 0^+$. Therefore, in the long time limit, we may neglect products of two $\boldsymbol{\xi}_n$'s, with $n > 1$, and write:

$$\partial_t \boldsymbol{\xi}_1 \simeq \mathbf{L}_1 \boldsymbol{\xi}_1 + \mathbf{N}_1[\boldsymbol{\xi}_1^*, \boldsymbol{\xi}_2, \mathbf{0}, \dots, \mathbf{0}] \quad (2.56)$$

for the $n = 1$ case. In the same spirit, the only $\boldsymbol{\xi}_{n>1}$ which is coupled to $\boldsymbol{\xi}_1$ alone is the $n = 2$ case. Thus, we may neglect all equations except for

$$\partial_t \boldsymbol{\xi}_2 \simeq \mathbf{L}_2 \boldsymbol{\xi}_2 + \mathbf{N}_2[\boldsymbol{\xi}_1, \mathbf{0}, \mathbf{0}, \dots, \mathbf{0}] . \quad (2.57)$$

Being a linear, though inhomogeneous, equation for $\boldsymbol{\xi}_2$, it can be solved. In the long time limit (i.e., t comparable to $[\tau_{02\pi/L_\parallel}^-]^{-1}$ but much greater than the eigenvalues of \mathbf{L}_2^{-1}), $\partial_t \boldsymbol{\xi}_2 \simeq 0$, so the solution of (2.57) is $-\mathbf{L}_2^{-1} \mathbf{N}_2[\boldsymbol{\xi}_1, \mathbf{0}, \mathbf{0}, \dots, \mathbf{0}]$. Inserting this result into (2.56), we obtain an equation of motion for $\boldsymbol{\xi}_1$ only:

$$\partial_t \boldsymbol{\xi}_1 \simeq \mathbf{L}_1 \boldsymbol{\xi}_1 + \mathbf{N}_1[\boldsymbol{\xi}_1^*, -\mathbf{L}_2^{-1} \mathbf{N}_2[\boldsymbol{\xi}_1, \mathbf{0}, \mathbf{0}, \dots, \mathbf{0}], \mathbf{0}, \dots, \mathbf{0}] . \quad (2.58)$$

The final step consists of projecting (2.58) onto \mathbf{e}^- in order to extract an equation for the slow mode. Some care has to be taken here because \mathbf{L}_1 is not hermitian so that the appropriate left eigenvector (i.e., conjugate of \mathbf{e}^-) must be computed:

$$\mathbf{e}^{-\dagger} = \left(1 \quad , \quad \frac{2\pi}{i[\gamma(1-\phi)-(1-2\phi)]\varepsilon L_\parallel} \right) . \quad (2.59)$$

Meanwhile, since \mathbf{e}^+ is associated with a fast mode through the non-vanishing eigenvalue $\tau_{02\pi/L_\parallel}^+$, we may set $F(t) \simeq 0$ in the long time limit. Thus, from (2.54), we may approximate $\boldsymbol{\xi}_1$ by $M(t)\mathbf{e}^-$ when inserted into (2.58). The result, after tedious but straightforward algebra, is a Ginzburg-Landau type equation of motion for $M(t)$:

$$\partial_t M = - \left\{ \tau M + g |M|^2 M + \mathcal{O}(M^5) \right\} , \quad (2.60)$$

where $\tau \equiv \tau_{02\pi/L_{\parallel}}^-$ is the soft eigenvalue and g is a complicated function of ε , γ , $\bar{\phi}$ and L_{\parallel} . Since (2.60) is of interest only near the stability limit, where $\tau \simeq 0$, we approximate ε by ε_H here. Using (2.47) to eliminate ε_H , and remembering that $\bar{\phi} = 1 - \bar{m}$, we obtain an explicit expression, up to an overall positive constant:

$$\begin{aligned}
g(\bar{\phi}, \gamma) \propto & \left[23(1 - \gamma)^2(2 - \gamma)^2 \right] \bar{\phi}^4 \\
& + \left[30\gamma(1 - \gamma)(2 - \gamma)^2 - 44(1 - \gamma)^3(2 - \gamma) \right] \bar{\phi}^3 \\
& + \left[20(1 - \gamma)^4 - 64\gamma(1 - \gamma)^2(2 - \gamma) \right] \bar{\phi}^2 \\
& + \left[32\gamma(1 - \gamma)^3 - 6\gamma^2(1 - \gamma)(2 - \gamma) \right] \bar{\phi} \\
& + \left[5\gamma^2(1 - \gamma)^2 \right] .
\end{aligned} \tag{2.61}$$

We recognize (2.60) as the equation of motion for the dynamic model involving simple relaxation and the usual Landau-Ginzburg φ^4 Hamiltonian. Thus, the sign of g determines the order of the transition. If it is positive, the transition is continuous. On the other hand, $g < 0$ is indicative that a first order transition has presumably taken place *before* we arrive at this $\tau = 0$ point. In the physical range $0 < \bar{\phi} < \bar{\phi}_{max} \equiv 1 - \bar{m}_{min} = \frac{1-\gamma}{2-\gamma}$, we find a unique numerical solution for

$$g(\bar{\phi}, \gamma) = 0 , \tag{2.62}$$

at a critical hole density $\bar{\phi}_0(\gamma)$. Thus, we predict a crossover from a first order to a continuous transition as the mass density increases beyond $\bar{m}_0(\gamma) = 1 - \bar{\phi}_0(\gamma)$. One might label the point $(\bar{m}_0(\gamma), L_{\parallel}\varepsilon_H(\gamma, \bar{m}_0))$, marked by solid circles in Fig. 2.14, as a non-equilibrium "tricritical" point. However, we only use this terminology in the sense that for a given γ , this is the point on the phase boundary where the transition changes from being first order to being second order. In the (\bar{m}, E, γ) space, these points form a line of multicritical points.

For small γ , we may write the solution of (2.62) in terms of powers of γ , yielding

$$\bar{m}_0(\gamma) \simeq \frac{\sqrt{24}}{2(\sqrt{24} - 1)} + 0.05\gamma + \mathcal{O}(\gamma^2) . \tag{2.63}$$

It indicates that $\bar{m}_0(\gamma)$ increases with γ , as borne out by the simulations. On the other hand, if we introduce the "fraction" of the second order region to the whole line, characterized by $R(\gamma) \equiv \frac{\bar{\phi}_0(\gamma)}{\bar{\phi}_{max}(\gamma)}$, and solve (2.62) in terms of this ratio as $\gamma \rightarrow 1^-$, $R(\gamma)$ approaches $\frac{5}{6}$. So intriguingly, even for γ very close to 1, mean-field theory predicts a small yet finite region of first order transitions, though these have not been observed in the simulations (Fig. 2.2). Two obvious possibilities for resolving this discrepancy are (a) that these transitions are only weakly first order or (b) that they turn into continuous transitions once fluctuations are included into the theory.

During the adiabatic elimination we focused on purely longitudinal modes. One may, however, keep track of the full set of modes with $(k_{\perp}, \frac{2\pi}{L_{\parallel}})$ which in real space yields an effective equation of motion for a *complex* order parameter $M(x, t)$, in *one* (transverse) dimension. This equation of motion and the two component order parameter clearly resemble those of the equilibrium $O(2)$ or XY model [39] for which it is known that there is no long range order possible below three dimensions. In two dimensions it exhibits the Kosterlitz-Thouless transition [40] with power law correlations below a critical temperature, but no long range order results. Thus, the puzzle is: how this theory in one effective dimension can describe a phase transition observed in simulations. Some insight might be gained by introducing noise terms, representing fluctuations, and keeping them through the elimination process. Then the resulting Langevin equation has not only the usual additive noise term but also a multiplicative one. Clearly, this approach has potential and should be pursued.

2.3.5 Conductivity Near the Continuous Transitions

We saw in the previous two subsections that there is a single slow mode near the continuous transitions, M , which is related to the longest wavelength Fourier components of the hole and charge densities. Upon entering the inhomogeneous phase, $|M|$ is expected to increase continuously, thus being very small near the line of continuous transitions. This translates into the emergence of small amplitude harmonic hole and charge density profiles with wavelength L_{\parallel} , and this picture is entirely consistent with our observations from simulations near the continuous transitions (Fig. 2.12b). Using these findings we can derive an expression for the conductivity, j , near the continuous transitions, in the *inhomogeneous* phase as well, within the mean-field approximation. It can be most easily done by recalling the equation of motion for the variable $u(z)$ as defined in eqs. (2.35-2.37). In particular, we can expand $V(u)$ about its local minimum, \bar{u} , so that $u(z)$ exhibits a simple harmonic “motion”:

$$u(z) = \bar{u} - \delta \cos(kz) , \tag{2.64}$$

with

$$k^2 = \left. \frac{d^2V}{du^2} \right|_{\bar{u}} = \frac{2}{\gamma} \left[\left(j - \frac{\gamma}{2} \right) - (1 - \gamma) j \frac{1}{\bar{u}^2} \right] \tag{2.65}$$

and $0 < \delta \ll 1$. Then, up to the same order in δ , $\phi(z)$ and $\psi(z)$ will also be harmonic:

$$\phi(z) = \frac{\gamma}{\bar{u}^2 + \gamma - 1} + \frac{2\gamma\bar{u}}{(\bar{u}^2 + \gamma - 1)} \delta \cos(kz) \tag{2.66}$$

and

$$\psi(z) = \frac{2\bar{u}k}{\bar{u}^2 + \gamma - 1} \delta \sin(kz) . \tag{2.67}$$

Note that we chose δ to be positive, so that the phases of the hole and charge densities coincide with those of the simulation profiles in Fig. 2.12b. Now we must write down the conditions which relate the wave-number, k , to the longitudinal system size, L_{\parallel} , and \bar{u} to the average particle density \bar{m} . The former takes the form

$$k = \frac{2\pi}{\varepsilon L_{\parallel}}, \quad (2.68)$$

since $z = \varepsilon y$ was the rescaled length, while the latter follows from (2.66), after integrating over a period:

$$\frac{\gamma}{\bar{u}^2 + \gamma - 1} = 1 - \bar{m}. \quad (2.69)$$

Note that $\int dz \psi(z) = 0$ is trivially satisfied by (2.67). Inserting (2.68) into (2.65) and eliminating \bar{u} in favor of \bar{m} via (2.69), we obtain

$$j_I(\bar{m}, \varepsilon, \gamma) = \frac{1 - \bar{m} + \gamma \bar{m}}{2} \left[1 + \left(\frac{2\pi}{\varepsilon L_{\parallel}} \right)^2 \right], \quad (2.70)$$

where with the resurrection of the subscript I , we emphasize that this is the conductivity in the inhomogeneous phase. Finally, recalling eqn. (2.30),

$$j_H(\bar{m}, \gamma) = \bar{m}(1 - \bar{m}) + \frac{\gamma}{2} \bar{m}^2, \quad (2.71)$$

we can summarize the result for the conductivity:

$$j(\bar{m}, \varepsilon, \gamma) = \begin{cases} j_H(\bar{m}, \gamma) & \text{if } \varepsilon < \varepsilon_c(\bar{m}, \gamma) \\ j_I(\bar{m}, \varepsilon, \gamma) & \text{if } \varepsilon > \varepsilon_c(\bar{m}, \gamma) \end{cases}. \quad (2.72)$$

where $\varepsilon_c(\bar{m}, \gamma)$ is the surface of the continuous transitions. In this case, it is reasonable to assume that this surface coincides with the stability boundary of the homogeneous solutions (2.47), i.e.,

$$\varepsilon_c(\bar{m}, \gamma) = \varepsilon_H(\bar{m}, \gamma) = \frac{2\pi}{L_{\parallel}} \sqrt{\frac{1 - \bar{m} + \gamma \bar{m}}{(1 - \bar{m})[(2 - \gamma)\bar{m} - 1]}}. \quad (2.73)$$

Checking consistency, one can find that

$$j_I(\bar{m}, \varepsilon_H(\bar{m}, \gamma), \gamma) = j_H(\bar{m}, \gamma) \quad (2.74)$$

i.e., the current changes continuously through this transition. It is also easy to show that its derivatives are not continuous.

There are two scenarios in which we can qualitatively compare these findings to simulations. First, we keep \bar{m} and γ fixed, while varying ε . Equations (2.70-2.72) indicate that

for $\varepsilon < \varepsilon_c$ the conductivity is a (ε -independent) constant, while it decreases rapidly beyond ε_c , approaching some (small) constant value in the ordered phase. This is qualitatively the same behavior that we observe in Fig. 2.5b, Fig. 2.8c and Fig. 2.9c. Next, we fix \bar{m} and ε , and decrease γ . For both $\gamma > \gamma_c$ and $\gamma < \gamma_c$, the conductivity decreases *linearly* with γ , where γ_c can be computed explicitly from (2.73). Further, at γ_c , there is a discontinuity in the otherwise constant slope:

$$\frac{\partial j_H}{\partial \gamma} = \frac{\bar{m}^2}{2} \quad (2.75)$$

and

$$\frac{\partial j_I}{\partial \gamma} = \frac{\bar{m}}{2} \left[1 + \left(\frac{2\pi}{\varepsilon L_{\parallel}} \right)^2 \right]. \quad (2.76)$$

For $\bar{m} < 1$, we have

$$\frac{\partial j_H}{\partial \gamma} < \frac{\partial j_I}{\partial \gamma}. \quad (2.77)$$

The above behavior of the conductivity as a function of γ , agrees qualitatively with the data in Fig. 2.11: the slope suffers a jump at the transition, in such a way that its value is greater in the ordered (inhomogeneous) phase.

These two examples clearly demonstrate that the simple “harmonic” approximation for $u(z)$ (and consequently for $\phi(z)$ and $\psi(z)$) yields reasonable results for the conductivity as well, near the continuous transitions.

2.4 Summary

We have investigated, by both Monte Carlo simulations and continuum mean-field theory techniques, the collective behavior of a system of two species of particles driven into opposite directions by an external “electric” field, E . In this sense, we regard the particles as being oppositely “charged”. Extending earlier studies [26, 27, 28, 29], where particle-particle exchanges were prohibited, we allow such exchanges to occur at a fraction, γ , of the rate of particle-hole exchanges. As in the previous studies, regular lattices with periodic boundary conditions are used. Also, the particles are non-interacting except for the excluded volume constraint, and the particle numbers of the two species are equal and conserved. Apart from γ and E , the remaining control parameter is the overall density of particles, \bar{m} .

Exploring in the range $\gamma \leq 1$, we seek transitions from a disordered phase with homogeneous densities and large currents to a “locked-up” phase, characterized by inhomogeneous densities and small currents. First, we find a critical value, $\gamma_{max} \simeq 0.62$, beyond which the system remains *disordered* for all values of \bar{m} and E . In contrast, for $\gamma < \gamma_{max}$, excluded volume effects dominate, so that the transition to ordered states occurs for significantly large \bar{m} or E . A phase diagram is mapped out: a single sheet of transitions is present in

the $(\overline{m}, E, \gamma)$ space. The nature of the transitions is first order on parts of this sheet and continuous on other parts, with a line of multicritical points as the common boundary. To support these findings, we checked for discontinuities in the order parameters across the transitions, and looked for the presence of hysteresis. Further, we compiled histograms and inquired whether the distributions remain single-peaked or develop second peaks. The fluctuations were also measured and their divergence with system size was noted qualitatively. Since we have not performed extensive finite size analyses, we cannot present precise values for the various critical exponents, associated with the continuous transitions. Finally, we measured the profiles of both the hole and the charge densities in the ordered phase, emphasizing the characteristic differences between cases with $\gamma = 0$ and $\gamma > 0$.

Turning to analytic studies, we first derived a mean-field set of equations of motion for the two densities, based on the master equation for our simple hopping model. We then demonstrated the existence of homogeneous and inhomogeneous stationary solutions to these equations, corresponding to the disordered and ordered phase, respectively. The former follow trivially from conservation laws, while the latter can be found easily once the equations of motion have been recast in a form analogous to Newton's equation of motion for a particle in a potential. To confirm the presence of transitions between the two phases, we determined the linear stability boundary for the homogeneous solutions, noting that it mirrors the shape of the phase boundary, observed in simulations, rather closely. In particular, the homogeneous phase was found to be stable for sufficiently large γ . The adiabatic elimination of the fast modes provided us with a Ginzburg-Landau type of equation for the amplitude of the slow mode, thus giving us some insight into the nature of the transitions: in agreement with the simulation data, the transitions are first order for small \overline{m} , turning second order as the parameters are increased beyond a multicritical point. Also, while the location of this point shifts to higher values of \overline{m} as γ increases, the width of the first order region shrinks, approaching a finite fraction of the width of the whole transition region.

Relying on the “harmonic” approximation near the continuous transitions, we found an explicit form for the conductivity, which qualitatively agreed with simulations, in the corresponding regimes of the phase diagram.

Although the homogeneous phase was identified as the trivial solution of the equations of motion, even in this phase and far from criticality we expect to find generic and novel non-equilibrium behavior, once the fluctuations are incorporated. In the next Chapter, we present a way to “derive” the associated Langevin equations of the system so that we can go beyond the mean-field level, at least in the disordered phase.

Chapter 3

The Ω -expansion for the Two Species

In the previous Chapter we have already used a set of mean-field equations for the charge densities, supported by simple arguments. Now we provide a somewhat more systematic “derivation” of those equations. More importantly, we will also obtain a Fokker-Planck equation [41, 42] to model the fluctuating degrees of freedom which have been neglected so far. Alternatively, this can be translated to a set of Langevin equations [43]. It should be noted, however, that this approach is far from exact, since it contains the “coarse-graining” of the excluded volume constraint, which by itself, is somewhat self-contradictory. Therefore, its predictions should be compared to simulations in order to determine whether those equations of motion for the fast and slow variables capture correctly the long wavelength behavior of the two species model specified by the microscopic dynamics. In this Chapter, we use the terms slow and fast variables to distinguish between the mean-field densities and their fluctuations, respectively. We have already seen in Chapter 2 that the mean-field theory works remarkably well. A similar comparison will be performed in Chapter 4 concerning structure factors (correlations in momentum space).

3.1 Expansion of the Master Equation

Introduced by van Kampen [44], there is a systematic way to obtain equations of motions at the mesoscopic level, starting from the “precise” microscopic dynamics. This method, called the Ω -expansion, can be easily generalized for many-particle systems, e.g. reaction-diffusion systems [45]. To avoid unnecessary complications, we will illustrate this method in one dimension with an external drive, since it can be trivially extended to $(d - 1) + 1$ dimensions. We start with a discrete lattice, with sites labeled $1, 2, \dots, M$. We divide the system into M/Ω equal size blocks and label them by the site which is in their center. Now a configuration can be specified by the coarse-grained variables, $\{N_i^\pm\}$, the total numbers of \pm particles in block i . For convenience, we can relabel the sites so that their index runs

$1, 2, \dots, L$, where $L = M/\Omega$. The probability of finding the system in “configuration”

$$\begin{bmatrix} N^+ \\ N^- \end{bmatrix} \equiv \begin{bmatrix} \dots, & N_i^+, & N_{i+1}^+, & \dots \\ \dots, & N_i^-, & N_{i+1}^-, & \dots \end{bmatrix} \quad (3.1)$$

at time t is now given by the coarse-grained probability density

$$P\left(t, \begin{bmatrix} N^+ \\ N^- \end{bmatrix}\right) = P\left(t, \begin{bmatrix} \dots, & N_i^+, & N_{i+1}^+, & \dots \\ \dots, & N_i^-, & N_{i+1}^-, & \dots \end{bmatrix}\right). \quad (3.2)$$

In the following, we will generally suppress the explicit t dependence in P .

If we choose Ω such that the blocks are *macroscopically small* subsystems of the original one, then we expect N_i^\pm to consist of a macroscopic part $\Omega \rho_i^\pm(t)$ plus fluctuations of order $\Omega^{1/2}$. That is, P will have a sharp peak located roughly at $\{\Omega \rho_i^\pm(t)\}$ in the configuration space with a width of order $\Omega^{1/2}$. The term *macroscopically small*, should be understood in the following sense. Assuming that we are not close to a phase transition, the correlation length ξ in the system is expected to be finite in terms of the original lattice constant, i.e., $1 < \xi \ll \infty$. On this length scale, the particle densities should not vary significantly, so that it is reasonable to coarse-grain over blocks of size $\Omega \sim \xi$. This idea forms the basis of a systematic expansion. Accordingly, we split the number of particles in $b(i)$, the block centered about site i , into a *macroscopic* part ($\Omega \rho_i^\pm(t)$) and a *fluctuating* one ($\Omega^{1/2} \chi_i^\pm$):

$$N_i^\pm = \sum_{i' \in b(i)} n_{i'}^\pm = \Omega \rho_i^\pm(t) + \Omega^{1/2} \chi_i^\pm. \quad (3.3)$$

To proceed, first we need to write a master equation for the coarse-grained probability density.

To display more transparently the effect of the drive, we rewrite the transition rates and the overall time scale, so that the resulting new parameters describe the model equivalently to the microscopic dynamics given by eqs. (2.3,2.4). Then, once a particle-hole or particle-particle pair is chosen, the exchanges take place with the rates

$$\begin{aligned} W_{ph} &= 2\Gamma p^\pm \\ W_{pp} &= 2\gamma\Gamma p^\pm, \end{aligned} \quad (3.4)$$

respectively, where

$$\begin{aligned} \Gamma &= \frac{1}{2} (1 + e^{-|E|}) \\ p^\pm &= \frac{1}{2} \left(1 \pm \frac{\varepsilon}{2}\right) \\ \varepsilon &= 2 \tanh(E/2). \end{aligned} \quad (3.5)$$

In eqns. (3.4) + or - must be chosen depending on whether the exchange takes place along or against the “force”. After incorporating coarse-graining and imposing periodic boundary conditions, we can write the six basic exchange processes in the following form:

$$\begin{aligned}
W_{i,i+1}^{+0} \begin{bmatrix} N^+ \\ N^- \end{bmatrix} &= N_i^+ (\Omega - N_{i+1}^+ - N_{i+1}^-) 2\Gamma p^+ \\
W_{i,i+1}^{0+} \begin{bmatrix} N^+ \\ N^- \end{bmatrix} &= (\Omega - N_i^+ - N_i^-) N_{i+1}^+ 2\Gamma p^- \\
W_{i,i+1}^{-0} \begin{bmatrix} N^+ \\ N^- \end{bmatrix} &= N_i^- (\Omega - N_{i+1}^+ - N_{i+1}^-) 2\Gamma p^- \\
W_{i,i+1}^{0-} \begin{bmatrix} N^+ \\ N^- \end{bmatrix} &= (\Omega - N_i^+ - N_i^-) N_{i+1}^- 2\Gamma p^+ \\
W_{i,i+1}^{+-} \begin{bmatrix} N^+ \\ N^- \end{bmatrix} &= N_i^+ N_{i+1}^- 2\gamma\Gamma p^+ \\
W_{i,i+1}^{-+} \begin{bmatrix} N^+ \\ N^- \end{bmatrix} &= N_i^- N_{i+1}^+ 2\gamma\Gamma p^- .
\end{aligned} \tag{3.6}$$

For example, the first transition rate, $W_{i,i+1}^{+0}$, originates from the exact microscopic jump rate, $n_i^+(1 - n_{i+1}^+ - n_{i+1}^-) 2\Gamma p^+$. Then the master equation can be written as follows:

$$\begin{aligned}
\partial_t P \begin{bmatrix} N^+ \\ N^- \end{bmatrix} &= \\
&- \sum_i P \begin{bmatrix} N^+ \\ N^- \end{bmatrix} \left\{ W_{i,i+1}^{+0} \begin{bmatrix} N^+ \\ N^- \end{bmatrix} + W_{i,i+1}^{0+} \begin{bmatrix} N^+ \\ N^- \end{bmatrix} + W_{i,i+1}^{-0} \begin{bmatrix} N^+ \\ N^- \end{bmatrix} + W_{i,i+1}^{0-} \begin{bmatrix} N^+ \\ N^- \end{bmatrix} \right\} \\
&+ \sum_i P \begin{bmatrix} N_i^+ + 1, & N_{i+1}^+ - 1 \\ N_i^-, & N_{i+1}^- \end{bmatrix} W_{i,i+1}^{+0} \begin{bmatrix} N_i^+ + 1, & N_{i+1}^+ - 1 \\ N_i^-, & N_{i+1}^- \end{bmatrix} \\
&+ \sum_i P \begin{bmatrix} N_i^+ - 1, & N_{i+1}^+ + 1 \\ N_i^-, & N_{i+1}^- \end{bmatrix} W_{i,i+1}^{0+} \begin{bmatrix} N_i^+ - 1, & N_{i+1}^+ + 1 \\ N_i^-, & N_{i+1}^- \end{bmatrix} \\
&+ \sum_i P \begin{bmatrix} N_i^+, & N_{i+1}^+ \\ N_i^- + 1, & N_{i+1}^- - 1 \end{bmatrix} W_{i,i+1}^{-0} \begin{bmatrix} N_i^+, & N_{i+1}^+ \\ N_i^- + 1, & N_{i+1}^- - 1 \end{bmatrix} \\
&+ \sum_i P \begin{bmatrix} N_i^+, & N_{i+1}^+ \\ N_i^- - 1, & N_{i+1}^- + 1 \end{bmatrix} W_{i,i+1}^{0-} \begin{bmatrix} N_i^+, & N_{i+1}^+ \\ N_i^- - 1, & N_{i+1}^- + 1 \end{bmatrix} \\
&- \sum_i P \begin{bmatrix} N^+ \\ N^- \end{bmatrix} \left\{ W_{i,i+1}^{+-} \begin{bmatrix} N^+ \\ N^- \end{bmatrix} + W_{i,i+1}^{-+} \begin{bmatrix} N^+ \\ N^- \end{bmatrix} \right\} \\
&+ \sum_i P \begin{bmatrix} N_i^+ + 1, & N_{i+1}^+ - 1 \\ N_i^- - 1, & N_{i+1}^- + 1 \end{bmatrix} W_{i,i+1}^{+-} \begin{bmatrix} N_i^+ + 1, & N_{i+1}^+ - 1 \\ N_i^- - 1, & N_{i+1}^- + 1 \end{bmatrix} \\
&+ \sum_i P \begin{bmatrix} N_i^+ - 1, & N_{i+1}^+ + 1 \\ N_i^- + 1, & N_{i+1}^- - 1 \end{bmatrix} W_{i,i+1}^{-+} \begin{bmatrix} N_i^+ - 1, & N_{i+1}^+ + 1 \\ N_i^- + 1, & N_{i+1}^- - 1 \end{bmatrix} .
\end{aligned} \tag{3.7}$$

Note that in the “gain” terms, we explicitly specified the i^{th} and the $(i+1)^{\text{th}}$ arguments of P and W ’s, since they differ from N_i^\pm and N_{i+1}^\pm . These arguments correspond to the occupation numbers *from which* $[N^+, N^-]$ could possibly result.

Next, we expand the right hand side of (3.7) about the configuration $[N^+, N^-]$. It is easy to see that for each “loss” term there is a “gain” term, which has the same functional form, but with $N_i^\pm \pm 1$ instead of N_i^\pm . After omitting higher than second order derivatives, the expansion of the master equation takes the form:

$$\begin{aligned}
\partial_t P = & \\
& \sum_i \left\{ \frac{\partial}{\partial N_i^+} - \frac{\partial}{\partial N_{i+1}^+} + \frac{1}{2} \left(\frac{\partial^2}{\partial (N_i^+)^2} + \frac{\partial^2}{\partial (N_{i+1}^+)^2} - 2 \frac{\partial^2}{\partial N_i^+ \partial N_{i+1}^+} \right) \right\} P W_{i,i+1}^{+0} + \\
& \sum_i \left\{ -\frac{\partial}{\partial N_i^+} + \frac{\partial}{\partial N_{i+1}^+} + \frac{1}{2} \left(\frac{\partial^2}{\partial (N_i^+)^2} + \frac{\partial^2}{\partial (N_{i+1}^+)^2} - 2 \frac{\partial^2}{\partial N_i^+ \partial N_{i+1}^+} \right) \right\} P W_{i,i+1}^{0+} + \\
& \sum_i \left\{ \frac{\partial}{\partial N_i^-} - \frac{\partial}{\partial N_{i+1}^-} + \frac{1}{2} \left(\frac{\partial^2}{\partial (N_i^-)^2} + \frac{\partial^2}{\partial (N_{i+1}^-)^2} - 2 \frac{\partial^2}{\partial N_i^- \partial N_{i+1}^-} \right) \right\} P W_{i,i+1}^{-0} + \\
& \sum_i \left\{ -\frac{\partial}{\partial N_i^-} + \frac{\partial}{\partial N_{i+1}^-} + \frac{1}{2} \left(\frac{\partial^2}{\partial (N_i^-)^2} + \frac{\partial^2}{\partial (N_{i+1}^-)^2} - 2 \frac{\partial^2}{\partial N_i^- \partial N_{i+1}^-} \right) \right\} P W_{i,i+1}^{0-} + \\
& \sum_i \left\{ \frac{\partial}{\partial N_i^+} - \frac{\partial}{\partial N_{i+1}^+} + \frac{1}{2} \left(\frac{\partial^2}{\partial (N_i^+)^2} + \frac{\partial^2}{\partial (N_{i+1}^+)^2} - 2 \frac{\partial^2}{\partial N_i^+ \partial N_{i+1}^+} \right) + \right. \tag{3.8} \\
& \quad \left. -\frac{\partial}{\partial N_i^-} + \frac{\partial}{\partial N_{i+1}^-} + \frac{1}{2} \left(\frac{\partial^2}{\partial (N_i^-)^2} + \frac{\partial^2}{\partial (N_{i+1}^-)^2} - 2 \frac{\partial^2}{\partial N_i^- \partial N_{i+1}^-} \right) + \right. \\
& \quad \left. \left(-\frac{\partial^2}{\partial N_i^+ \partial N_i^-} - \frac{\partial^2}{\partial N_{i+1}^+ \partial N_{i+1}^-} + \frac{\partial^2}{\partial N_i^- \partial N_{i+1}^+} + \frac{\partial^2}{\partial N_i^+ \partial N_{i+1}^-} \right) \right\} P W_{i,i+1}^{+-} + \\
& \sum_i \left\{ -\frac{\partial}{\partial N_i^+} + \frac{\partial}{\partial N_{i+1}^+} + \frac{1}{2} \left(\frac{\partial^2}{\partial (N_i^+)^2} + \frac{\partial^2}{\partial (N_{i+1}^+)^2} - 2 \frac{\partial^2}{\partial N_i^+ \partial N_{i+1}^+} \right) + \right. \\
& \quad \left. + \frac{\partial}{\partial N_i^-} - \frac{\partial}{\partial N_{i+1}^-} + \frac{1}{2} \left(\frac{\partial^2}{\partial (N_i^-)^2} + \frac{\partial^2}{\partial (N_{i+1}^-)^2} - 2 \frac{\partial^2}{\partial N_i^- \partial N_{i+1}^-} \right) + \right. \\
& \quad \left. \left(-\frac{\partial^2}{\partial N_i^+ \partial N_i^-} - \frac{\partial^2}{\partial N_{i+1}^+ \partial N_{i+1}^-} + \frac{\partial^2}{\partial N_i^- \partial N_{i+1}^+} + \frac{\partial^2}{\partial N_i^+ \partial N_{i+1}^-} \right) \right\} P W_{i,i+1}^{-+},
\end{aligned}$$

where now P and the W ’s are all taken at the “original” $[N^+, N^-]$ configuration.

Returning to the main idea of the Ω -expansion, our new set of stochastic variables will be the density fluctuations, $\{\chi_i^\pm\}$:

$$\begin{aligned}
P\left(t, \begin{bmatrix} N^+ \\ N^- \end{bmatrix}\right) \Delta N_1^+ \dots \Delta N_L^+ \Delta N_1^- \dots \Delta N_L^- = \\
\Pi\left(t, \begin{bmatrix} \chi^+ \\ \chi^- \end{bmatrix}\right) \Delta \chi_1^+ \dots \Delta \chi_L^+ \Delta \chi_1^- \dots \Delta \chi_L^-,
\end{aligned} \tag{3.9}$$

so that, using (3.3)

$$\Omega^L P\left(t, \begin{bmatrix} \{\Omega \rho_i^+(t) + \Omega^{1/2} \chi_i^+\} \\ \{\Omega \rho_i^-(t) + \Omega^{1/2} \chi_i^-\} \end{bmatrix}\right) = \Pi\left(t, \begin{bmatrix} \{\chi_i^+\} \\ \{\chi_i^-\} \end{bmatrix}\right). \tag{3.10}$$

According to (3.3) and (3.10) we have to carry out the transformation of the master equation (3.8). Some care has to be taken, since now P depends on t not only explicitly but also through $\{\rho_i^\pm(t)\}$. Following the rules of differentiation one can easily find

$$\frac{\partial}{\partial N_i^\pm} = \Omega^{-1/2} \frac{\partial}{\partial \chi_i^\pm} \tag{3.11}$$

and

$$\Omega^L \partial_t P = \partial_t \Pi - \Omega^{1/2} \partial_t \rho_i^\alpha \frac{\partial \Pi}{\partial \chi_i^\alpha}, \tag{3.12}$$

where $\alpha = +, -$ and summation over repeated indices is implied in (3.12) and in the following. Now we insert (3.3) into (3.8) and use (3.11) and (3.12). For simplicity, we multiply both sides of (3.8) by Ω^L and rescale time by absorbing a factor Ω into t . Then we rearrange the terms in decreasing order of powers of Ω such that the master equation takes the form

$$0 = \{\dots\} \Omega^{1/2} + \{\dots\} \Omega^0 + \mathcal{O}\left(\Omega^{-1/2}\right), \tag{3.13}$$

where the $\{\dots\}$'s depend explicitly on $\{\rho_i^\pm(t)\}$, $\{\chi_i^\pm\}$ and implicitly on them through Π . We will require that the ‘‘coefficients’’ of the first two terms vanish identically, while we neglect lower orders, in order to satisfy (3.13). In the following two subsections we present the results for the two leading order terms of the Ω -expansion. It is now clear why we dropped higher than second order derivatives in (3.8): they would only generate lower order contributions as can be easily seen from (3.11).

3.1.1 Mean-field Equations of Motion

The largest term is of order $\Omega^{1/2}$. For its coefficient, which must vanish, we find:

$$\left(\partial_t \rho_i^\alpha - F_i^\alpha[\{\rho_j^\beta\}]\right) \frac{\partial \Pi}{\partial \chi_i^\alpha} = 0, \tag{3.14}$$

where

$$\begin{aligned}
F_i^\pm [\{\rho_j^\beta\}] = & \\
& -\Gamma \left\{ \left[\rho_i^\pm (\phi_{i+1} + \phi_{i-1}) - \phi_i (\rho_{i+1}^\pm + \rho_{i-1}^\pm) \right] + \right. \\
& \left. \pm \frac{\varepsilon}{2} \left[\rho_i^\pm (\phi_{i+1} - \phi_{i-1}) + \phi_i (\rho_{i+1}^\pm - \rho_{i-1}^\pm) \right] \right\} \\
& -\gamma \Gamma \left\{ \left[\rho_i^\pm (\rho_{i+1}^\mp + \rho_{i-1}^\mp) - \rho_i^\mp (\rho_{i+1}^\pm + \rho_{i-1}^\pm) \right] + \right. \\
& \left. \pm \frac{\varepsilon}{2} \left[\rho_i^\pm (\rho_{i+1}^\mp - \rho_{i-1}^\mp) + \rho_i^\mp (\rho_{i+1}^\pm - \rho_{i-1}^\pm) \right] \right\}
\end{aligned} \tag{3.15}$$

and $\phi_i(t) = 1 - \rho_i^+(t) - \rho_i^-(t)$ is the hole density. Thus, the average particle densities must satisfy the equation:

$$\partial_t \rho_i^\alpha = F_i^\alpha [\{\rho_j^\beta\}]. \tag{3.16}$$

These are just the mean-field equations of motions of the two species model that we have already encountered in Chapter 2. We can easily extend the result to $(d-1)+1$ dimensions, where the field points e.g. along the d^{th} axis and there are $d-1$ transverse dimensions. To simplify the formulas, we take a naive continuum limit, so that $\{\rho_i^\pm(t)\} \rightarrow \rho^\pm(\mathbf{x}, t)$:

$$\partial_t \rho^\pm = -\nabla \Gamma \left\{ [\rho^\pm \overset{\leftrightarrow}{\nabla} \phi \pm \varepsilon \hat{\mathbf{x}}_{\parallel} \rho^\pm \phi] + \gamma [\rho^\pm \overset{\leftrightarrow}{\nabla} \rho^\mp \pm \varepsilon \hat{\mathbf{x}}_{\parallel} \rho^\pm \rho^\mp] \right\}, \tag{3.17}$$

where

$$\Gamma = \begin{pmatrix} \mathbf{\Gamma}_{\perp} & \mathbf{0} \\ \mathbf{0} & \Gamma_{\parallel} \end{pmatrix} = \begin{pmatrix} \mathbf{1} & \mathbf{0} \\ \mathbf{0} & \frac{1+e^{-|E|}}{2} \end{pmatrix} \tag{3.18}$$

is the diffusion-matrix, which is manifestly isotropic in the $d-1$ dimensional transverse subspace. $\overset{\leftrightarrow}{\nabla}$ is again the asymmetric gradient operator. $\varepsilon = 2 \tanh(E/2)$ is the coarse-grained bias and $\hat{\mathbf{x}}_{\parallel}$ is the unit vector along the x_{\parallel} direction.

3.1.2 The Fokker-Planck Equation

The second largest term in (3.13) is of order Ω^0 and its coefficient, which must vanish, yields a Fokker-Planck equation for Π . Here, we will only focus on the case where the mean-field densities are homogeneous. It is clear from (3.15,3.16) that time-independent, uniform densities, $\rho_i^\pm(t) = \bar{\rho}$, always satisfy the mean-field equations. Thus, the fast variables will now correspond to the fluctuations about these constant densities, i.e., the fluctuations in the disordered phase of the system. Then, still in one dimension, we find the following Fokker-Planck equation for Π :

$$\partial_t \Pi = \frac{\partial}{\partial \chi_i^\alpha} (\mathcal{L}_i^\alpha [\{\chi_l^\gamma\}] \Pi) + d_{ij}^{\alpha\beta} \frac{\partial^2 \Pi}{\partial \chi_i^\alpha \partial \chi_j^\beta}. \tag{3.19}$$

The coefficient under the first derivative, \mathcal{L}_i^α , is called the “drift” coefficient, and is given by

$$\begin{aligned} \mathcal{L}_i^\pm [\{\chi_l^\gamma\}] = & \Gamma \left\{ \left[(1 - \bar{\rho}) (\chi_{i+1}^\pm + \chi_{i-1}^\pm - 2\chi_i^\pm) + \bar{\rho} (\chi_{i+1}^\mp + \chi_{i-1}^\mp - 2\chi_i^\mp) \right] + \right. \\ & \left. \pm \frac{\varepsilon}{2} \left[(1 - 3\bar{\rho}) (\chi_{i+1}^\pm - \chi_{i-1}^\pm) + \bar{\rho} (\chi_{i+1}^\mp - \chi_{i-1}^\mp) \right] \right\} \\ \gamma \Gamma \left\{ \left[\bar{\rho} (\chi_{i+1}^\pm + \chi_{i-1}^\pm - 2\chi_i^\pm) - \bar{\rho} (\chi_{i+1}^\mp + \chi_{i-1}^\mp - 2\chi_i^\mp) \right] + \right. \\ & \left. \pm \frac{\varepsilon}{2} \left[-\bar{\rho} (\chi_{i+1}^\pm - \chi_{i-1}^\pm) - \bar{\rho} (\chi_{i+1}^\mp - \chi_{i-1}^\mp) \right] \right\} . \end{aligned} \quad (3.20)$$

The “diffusion” or “noise” coefficient, the coefficient of the second derivative, is

$$d_{ij}^{\alpha\beta} = \sigma^{\alpha\beta} (2\delta_{ij} - \delta_{i+1j} - \delta_{i-1j}) \quad (3.21)$$

with

$$(\sigma^{\alpha\beta}) = \begin{pmatrix} \sigma^{++} & \sigma^{+-} \\ \sigma^{-+} & \sigma^{--} \end{pmatrix} = \Gamma \begin{pmatrix} \bar{\rho}(1 - 2\bar{\rho}) + \gamma \bar{\rho}^2 & -\gamma \bar{\rho}^2 \\ -\gamma \bar{\rho}^2 & \bar{\rho}(1 - 2\bar{\rho}) + \gamma \bar{\rho}^2 \end{pmatrix} . \quad (3.22)$$

Here and in the following, δ_{ij} denotes the Kronecker-symbol. It is important to note that the drift term is linear in the χ 's and the diffusion coefficient does not depend on them. In particular, $\mathcal{L}_i^\alpha [\{\chi_l^\gamma\}]$ is just the linearization of $F_i^\alpha [\{\rho_l^\gamma\}]$ about the homogeneous densities! Equation (3.19) governs the fluctuations of order $\Omega^{1/2}$ in the disordered phase.

3.2 The Associated Langevin Equations

There exists an equivalent framework in which one can study fluctuations about the macroscopic (mean-field) densities. Instead of the probability density $\Pi(t, \{\chi_i^\alpha\})$ which specifies the probability of the configuration $\{\chi_i^\alpha\}$ at time t , one can treat the χ 's as time-dependent stochastic variables, $\{\chi_i^\alpha(t)\}$, in principle described by a probability density functional $P[\{\chi_i^\alpha(t)\}]$. For our purposes, this other framework, the equivalent Langevin equations, is more transparent. Since the diffusion coefficient does not depend on the χ 's, it is straightforward to obtain the associated set of stochastic differential equations [46] which is equivalent to the Fokker-Planck equation (3.19):

$$\partial_t \chi_i^\alpha = \mathcal{L}_i^\alpha [\{\chi_l^\gamma\}] - g_{ij}^{\alpha\beta} \xi_j^\beta . \quad (3.23)$$

Here, the ξ 's are uncorrelated, Gaussian noise terms with zero mean, i.e.,

$$\langle \xi_i^\alpha(t) \rangle = 0 , \quad \langle \xi_i^\alpha(t) \xi_j^\beta(t') \rangle = 2\delta^{\alpha\beta} \delta_{ij} \delta(t - t') \quad (3.24)$$

and

$$g_{ik}^{\alpha\gamma} g_{jk}^{\beta\gamma} = d_{ij}^{\alpha\beta} . \quad (3.25)$$

Similar to δ_{ij} , $\delta^{\alpha\beta}$ is the Kronecker-symbol for the charge degrees of freedom, while $\delta(t-t')$ is the (Dirac) δ -function. First we need to find a solution for (3.25). It is useful to recall from (3.21), that $d_{ij}^{\alpha\beta}$ is the direct product of two matrices, associated with the charge and spatial degrees of freedom, respectively. Thus, when solving for $g_{ij}^{\alpha\beta}$, we expect it to have a similar structure. Furthermore, by noticing that

$$(\delta_{ik} - \delta_{i-1k}) (\delta_{jk} - \delta_{j-1k}) = 2\delta_{ij} - \delta_{i+1j} - \delta_{i-1j} , \quad (3.26)$$

we can write it as

$$g_{ij}^{\alpha\beta} = g^{\alpha\beta} (\delta_{ij} - \delta_{i-1,j}) . \quad (3.27)$$

Now, what is left to be solved is

$$g^{\alpha\gamma} g^{\beta\gamma} = \sigma^{\alpha\beta} . \quad (3.28)$$

Since $\sigma^{\alpha\beta}$ is a 2×2 positive definite, symmetric matrix, it is easy to find the square root of it by diagonalization. This procedure would simply yield a symmetric $g^{\alpha\beta}$. Note that this would not be a unique solution, because multiplying $g^{\alpha\beta}$ by an orthogonal matrix would satisfy (3.28) as well. However, an explicit solution for $g^{\alpha\beta}$ is not needed, since we can define a new set of Gaussian random variables as a linear combination of the old ones:

$$\eta_i^\alpha(t) \equiv g^{\alpha\beta} \xi_i^\beta(t) . \quad (3.29)$$

Then, using (3.24) and (3.28), it easily follows that

$$\langle \eta_i^\alpha(t) \rangle = 0 , \quad \langle \eta_i^\alpha(t) \eta_j^\beta(t') \rangle = 2\sigma^{\alpha\beta} \delta_{ij} \delta(t-t') . \quad (3.30)$$

and the Langevin equation takes the form:

$$\partial_t \chi_i^\alpha = \mathcal{L}_i^\alpha [\{\chi_l^\gamma\}] - (\delta_{ij} - \delta_{i-1j}) \eta_j^\alpha . \quad (3.31)$$

It is important to note that this equation together with (3.20), explicitly reflects the conserved microscopic dynamics at the coarse-grained level. Similar to the mean-field equations, we extend the result to $(d-1)+1$ dimensions and take the continuum limit, i.e., $\{\chi_i^\pm(t)\} \rightarrow \chi^\pm(\mathbf{x}, t)$:

$$\partial_t \chi^\alpha(\mathbf{x}, t) = \mathcal{L}^{\alpha\beta}(\nabla) \chi^\beta(\mathbf{x}, t) - \nabla \eta^\alpha(\mathbf{x}, t) , \quad (3.32)$$

where

$$(\mathcal{L}^{\alpha\beta}(\nabla)) = \begin{pmatrix} (1 - \tilde{\rho}) \nabla \Gamma \nabla - (1 - \delta \tilde{\rho}) \varepsilon \Gamma_{\parallel} \partial_{\parallel} & \tilde{\rho} \nabla \Gamma \nabla + \tilde{\rho} \varepsilon \Gamma_{\parallel} \partial_{\parallel} \\ \tilde{\rho} \nabla \Gamma \nabla - \tilde{\rho} \varepsilon \Gamma_{\parallel} \partial_{\parallel} & (1 - \tilde{\rho}) \nabla \Gamma \nabla + (1 - \delta \tilde{\rho}) \varepsilon \Gamma_{\parallel} \partial_{\parallel} \end{pmatrix} \quad (3.33)$$

and we have defined the “reduced” average density $\tilde{\rho} \equiv (1 - \gamma)\bar{\rho}$ and $\delta \equiv (3 - \gamma)/(1 - \gamma)$. $\mathbf{\Gamma}$ is the diffusion matrix, given in (3.18). $\boldsymbol{\eta}^\pm(\mathbf{x}, t)$ are Gaussian, white noise terms, in continuous space and time:

$$\langle \eta_i^\alpha(\mathbf{x}, t) \rangle = 0, \quad \langle \eta_i^\alpha(\mathbf{x}, t) \eta_j^\beta(\mathbf{x}', t') \rangle = 2\sigma_{ij}^{\alpha\beta} \delta(\mathbf{x} - \mathbf{x}') \delta(t - t'), \quad (3.34)$$

where $\alpha, \beta = +, -$; $i, j = 1, 2, \dots, d$ and $(\sigma_{ij})^{\alpha\beta} = \boldsymbol{\sigma}^{\alpha\beta}$ are the noise matrices:

$$\boldsymbol{\sigma}^{\alpha\beta} = \begin{pmatrix} \boldsymbol{\sigma}_\perp^{\alpha\beta} & \mathbf{0} \\ \mathbf{0} & \sigma_\parallel^{\alpha\beta} \end{pmatrix}. \quad (3.35)$$

It is clear that these matrices are diagonal but not proportional to the unit matrix. At this level, we have an explicit form for them, in terms of the diffusion matrix:

$$\begin{aligned} \boldsymbol{\sigma}^{++} &= [\bar{\rho}(1 - 2\bar{\rho}) + \gamma\bar{\rho}^2] \mathbf{\Gamma} \\ \boldsymbol{\sigma}^{+-} &= [-\gamma\bar{\rho}^2] \mathbf{\Gamma}. \end{aligned} \quad (3.36)$$

Thus, similar to $\mathbf{\Gamma}$, $\boldsymbol{\sigma}^{\alpha\beta}$ is also isotropic in the $d - 1$ dimensional transverse subspace.

3.3 Some General Remarks

In this section, we briefly comment on the effect of higher order terms in the Ω -expansion (3.13). These provide corrections to the Fokker-Planck equation, leading to the following modifications.

- (i.) The drift coefficient becomes nonlinear in the χ 's.
- (ii.) The diffusion coefficient acquires a χ -dependence.
- (iii.) The differential equation for Π will now contain higher than second order derivatives with respect to the χ 's, thus, it will no longer be a Fokker-Planck equation.

Note that all these corrections are of $\mathcal{O}(\Omega^{-1/2})$ compared to the leading terms. One major problem with (iii.) is that it allows negative values for the probability density Π . Although it can have some use in certain applications [46], for most problems we can drop these higher order derivatives and stay with a Fokker-Planck equation. On the other hand, keeping (i.) and (ii.) only is not systematic in the spirit of the Ω -expansion but physically reasonable in most cases. The resulting equivalent Langevin equation with nonlinear deterministic (drift) term and with additive and/or multiplicative noise terms [46] has been widely used to describe various physical systems. Another drawback of the Ω -expansion is that, for realistic models, it is not easily done in practice. For systems with more complicated interactions and dynamics, the difficulty of performing the Ω -expansion, or similar systematic derivations starting from the microscopics, is insurmountable. In these

cases, finding the deterministic part can be supported by some macroscopic balance equations, containing the symmetries of the system, while finding the noise term requires some extra intuition. In equilibrium, however, the latter can also be given explicitly by virtue of the FDT. In non-equilibrium, such a condition does not exist, since the steady state distribution is generically non-Hamiltonian. In our case, the proportionality between the noise and diffusion matrices (3.36) is not expected to hold, in that the diffusion and noise matrices would be renormalized differently by the drive ε . Clearly, this expansion scheme cannot explain such renormalization effects. The transverse components of those matrices on the other hand, may indeed follow (3.36), since the model is manifestly isotropic in the transverse subspace.

Nevertheless, performing the Ω -expansion for the two species model illustrates how one can get to the coarse-grained level starting from the microscopics. Furthermore, it provides us with a systematic description of the disordered phase of the model, with a reliable starting point for the fluctuations. In particular, it shows explicitly how correlations emerge between the $+$ and $-$ noises, as a result of the charge exchange mechanism. Otherwise, we could only intuitively guess it. When studying fluctuations in the disordered phase we will use eqns. (3.32-3.34) with the diffusion and noise matrices, as well as other parameters, being phenomenological constants.

Chapter 4

Structure Factors and Correlations in the Disordered Phase

Analyzing structure factors and correlations in many-particle systems is a standard way to study collective behavior in real experiments, computer simulations and theoretical frameworks. For example, for a system with short range microscopic interactions, placed in thermal equilibrium, there are no long range spatial correlations in general. Their presence is a typical signal that the system is at a critical point. On the other hand, when such systems are driven into non-equilibrium steady states, long range correlations are often observed [47]. As we already mentioned in Chapter 1.1, the standard model also exhibits long range spatial correlations *at all temperatures* above criticality [13], as a result of the breakdown of the traditional fluctuation-dissipation relations [14]. In momentum space, this appears as a discontinuity singularity of the structure factor at the origin [48].

In experiments, correlations are typically studied by electron or neutron beam scattering techniques. The scattering intensity is closely related to the structure factor. Depending on the actual physical system, this quantity is the Fourier transform of the “density-density” correlations, where, e.g., in a ferromagnetic system the “density” stands for the local magnetization. Even in the stationary case, i.e., when the averages are not expected to be time-dependent, the densities themselves are fluctuating quantities in both space and *time*. Thus, when samples are taken, it is crucial to compare the time scales of the associated fluctuations to that of the duration of a typical “snap-shot”. If the former is a lot smaller than the sampling time interval, then even one measurement practically results in a temporal average. Then the scattering intensity is a direct measure of the *average* structure factor. In the opposite scenario, however, one can store all these snap-shots which individually appear as a random pattern of speckles, but together they represent the full distribution of the fluctuating density-density products. This phenomenon has long been known in laser scattering experiments and the statistical properties of the random speckles are well

established [49]. When using Monte Carlo simulations, the ideal situation occurs: each measurement corresponds to one configuration at a certain instant of time, hence, there are no “experimental” difficulties to achieve fine sampling and one has the opportunity to study these fluctuating quantities in terms of their distribution.

Correlations in the two species model without charge exchange have already been studied [50]. In this Chapter we extend our previous work to the more general case where charge exchange is allowed [51]. In Chapter 2 we saw that the system undergoes a phase transition, controlled by particle density and drive, from a spatially homogeneous (disordered) phase to an ordered one, where particles form a single, compact strip, transverse to the field. We will investigate the correlations in the disordered phase, where we have a sound analytic understanding of the dynamics in terms of Langevin equations and will study not only the averages but the full distributions of the steady-state structure factors as well. We will primarily focus on correlations in momentum space, but using the analytic results for the structure factors, we will explicitly calculate their Fourier transform and predict the corresponding spatial correlations.

4.1 Microscopic Observables and Histograms

For simplicity, we consider $L \times L$ square lattices in two dimensions with fully periodic boundary conditions. We restrict ourselves to zero total charge again, i.e., the total number of positive and negative particles are the same:

$$\sum_{\mathbf{x}} n_{\mathbf{x}}^+ = \sum_{\mathbf{x}} n_{\mathbf{x}}^- = \bar{\rho} L^2, \quad (4.1)$$

where $\bar{\rho}$ is the average density of either species. Clearly, it is just $\bar{m}/2$ in terms of the overall mass density, defined in Chapter 2. In this Chapter we will rather use $\bar{\rho}$ as one of our control parameters, and use the term “mass” in the field theoretical sense, described later and not to be confused with the overall density of particles. Now, during one Monte Carlo step $2L^2$ nearest neighbor bonds are chosen randomly. We recall the microscopic dynamics, defined in Chapter 2.1, i.e., if a particle-hole pair is encountered, an exchange takes place with rate

$$W_{ph} = \Gamma \min\{1, \exp(qE \Delta x_{\parallel})\}, \quad (4.2)$$

where $q = \pm 1$ is the charge of the particle and Δx_{\parallel} is the change in the Δx_{\parallel} coordinate of the particle due to the jump. Similarly, if the neighboring sites occupied by opposite charges, a “charge transfer” is attempted with rate

$$W_{pp} = \gamma \Gamma \min\{1, \exp(E \Delta x_{\parallel})\}, \quad (4.3)$$

where now Δx_{\parallel} is the change in the x_{\parallel} coordinate of the *positive* particle due to the jump. Note that the notation in (4.2) and (4.3) slightly differs from that of Chapter 2: the axis parallel to the field is now denoted by x_{\parallel} .

For our simulations, we set $\Gamma = 1$. Using lattices with L ranging from 30 to 100, we initialize the system with random configurations of various particle densities and carry out runs ranging from $(2.5 \text{ to } 5) \times 10^5$ MCS. After allowing 62500 MCS for the system to settle into a steady state, we measure the Fourier transforms of $n_{\mathbf{x}}^{\pm}$ every 125 MCS, defining them now in the conventional way:

$$n_{\mathbf{k}}^{\pm} = \sum_{\mathbf{x}} e^{-i\mathbf{k}\mathbf{x}} n_{\mathbf{x}}^{\pm} . \quad (4.4)$$

In the literature, the term “structure factor” typically refers to the (ensemble- or time-) average of density-density operators in momentum space, i.e.,

$$S^{\alpha\beta}(\mathbf{k}) \equiv \frac{1}{V} \langle n_{\mathbf{k}}^{\alpha} n_{-\mathbf{k}}^{\beta} \rangle , \quad (4.5)$$

where $\alpha, \beta = +, -$; $\mathbf{k} = \frac{2\pi}{L}(m_{\perp}, m_{\parallel}) \neq \mathbf{0}$ and $V = L^2$ is the volume. The $\mathbf{k} = \mathbf{0}$ component is trivially related to the average densities by virtue of the conserved dynamics. In addition to computing averages, we construct histograms for $\frac{n_{\mathbf{k}}^{+} n_{-\mathbf{k}}^{+}}{V}$, $\frac{\text{Re}[n_{\mathbf{k}}^{+} n_{-\mathbf{k}}^{-}]}{V}$ and $\frac{\text{Im}[n_{\mathbf{k}}^{+} n_{-\mathbf{k}}^{-}]}{V}$ from their time series in the steady state. We will use the somewhat loose term “structure factors” for these fluctuating quantities themselves. By symmetry, $\frac{n_{\mathbf{k}}^{+} n_{-\mathbf{k}}^{+}}{V}$ and $\frac{n_{\mathbf{k}}^{-} n_{-\mathbf{k}}^{-}}{V}$ are distributed identically, and we consider only the former. Also note that in the disordered phase $S^{\alpha\beta}$ is the Fourier transform of the usual *equal-time* correlation function

$$G^{\alpha\beta}(\mathbf{x}) \equiv \langle n_{\mathbf{x}}^{\alpha} n_{\mathbf{0}}^{\beta} \rangle - \langle n_{\mathbf{x}}^{\alpha} \rangle \langle n_{\mathbf{0}}^{\beta} \rangle . \quad (4.6)$$

Thus, if G is even in \mathbf{x} , S will be real. Equivalently, an imaginary part of S corresponds to the part of G which is odd in \mathbf{x} . Due to charge symmetry, we expect $G^{++} = G^{--}$. Clearly, both must be even in \mathbf{x} , so that the associated S 's are real. On the other hand, due to the drive, we have

$$G^{+-}(\mathbf{x}, E) = G^{+-}(x_{\perp}, -x_{\parallel}, -E) \quad (4.7)$$

so that S^{+-} may have an imaginary part (which must be odd in E). Finally, $G^{-+}(\mathbf{x}) = G^{+-}(-\mathbf{x})$ is just a mathematical identity.

We studied systems with γ ranging from 0 to 1. For small γ 's we have to choose E and $\bar{\rho}$ in such a way that the system is in the homogeneous phase. For larger γ 's ($\gamma > \gamma_c \simeq 0.62$) the charge exchange mechanism suppresses the ordered phase entirely as we saw in Chapter 2, so we can pick arbitrarily large fields at any density. A particularly interesting case occurs for $\gamma = 1$. Since the rates W_{pp} and W_{ph} are now equal, a positive (negative) particle can no longer distinguish a negative (positive) one from a hole, and spatial inhomogeneities are impossible for either species. Thus, only the two marginal distributions, $P[\{n_{\mathbf{x}}^{+}\}]$ and

$P[\{n_{\mathbf{x}}^-\}]$, are uniform, while the full steady state distribution $P[\{n_{\mathbf{x}}^+, n_{\mathbf{x}}^-\}]$ is far from trivial and can result in, e.g., long range correlations between *different* species.

To emphasize the crucial role of the drive, we first present the steady state structure factors in *zero field* in a 100×100 system at half filling (Fig.4.1). Although here, the value of γ is irrelevant, we chose $\gamma = 0.02$. The results clearly indicate that these quantities fluctuate about a uniform finite size value. These \mathbf{k} -independent quantities simply translate to short range (δ -function) correlations in real space. In contrast, Fig. 4.2 shows the results for the three independent S 's found in the 100×100 system for non-zero drive. Here $E = 0.279$, $\bar{\rho} = 0.175$ and $\gamma = 0.02$ were chosen so that the system is in the disordered phase. The most striking feature of these objects is a discontinuity singularity at the origin. Based on similar properties of other non-equilibrium systems [15], we expect that this type of singularity results in long range spatial correlations. In Fig. 4.3, we show the same quantities for $\gamma = 1$ and draw special attention to the fact that while S^{++} does not depend on \mathbf{k} at all, S^{+-} exhibits highly nontrivial \mathbf{k} dependence. Since at this value of γ , the system cannot order at any E and $\bar{\rho}$, we have chosen *infinite* drive at half filling. Time series in the steady state, corresponding to the parameters of Fig. 4.2, are shown in Fig. 4.4 and 4.5 for the smallest longitudinal and transverse wave vectors, respectively. Fig. 4.6 and 4.7 present the associated structure factor histograms obtained from their time series.

Before discussing the data in detail, we will first present the theoretical framework within which they can be understood. In particular, we will illustrate the emergence of discontinuity singularities in the structure factors at $\mathbf{k} = \mathbf{0}$, and their consequences for long-range correlations in real space. This will then be followed by a comparison between our theoretical predictions and the simulation results.

4.2 Exact Results at Zero Field

For the special case $E = 0$, it is possible to calculate the correlations exactly. Then one can begin by comparing simulation results to these exact values. Also, as we shall see later, these zero-field values will play an important role in the structure factors at any field: they completely determine $S^{\alpha\beta}(\mathbf{k})$ when $k_{\parallel} = 0$.

At zero field the steady state probability distribution of the system is uniform. More precisely, it is

$$P[C] = \frac{1}{\mathcal{N}}, \quad (4.8)$$

where $C = \{n_{\mathbf{x}}^+, n_{\mathbf{x}}^-\}$ is a configuration and \mathcal{N} is the total number of configurations. By

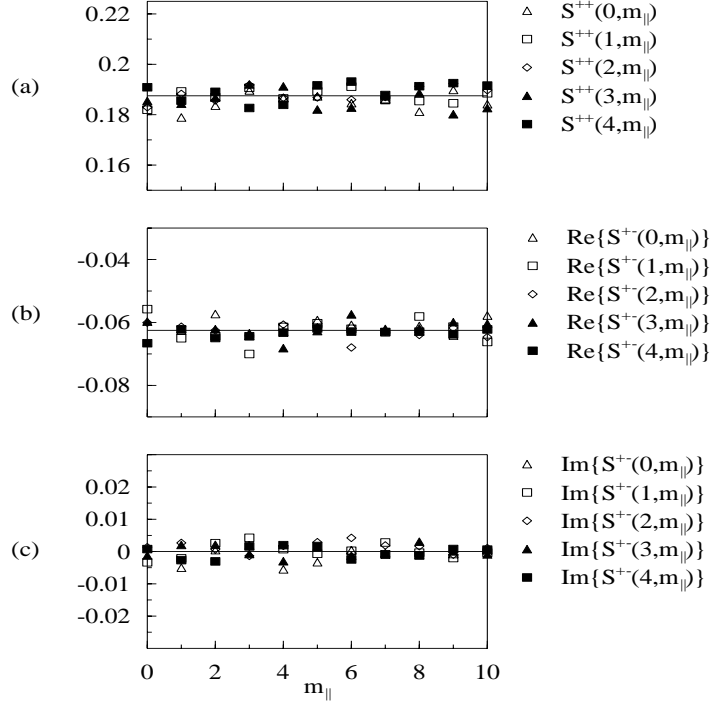


Figure 4.1: Steady state structure factors in the absence of the drive (a) $S^{++}(\mathbf{k})$, (b) $\text{Re}\{S^{+-}(\mathbf{k})\}$, (c) $\text{Im}\{S^{+-}(\mathbf{k})\}$ for an $L = 100$ system at $\gamma = 0.02$, $E = 0.00$ and $\bar{\rho} = 0.25$. Structure factors are plotted against the integer $m_{\parallel} = \frac{k_{\parallel}L}{2\pi}$, while $m_{\perp} = \frac{k_{\perp}L}{2\pi}$ is taken as a parameter. Lines are representing the exact finite size values which are the same for all $\mathbf{k} \neq \mathbf{0}$.

simple combinatorics, it is

$$\mathcal{N} = \frac{N!}{N^{+!}N^{-!}(N - N^{+} - N^{-})!}, \quad (4.9)$$

where N is the total number of lattice sites (i.e., the volume V if the lattice constant is unity) and $N^{\pm} = \sum_{\mathbf{x}} n_{\mathbf{x}}^{\pm}$ is the total number of \pm particles. To obtain the structure factors, we will need the first and second moments of the occupation numbers. These are also easy to find, e.g.

$$\langle n_{\mathbf{x}}^{+} \rangle = \sum_C P[C] n_{\mathbf{x}}^{+} = \frac{1}{\mathcal{N}} \sum_C n_{\mathbf{x}}^{+} = \frac{1}{\mathcal{N}} \frac{(N-1)!}{(N^{+}-1)!N^{-!}(N - N^{+} - N^{-})!} = \frac{N^{+}}{N}, \quad (4.10)$$

and similarly $\langle n_{\mathbf{x}}^{-} \rangle = N^{-}/N$. Before finding the second moments it is useful to note that

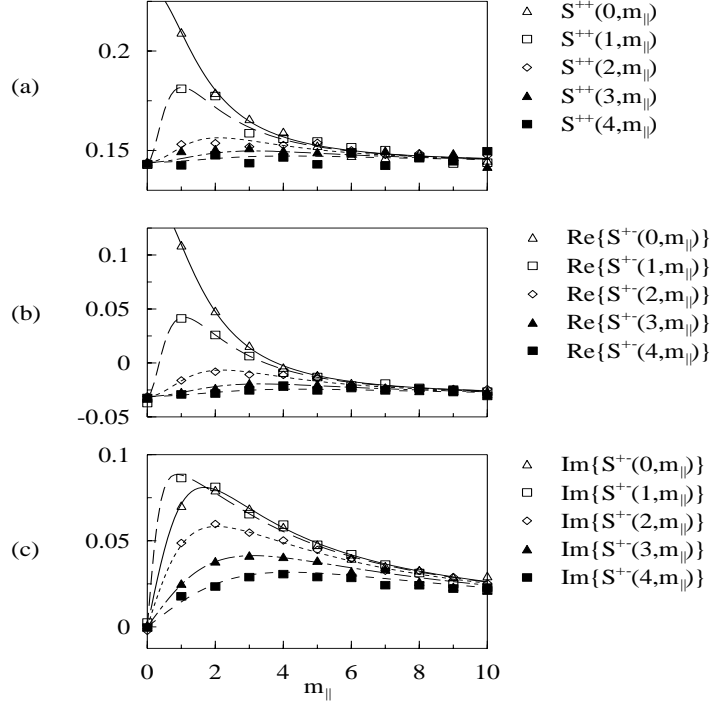


Figure 4.2: Steady state structure factors (a) $S^{++}(\mathbf{k})$, (b) $\text{Re}\{S^{+-}(\mathbf{k})\}$, (c) $\text{Im}\{S^{+-}(\mathbf{k})\}$ for an $L = 100$ system at $\gamma = 0.02$, $E = 0.279$ and $\bar{\rho} = 0.175$. Structure factors are plotted against the integer $m_{\parallel} = \frac{k_{\parallel}L}{2\pi}$, while $m_{\perp} = \frac{k_{\perp}L}{2\pi}$ is taken as a parameter. Lines are representing the fitted theoretical curves.

$n_{\mathbf{x}}^{\pm 2} = n_{\mathbf{x}}^{\pm}$ and $n_{\mathbf{x}}^{+}n_{\mathbf{x}}^{-} = 0$ identically, by virtue of the excluded volume constraint. Thus,

$$\langle n_{\mathbf{x}}^{+}n_{\mathbf{x}'}^{+} \rangle = \frac{1}{\mathcal{N}} \sum_{\mathcal{C}} n_{\mathbf{x}}^{+}n_{\mathbf{x}'}^{+} = \begin{cases} \frac{1}{\mathcal{N}} \sum_{\mathcal{C}} n_{\mathbf{x}}^{+} & = \frac{N^{+}}{N} & \text{if } \mathbf{x} = \mathbf{x}' \\ \frac{1}{\mathcal{N}} \frac{(N-2)!}{(N^{+}-2)!(N^{-})!} & = \frac{N^{+}(N^{+}-1)}{N(N-1)} & \text{if } \mathbf{x} \neq \mathbf{x}' \end{cases} \quad (4.11)$$

and

$$\langle n_{\mathbf{x}}^{+}n_{\mathbf{x}'}^{-} \rangle = \frac{1}{\mathcal{N}} \sum_{\mathcal{C}} n_{\mathbf{x}}^{+}n_{\mathbf{x}'}^{-} = \begin{cases} \frac{1}{\mathcal{N}} \sum_{\mathcal{C}} 0 & = 0 & \text{if } \mathbf{x} = \mathbf{x}' \\ \frac{1}{\mathcal{N}} \frac{(N-2)!}{(N^{+}-1)!(N^{-}-1)!} & = \frac{N^{+}N^{-}}{N(N-1)} & \text{if } \mathbf{x} \neq \mathbf{x}' \end{cases} \quad (4.12)$$

Using the definition (4.5) we find

$$S^{++}(\mathbf{k}) = \frac{1}{N} \left\langle \sum_{\mathbf{x}} e^{-i\mathbf{k}\mathbf{x}} n_{\mathbf{x}}^{+} \sum_{\mathbf{x}'} e^{i\mathbf{k}\mathbf{x}'} n_{\mathbf{x}'}^{+} \right\rangle = \frac{1}{N} \sum_{\mathbf{x}, \mathbf{x}'} e^{-i\mathbf{k}(\mathbf{x}-\mathbf{x}')} \langle n_{\mathbf{x}}^{+}n_{\mathbf{x}'}^{+} \rangle = \quad (4.13)$$

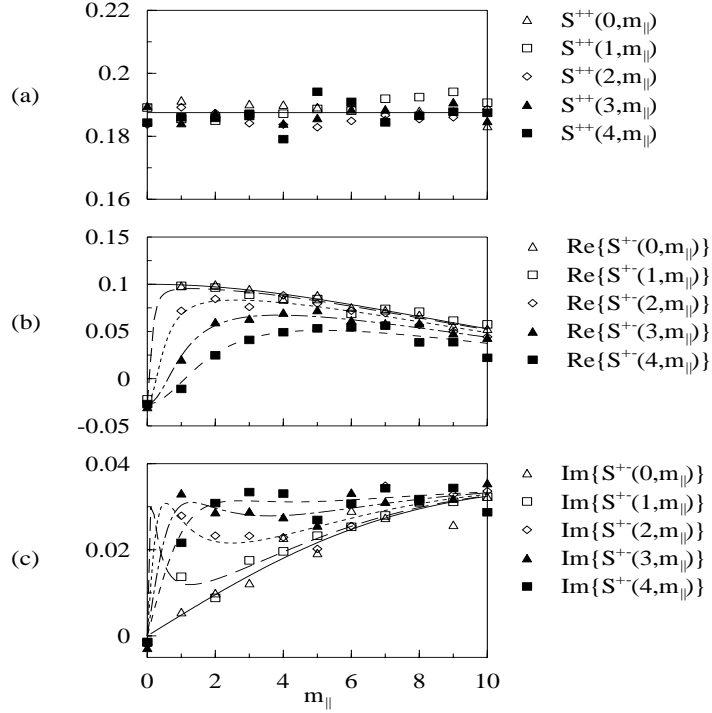


Figure 4.3: Steady state structure factors (a) $S^{++}(\mathbf{k})$, (b) $\text{Re}\{S^{+-}(\mathbf{k})\}$, (c) $\text{Im}\{S^{+-}(\mathbf{k})\}$ for an $L = 100$ system at $\gamma = 1.00$, $E = \infty$ and $\bar{\rho} = 0.25$. Structure factors are plotted against the integer $m_{\parallel} = \frac{k_{\parallel}L}{2\pi}$, while $m_{\perp} = \frac{k_{\perp}L}{2\pi}$ is taken as a parameter. Lines are representing the fitted theoretical curves.

$$\begin{aligned} & \frac{1}{N} \left\{ N \langle n_{\mathbf{x}}^{+2} \rangle + \sum_{\mathbf{x} \neq \mathbf{x}'} e^{-i\mathbf{k}(\mathbf{x}-\mathbf{x}')} \langle n_{\mathbf{x}}^{+} n_{\mathbf{x}'}^{+} \rangle \right\} = \frac{N^{+}}{N} + (N\delta_{\mathbf{k}\mathbf{0}} - 1) \frac{N^{+}(N^{+} - 1)}{N(N - 1)} = \\ & = \begin{cases} \rho^{\bar{+}2} N & \text{if } \mathbf{k} = \mathbf{0} \\ \rho^{\bar{+}}(1 - \rho^{\bar{+}}) \frac{N}{N-1} & \text{if } \mathbf{k} \neq \mathbf{0} \end{cases} \end{aligned}$$

and

$$\begin{aligned} S^{+-}(\mathbf{k}) &= \\ & \frac{1}{N} \left\langle \sum_{\mathbf{x}} e^{-i\mathbf{k}\mathbf{x}} n_{\mathbf{x}}^{+} \sum_{\mathbf{x}'} e^{i\mathbf{k}\mathbf{x}'} n_{\mathbf{x}'}^{-} \right\rangle = \frac{1}{N} \sum_{\mathbf{x}, \mathbf{x}'} e^{-i\mathbf{k}(\mathbf{x}-\mathbf{x}')} \langle n_{\mathbf{x}}^{+} n_{\mathbf{x}'}^{-} \rangle = \quad (4.14) \\ & \frac{1}{N} \sum_{\mathbf{x} \neq \mathbf{x}'} e^{-i\mathbf{k}(\mathbf{x}-\mathbf{x}')} \langle n_{\mathbf{x}}^{+} n_{\mathbf{x}'}^{-} \rangle = (N\delta_{\mathbf{k}\mathbf{0}} - 1) \frac{N^{+}N^{-}}{N(N - 1)} = \\ & = \begin{cases} \rho^{\bar{+}}\rho^{\bar{-}} N & \text{if } \mathbf{k} = \mathbf{0} \\ -\rho^{\bar{+}}\rho^{\bar{-}} \frac{N}{N-1} & \text{if } \mathbf{k} \neq \mathbf{0} \end{cases} , \end{aligned}$$

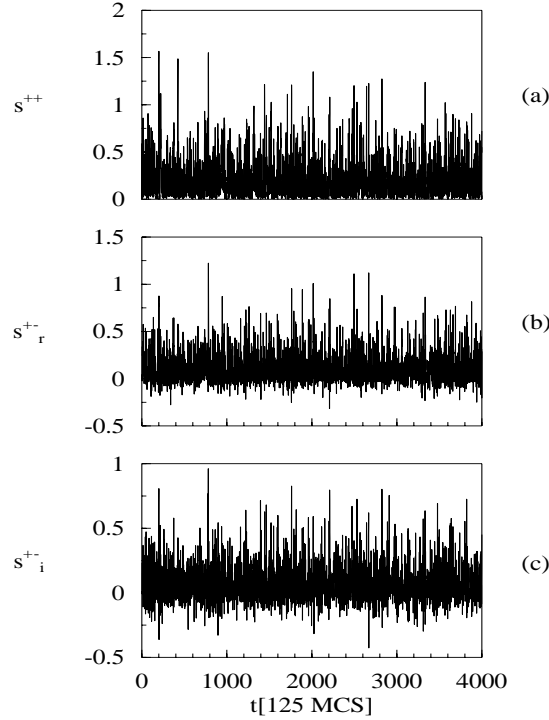


Figure 4.4: Time series of the $\mathbf{k} = \frac{2\pi}{L}(0, 1)$ structure factors (a) $s^{++} = \frac{n_{\mathbf{k}}^+ n_{-\mathbf{k}}^+}{V}$, (b) $s_r^{+-} = \frac{\text{Re}[n_{\mathbf{k}}^+ n_{-\mathbf{k}}^-]}{V}$ and (c) $s_i^{+-} = \frac{\text{Im}[n_{\mathbf{k}}^+ n_{-\mathbf{k}}^-]}{V}$. $L = 100$, $\gamma = 0.02$, $E = 0.279$ and $\bar{\rho} = 0.175$.

where in (4.13) and (4.14) we used $\bar{\rho}^\pm \equiv N^\pm/N$ for the average densities. As we already noted, the $\mathbf{k} = \mathbf{0}$ components of $S^{\alpha\beta}$ are trivially related to the average densities, reflecting the conserved dynamics. Focusing on the $\mathbf{k} \neq \mathbf{0}$ fluctuating modes, and keeping in mind that $\bar{\rho}^+ = \bar{\rho}^- = \bar{\rho}$ for our simulation, we clearly have

$$\begin{aligned}
 S^{++}(\mathbf{k}) &= \bar{\rho}(1 - \bar{\rho}) \frac{N}{N - 1} = \bar{\rho}(1 - \bar{\rho}) \left(1 + \mathcal{O}\left(\frac{1}{N}\right) \right) \\
 S^{+-}(\mathbf{k}) &= -\bar{\rho}^2 \frac{N}{N - 1} = -\bar{\rho}^2 \left(1 + \mathcal{O}\left(\frac{1}{N}\right) \right).
 \end{aligned}
 \tag{4.15}$$

By symmetry, $S^{--}(\mathbf{k}) = S^{++}(\mathbf{k})$, and $S^{-+}(\mathbf{k}) = S^{+-}(\mathbf{k})$, since it is real now. It is also apparent that the value of γ is irrelevant in the $E = 0$ “completely” disordered case. Simulation results together with the above exact amplitudes are shown in Fig. 4.1.

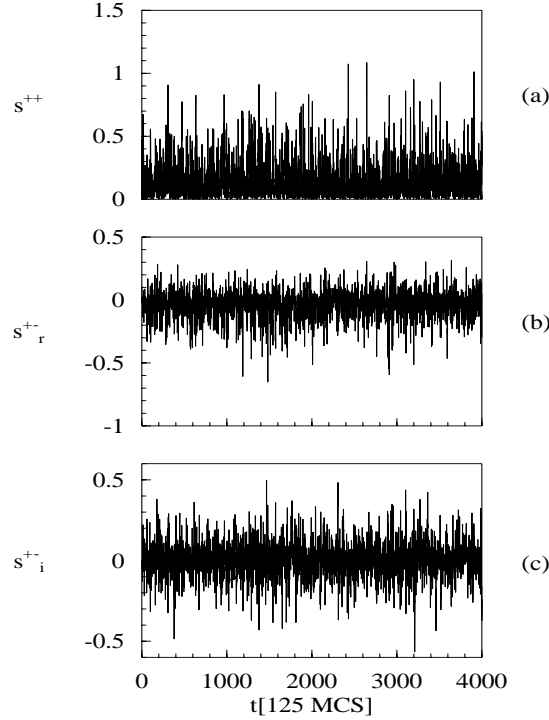


Figure 4.5: Time series of the $\mathbf{k} = \frac{2\pi}{L}(1, 0)$ structure factors for (a) $s^{++} = \frac{n_{\mathbf{k}}^+ n_{-\mathbf{k}}^+}{V}$, (b) $s_r^{+-} = \frac{\text{Re}[n_{\mathbf{k}}^+ n_{-\mathbf{k}}^-]}{V}$ and (c) $s_i^{+-} = \frac{\text{Im}[n_{\mathbf{k}}^+ n_{-\mathbf{k}}^-]}{V}$. $L = 100$, $\gamma = 0.02$, $E = 0.279$ and $\bar{\rho} = 0.175$.

4.3 Coarse-grained Description

Since our interest lies in the behavior at large distances (or small \mathbf{k}), the simplest approach relies on continuum field theory. Starting from the dynamics at the microscopic level, specified by (4.2,4.3) and the associated master equation, there are several ways to arrive at a coarse-grained description. A systematic one is to perform an Ω -expansion [44], as we described in detail in Chapter 3. Now we recapitulate the results for the equivalent set of Langevin equations. The fast degrees of freedom are the density fluctuations, $\{\chi^\alpha(\mathbf{x}, t)\}$, about the time independent, homogeneous densities, $\rho^\pm(\mathbf{x}, t) = \bar{\rho}$. For generality, we consider the d-dimensional case when \mathbf{x}_\parallel is directed along the electric field and \mathbf{x}_\perp is in the d-1 dimensional subspace, perpendicular to the field. In the continuum limit, the Langevin equation for density fluctuations is:

$$\partial_t \chi^\alpha(\mathbf{x}, t) = \mathcal{L}^{\alpha\beta}(\nabla) \chi^\beta(\mathbf{x}, t) - \nabla \eta^\alpha(\mathbf{x}, t), \quad (4.16)$$

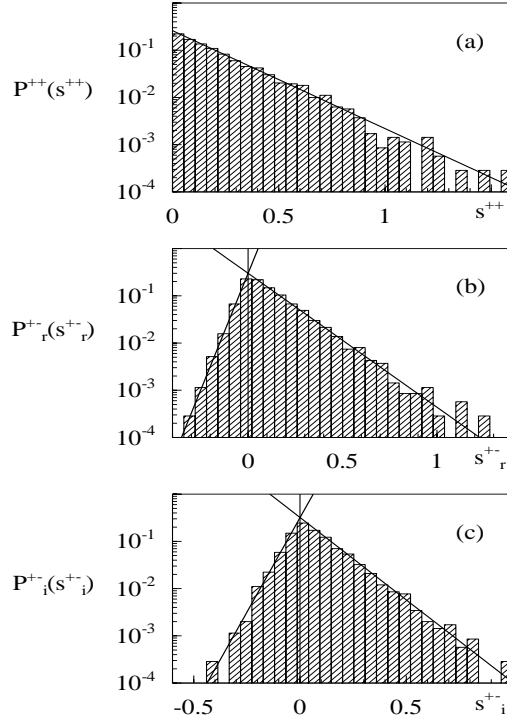


Figure 4.6: Histograms representing the distributions of the $\mathbf{k} = \frac{2\pi}{L}(0, 1)$ structure factors for (a) $s^{++} = \frac{n_{\mathbf{k}}^+ n_{-\mathbf{k}}^+}{V}$, (b) $s_r^{+-} = \frac{\text{Re}[n_{\mathbf{k}}^+ n_{-\mathbf{k}}^-]}{V}$ and (c) $s_i^{+-} = \frac{\text{Im}[n_{\mathbf{k}}^+ n_{-\mathbf{k}}^-]}{V}$. $L = 100$, $\gamma = 0.02$, $E = 0.279$ and $\bar{\rho} = 0.175$. Theoretical distributions (a) $P^{++}(s^{++}; \mathbf{k})$, (b) $P_r^{+-}(s_r^{+-}; \mathbf{k})$ and (c) $P_i^{+-}(s_i^{+-}; \mathbf{k})$ are plotted with solid lines on the same graphs.

where

$$(\mathcal{L}^{\alpha\beta}(\nabla)) = \begin{pmatrix} (1 - \tilde{\rho})\nabla\Gamma\nabla - (1 - \delta\tilde{\rho})\varepsilon\Gamma_{\parallel}\partial_{\parallel} & \tilde{\rho}\nabla\Gamma\nabla + \tilde{\rho}\varepsilon\Gamma_{\parallel}\partial_{\parallel} \\ \tilde{\rho}\nabla\Gamma\nabla - \tilde{\rho}\varepsilon\Gamma_{\parallel}\partial_{\parallel} & (1 - \tilde{\rho})\nabla\Gamma\nabla + (1 - \delta\tilde{\rho})\varepsilon\Gamma_{\parallel}\partial_{\parallel} \end{pmatrix} \quad (4.17)$$

and we defined the “reduced” average density $\tilde{\rho} \equiv (1 - \gamma)\bar{\rho}$ and $\delta \equiv (3 - \gamma)/(1 - \gamma)$. Also,

$$\Gamma = \begin{pmatrix} \Gamma_{\perp} & \mathbf{0} \\ \mathbf{0} & \Gamma_{\parallel} \end{pmatrix} \quad (4.18)$$

is the diffusion-matrix. Γ_{\perp} is diagonal and isotropic in the $d-1$ dimensional subspace, thus characterized by a number Γ_{\perp} . ε is the coarse-grained bias and $\hat{\mathbf{x}}_{\parallel}$ is the unit vector along the x_{\parallel} direction. $\boldsymbol{\eta}^{\pm}(\mathbf{x}, t)$ are Gaussian, white noise terms, satisfying:

$$\langle \eta_i^{\alpha}(\mathbf{x}, t) \rangle = 0, \quad \langle \eta_i^{\alpha}(\mathbf{x}, t) \eta_j^{\beta}(\mathbf{x}', t') \rangle = 2\sigma_{ij}^{\alpha\beta} \delta(\mathbf{x} - \mathbf{x}') \delta(t - t'), \quad (4.19)$$

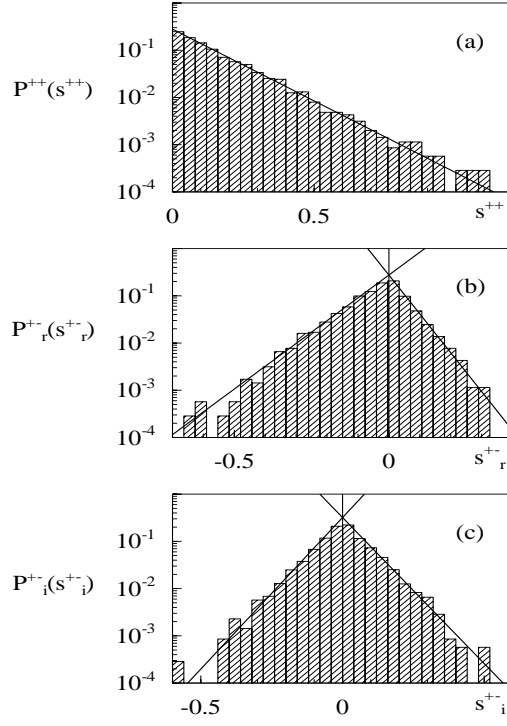


Figure 4.7: Histograms representing the distributions of the $\mathbf{k} = \frac{2\pi}{L}(1,0)$ structure factors for (a) $s^{++} = \frac{n_{\mathbf{k}}^+ n_{-\mathbf{k}}^+}{V}$, (b) $s_r^{+-} = \frac{\text{Re}[n_{\mathbf{k}}^+ n_{-\mathbf{k}}^-]}{V}$ and (c) $s_i^{+-} = \frac{\text{Im}[n_{\mathbf{k}}^+ n_{-\mathbf{k}}^-]}{V}$. $L = 100$, $\gamma = 0.02$, $E = 0.279$ and $\bar{\rho} = 0.175$. Theoretical distributions (a) $P^{++}(s^{++}; \mathbf{k})$, (b) $P_r^{+-}(s_r^{+-}; \mathbf{k})$ and (c) $P_i^{+-}(s_i^{+-}; \mathbf{k})$ are plotted with solid lines on the same graphs.

where $\alpha, \beta = +, -$; $i, j = 1, 2, \dots, d$ and $(\sigma_{ij})^{\alpha\beta} = \sigma^{\alpha\beta}$ are the noise matrices which are diagonal but not proportional to the unit matrix, due to the bias:

$$\sigma^{\alpha\beta} = \begin{pmatrix} \sigma_{\perp}^{\alpha\beta} & \mathbf{0} \\ \mathbf{0} & \sigma_{\parallel}^{\alpha\beta} \end{pmatrix}. \quad (4.20)$$

Note that $\sigma^{\alpha\beta}$ is symmetric and due to charge symmetry, we also have $\sigma^{++} = \sigma^{--}$. Similar to Γ_{\perp} , $\sigma_{\perp}^{\alpha\beta}$ is diagonal and isotropic in the $d-1$ dimensional subspace, characterized by a number $\sigma_{\perp}^{\alpha\beta}$. As an explicit result of the Ω -expansion, we found (3.36)

$$\begin{aligned} \sigma^{++} &= [\bar{\rho}(1 - 2\bar{\rho}) + \gamma\bar{\rho}^2] \mathbf{\Gamma} \\ \sigma^{+-} &= [-\gamma\bar{\rho}^2] \mathbf{\Gamma} \end{aligned}, \quad (4.21)$$

i.e., $\sigma^{\alpha\beta} \propto \mathbf{\Gamma}$. However, when driven, the proportionality is not expected to hold, in that the diffusion and noise matrices would be renormalized differently by the drive ε .

This is certainly the situation in the driven single species case [11]. Unfortunately, the Ω -expansion cannot explain such coarse-graining effects which are typically generated by the highly anisotropic nonlinear terms neglected in the drift coefficient. Thus, we can only accept (4.21) in the absence of the drive where the system is in equilibrium and then it reflects FDT. Finally, we point out that there is a correlation between $\boldsymbol{\eta}^+$ and $\boldsymbol{\eta}^-$ due to the fact that charge exchange is allowed, and this effect and the corresponding matrix is expected to be proportional to γ and negative definite for non-zero drive as well.

4.3.1 Steady-state structure factors

To find the correlations and structure factors from eqns. (4.16-4.19), we introduce the Fourier components for the fluctuations:

$$\chi^\pm(\mathbf{k}, \omega) = \int dt d^d x \chi^\pm(\mathbf{x}, t) e^{-i(\omega t + \mathbf{kx})}, \quad (4.22)$$

and similar ones for the noise, so that

$$\langle \eta_i^\alpha(\mathbf{k}, \omega) \rangle = 0, \quad \langle \eta_i^\alpha(\mathbf{k}, \omega) \eta_j^\beta(\mathbf{k}', \omega') \rangle = 2\sigma_{ij}^{\alpha\beta} \left[(2\pi)^{d+1} \delta(\mathbf{k} + \mathbf{k}') \delta(\omega + \omega') \right]. \quad (4.23)$$

Then the solution to (4.16) is trivial:

$$\chi^\alpha(\mathbf{k}, \omega) = (L^{-1})^{\alpha\beta} i\mathbf{k}\boldsymbol{\eta}^\beta(\mathbf{k}, \omega), \quad (4.24)$$

where

$$L^{\alpha\beta}(\mathbf{k}, \omega) \equiv \mathcal{L}^{\alpha\beta}(i\mathbf{k}) - i\omega\delta^{\alpha\beta}. \quad (4.25)$$

Note that, in \mathbf{k} space, $(\mathcal{L}^{++}, \mathcal{L}^{--})$ and $(\mathcal{L}^{+-}, \mathcal{L}^{-+})$ are complex conjugate pairs.

As expected, $\langle \chi^\pm(\mathbf{k}, \omega) \rangle = 0$, since these are the fluctuations about the conserved average densities. Their correlations are just the *dynamic* structure factors, easily obtained from (4.23) and (4.24). From the definition:

$$S^{\alpha\beta}(\mathbf{k}, \omega) \left[(2\pi)^{d+1} \delta(\mathbf{k} + \mathbf{k}') \delta(\omega + \omega') \right] \equiv \langle \chi^\alpha(\mathbf{k}, \omega) \chi^\beta(\mathbf{k}', \omega') \rangle, \quad (4.26)$$

we find the two independent S 's:

$$\begin{aligned} S^{++}(\mathbf{k}, \omega) &= \frac{2\mathbf{k}\boldsymbol{\sigma}^{++}\mathbf{k}}{|\det(L)|^2} \left(|L^{--}|^2 + |L^{+-}|^2 \right) - \frac{2\mathbf{k}\boldsymbol{\sigma}^{+-}\mathbf{k}}{|\det(L)|^2} 2\text{Re}\{L^{--}L^{-+}\} \\ S^{+-}(\mathbf{k}, \omega) &= -\frac{2\mathbf{k}\boldsymbol{\sigma}^{++}\mathbf{k}}{|\det(L)|^2} L^{+-} \left((L^{++})^* + L^{--} \right) + \frac{2\mathbf{k}\boldsymbol{\sigma}^{+-}\mathbf{k}}{|\det(L)|^2} \left((L^{++})^* L^{--} + (L^{+-})^2 \right). \end{aligned} \quad (4.27)$$

To compare directly with simulations, we define the steady-state structure factors:

$$S^{\alpha\beta}(\mathbf{k}) \left[(2\pi)^d \delta(\mathbf{k} + \mathbf{k}') \right] \equiv \langle \chi^\alpha(\mathbf{k}, t) \chi^\beta(\mathbf{k}', t) \rangle. \quad (4.28)$$

They are easily obtained from (4.27) by an integration over ω , using the residue theorem and noting that the two zeros of $\det(L)$ simply correspond to the two stable eigenvalues of \mathcal{L} :

$$\omega_{1,2} = -i \frac{\text{Tr}(\mathcal{L})}{2} \pm \sqrt{\det(\mathcal{L}) - \left(\frac{\text{Tr}(\mathcal{L})}{2}\right)^2}. \quad (4.29)$$

Note that $-\frac{1}{2}\text{Tr}(\mathcal{L}) = (1 - \tilde{\rho})\mathbf{k}\Gamma\mathbf{k}$ is positive definite, while we need to require $\det(\mathcal{L}) > 0$ for all $\mathbf{k} \neq 0$ to assure that the system is within the linear stability boundary. Then the results are:

$$\begin{aligned} S^{++}(\mathbf{k}) &= \frac{\mathbf{k}\boldsymbol{\sigma}^{++}\mathbf{k}}{-\frac{1}{2}\text{Tr}(\mathcal{L})} \frac{|\mathcal{L}^{--}|^2}{\det(\mathcal{L})} - \frac{\mathbf{k}\boldsymbol{\sigma}^{+-}\mathbf{k}}{-\frac{1}{2}\text{Tr}(\mathcal{L})} \frac{\text{Re}\{\mathcal{L}^{--}\mathcal{L}^{+-}\}}{\det(\mathcal{L})} \\ S^{+-}(\mathbf{k}) &= -\frac{\mathbf{k}\boldsymbol{\sigma}^{++}\mathbf{k}}{-\frac{1}{2}\text{Tr}(\mathcal{L})} \frac{\mathcal{L}^{--}\mathcal{L}^{+-}}{\det(\mathcal{L})} + \frac{\mathbf{k}\boldsymbol{\sigma}^{+-}\mathbf{k}}{-\frac{1}{2}\text{Tr}(\mathcal{L})} \frac{\mathcal{L}^{--}\text{Re}\{\mathcal{L}^{--}\} + i\mathcal{L}^{+-}\text{Im}\{\mathcal{L}^{+-}\}}{\det(\mathcal{L})}. \end{aligned} \quad (4.30)$$

Finally, using (4.17), eqs. (4.30) take the explicit form:

$$\begin{aligned} S^{++}(\mathbf{k}) &= \frac{(1 - \tilde{\rho})}{(1 - 2\tilde{\rho})} \frac{\mathbf{k}\boldsymbol{\sigma}^{++}\mathbf{k}}{\mathbf{k}\Gamma\mathbf{k}} \frac{(\mathbf{k}\Gamma\mathbf{k})^2 + \frac{(1-\delta\tilde{\rho})^2}{(1-\tilde{\rho})^2} \varepsilon^2 \Gamma_{\parallel}^2 k_{\parallel}^2}{(\mathbf{k}\Gamma\mathbf{k})^2 + 4m^2 \Gamma_{\parallel} k_{\parallel}^2} \\ &\quad - \frac{\tilde{\rho}}{(1 - 2\tilde{\rho})} \frac{\mathbf{k}\boldsymbol{\sigma}^{+-}\mathbf{k}}{\mathbf{k}\Gamma\mathbf{k}} \frac{(\mathbf{k}\Gamma\mathbf{k})^2 + \frac{(1-\delta\tilde{\rho})}{(1-\tilde{\rho})} \varepsilon^2 \Gamma_{\parallel}^2 k_{\parallel}^2}{(\mathbf{k}\Gamma\mathbf{k})^2 + 4m^2 \Gamma_{\parallel} k_{\parallel}^2} \\ \text{Re}\{S^{+-}(\mathbf{k})\} &= -\frac{\tilde{\rho}}{(1 - 2\tilde{\rho})} \frac{\mathbf{k}\boldsymbol{\sigma}^{++}\mathbf{k}}{\mathbf{k}\Gamma\mathbf{k}} \frac{(\mathbf{k}\Gamma\mathbf{k})^2 - \frac{(1-\delta\tilde{\rho})}{(1-\tilde{\rho})} \varepsilon^2 \Gamma_{\parallel}^2 k_{\parallel}^2}{(\mathbf{k}\Gamma\mathbf{k})^2 + 4m^2 \Gamma_{\parallel} k_{\parallel}^2} \\ &\quad + \frac{(1 - \tilde{\rho})}{(1 - 2\tilde{\rho})} \frac{\mathbf{k}\boldsymbol{\sigma}^{+-}\mathbf{k}}{\mathbf{k}\Gamma\mathbf{k}} \frac{(\mathbf{k}\Gamma\mathbf{k})^2 - \frac{\tilde{\rho}^2}{(1-\tilde{\rho})^2} \varepsilon^2 \Gamma_{\parallel}^2 k_{\parallel}^2}{(\mathbf{k}\Gamma\mathbf{k})^2 + 4m^2 \Gamma_{\parallel} k_{\parallel}^2} \\ \text{Im}\{S^{+-}(\mathbf{k})\} &= \frac{\tilde{\rho}(2 - (1 + \delta)\tilde{\rho})}{(1 - \tilde{\rho})(1 - 2\tilde{\rho})} \frac{(\mathbf{k}\boldsymbol{\sigma}^{++}\mathbf{k}) \varepsilon \Gamma_{\parallel} k_{\parallel}}{(\mathbf{k}\Gamma\mathbf{k})^2 + 4m^2 \Gamma_{\parallel} k_{\parallel}^2} \\ &\quad - \frac{(1 - \tilde{\rho})(1 - \delta\tilde{\rho}) + \tilde{\rho}^2}{(1 - \tilde{\rho})(1 - 2\tilde{\rho})} \frac{(\mathbf{k}\boldsymbol{\sigma}^{+-}\mathbf{k}) \varepsilon \Gamma_{\parallel} k_{\parallel}}{(\mathbf{k}\Gamma\mathbf{k})^2 + 4m^2 \Gamma_{\parallel} k_{\parallel}^2}, \end{aligned} \quad (4.31)$$

where

$$4m^2 \equiv \frac{(1 - \delta\tilde{\rho})^2 - \tilde{\rho}^2}{1 - 2\tilde{\rho}} \varepsilon^2 \Gamma_{\parallel} = \frac{(1 - 2\tilde{\rho})(1 - (2 - \gamma)2\tilde{\rho})}{(1 - (1 - \gamma)2\tilde{\rho})} \varepsilon^2 \Gamma_{\parallel} \quad (4.32)$$

is the definition of the ‘‘mass’’ m . To keep the system in the homogeneous phase, it is sufficient to impose $m^2 > 0$, i.e., $\tilde{\rho} < \frac{1}{2(2-\gamma)}$. We should note that, in the limit $\varepsilon L \rightarrow \infty$, the mean-field phase boundary is given precisely by $m^2 = 0$. Otherwise, for *finite* εL , the

system does not reach the stability limit as long as

$$\left(\frac{\varepsilon L}{2\pi}\right)^2 < \frac{1 - (1 - \gamma)2\bar{\rho}}{(1 - 2\bar{\rho})(2 - \gamma)2\bar{\rho} - 1} \quad (4.33)$$

is satisfied, which is just the mean-field stability limit, already found in Chapter 2, eqn. (2.47).

A key feature of these structure factors is that, unlike in equilibrium cases, all are singular at the origin. For both S^{++} and $\text{Re}\{S^{+-}\}$, this singularity is exhibited as a discontinuity, i.e., $\lim_{k_{\parallel} \rightarrow 0} S(\mathbf{0}, k_{\parallel}) \neq \lim_{\mathbf{k}_{\perp} \rightarrow \mathbf{0}} S(\mathbf{k}_{\perp}, 0)$. In particular,

$$\frac{\lim_{k_{\parallel} \rightarrow 0} S^{++}(\mathbf{0}, k_{\parallel})}{\lim_{\mathbf{k}_{\perp} \rightarrow \mathbf{0}} S^{++}(\mathbf{k}_{\perp}, 0)} = \frac{1 - 2\tilde{\rho}}{(1 - \delta\tilde{\rho})^2 - \tilde{\rho}^2} \frac{(1 - \delta\tilde{\rho})^2}{(1 - \tilde{\rho})^2} \frac{\frac{\sigma_{\parallel}^{++}}{\Gamma_{\parallel}} - \frac{\tilde{\rho}}{1 - \delta\tilde{\rho}} \frac{\sigma_{\parallel}^{+-}}{\Gamma_{\parallel}}}{\frac{\sigma_{\perp}^{++}}{\Gamma_{\perp}} - \frac{\tilde{\rho}}{1 - \tilde{\rho}} \frac{\sigma_{\perp}^{+-}}{\Gamma_{\perp}}} \quad (4.34)$$

and

$$\frac{\lim_{k_{\parallel} \rightarrow 0} \text{Re}\{S^{+-}(\mathbf{0}, k_{\parallel})\}}{\lim_{\mathbf{k}_{\perp} \rightarrow \mathbf{0}} \text{Re}\{S^{+-}(\mathbf{k}_{\perp}, 0)\}} = -\frac{1 - 2\tilde{\rho}}{(1 - \delta\tilde{\rho})^2 - \tilde{\rho}^2} \frac{1 - \delta\tilde{\rho}}{1 - \tilde{\rho}} \frac{\frac{\sigma_{\parallel}^{+-}}{\Gamma_{\parallel}} - \frac{\tilde{\rho}}{1 - \delta\tilde{\rho}} \frac{\sigma_{\parallel}^{++}}{\Gamma_{\parallel}}}{\frac{\sigma_{\perp}^{+-}}{\Gamma_{\perp}} - \frac{1 - \tilde{\rho}}{\tilde{\rho}} \frac{\sigma_{\perp}^{++}}{\Gamma_{\perp}}}. \quad (4.35)$$

In general these ratios are not unity. Note that these singularities come not only from the generic FDT-breaking property, namely $\frac{\sigma_{\parallel}^{\alpha\beta}}{\Gamma_{\parallel}} \neq \frac{\sigma_{\perp}^{\alpha\beta}}{\Gamma_{\perp}}$, but also from the specifics of this particular driven system. The first factor in eqs. (4.34,4.35) is a monotonically increasing function of $\bar{\rho}$, reaching ∞ at $\bar{\rho} = \frac{1}{2(2-\gamma)}$. This divergence is related to the instability of the homogeneous phase, as we saw above. On the other hand, though $\text{Im}\{S^{+-}(\mathbf{k})\}$ vanishes for $\mathbf{k} \rightarrow \mathbf{0}$ in any direction, discontinuities are present in higher derivatives.

At the end of this Chapter we will compare these results with the structure factors obtained from simulations.

4.3.2 Equal-time spatial correlations

In configuration space, the above singularities translate into power law decays of the equal-time correlation functions $\langle \chi^{\alpha}(\mathbf{x}' + \mathbf{x}, t) \chi^{\beta}(\mathbf{x}', t) \rangle$, which are, thanks to translational invariance, independent of \mathbf{x}' . More precisely, we just have

$$G^{\alpha\beta}(\mathbf{x}) = \int \frac{d^d k}{(2\pi)^d} S^{\alpha\beta}(\mathbf{k}) e^{i\mathbf{k}\mathbf{x}}. \quad (4.36)$$

To carry out the transform, it is convenient to rescale the lengths and momenta

$$\mathbf{x}_{\perp} \rightarrow \frac{\mathbf{x}_{\perp}}{\Gamma_{\perp}^{\frac{1}{2}}}, \quad x_{\parallel} \rightarrow \frac{x_{\parallel}}{\Gamma_{\parallel}^{\frac{1}{2}}}; \quad \mathbf{k}_{\perp} \rightarrow \Gamma_{\perp}^{\frac{1}{2}} \mathbf{k}_{\perp}, \quad k_{\parallel} \rightarrow \Gamma_{\parallel}^{\frac{1}{2}} k_{\parallel} \quad (4.37)$$

so that Γ becomes the unit matrix. In terms of these rescaled \mathbf{x} , let us define $r \equiv |\mathbf{x}|$, $r_{\perp} \equiv |\mathbf{x}_{\perp}|$ and $r_{\parallel} \equiv |x_{\parallel}|$. Also, we should rescale the elements of the noise matrix, to keep the notation simple:

$$\sigma_{\perp}^{\alpha\beta} \rightarrow \frac{\sigma_{\perp}^{\alpha\beta}}{\Gamma_{\perp}}, \quad \sigma_{\parallel}^{\alpha\beta} \rightarrow \frac{\sigma_{\parallel}^{\alpha\beta}}{\Gamma_{\parallel}}. \quad (4.38)$$

After some algebra the structure factors can be written in a compact form:

$$\begin{aligned} S^{++}(\mathbf{k}) &= \frac{\mathbf{k}\sigma^1\mathbf{k}}{k^2} - (\mathbf{k}\sigma^2\mathbf{k})\frac{k^2}{k^4 + 4m^2k_{\parallel}^2} \\ \text{Re}\{S^{+-}(\mathbf{k})\} &= \frac{\mathbf{k}\sigma^3\mathbf{k}}{k^2} - (\mathbf{k}\sigma^4\mathbf{k})\frac{k^2}{k^4 + 4m^2k_{\parallel}^2} \\ \text{Im}\{S^{+-}(\mathbf{k})\} &= (\mathbf{k}\sigma^5\mathbf{k})\frac{\varepsilon\Gamma_{\parallel}^{\frac{1}{2}}k_{\parallel}}{k^4 + 4m^2k_{\parallel}^2}, \end{aligned} \quad (4.39)$$

where $k = |\mathbf{k}|$ and

$$\begin{aligned} \sigma^1 &= \frac{(1 - \delta\tilde{\rho})^2}{(1 - \tilde{\rho})((1 - \delta\tilde{\rho})^2 - \tilde{\rho}^2)} \sigma^{++} - \frac{(1 - \tilde{\rho})\tilde{\rho}}{(1 - \tilde{\rho})((1 - \delta\tilde{\rho})^2 - \tilde{\rho}^2)} \sigma^{+-} \\ \sigma^2 &= \left[\frac{(1 - \delta\tilde{\rho})^2(1 - 2\tilde{\rho})}{(1 - \tilde{\rho})^2((1 - \delta\tilde{\rho})^2 - \tilde{\rho}^2)} - 1 \right] \frac{(1 - \tilde{\rho})}{(1 - 2\tilde{\rho})} \sigma^{++} \\ &\quad - \left[\frac{(1 - \delta\tilde{\rho})(1 - 2\tilde{\rho})}{(1 - \tilde{\rho})((1 - \delta\tilde{\rho})^2 - \tilde{\rho}^2)} - 1 \right] \frac{\tilde{\rho}}{(1 - 2\tilde{\rho})} \sigma^{+-} \\ \sigma^3 &= \frac{(1 - \tilde{\rho})\tilde{\rho}}{(1 - \tilde{\rho})((1 - \delta\tilde{\rho})^2 - \tilde{\rho}^2)} \sigma^{++} - \frac{\tilde{\rho}^2}{(1 - \tilde{\rho})((1 - \delta\tilde{\rho})^2 - \tilde{\rho}^2)} \sigma^{+-} \\ \sigma^4 &= \left[\frac{(1 - \delta\tilde{\rho})(1 - 2\tilde{\rho})}{(1 - \tilde{\rho})((1 - \delta\tilde{\rho})^2 - \tilde{\rho}^2)} + 1 \right] \frac{\tilde{\rho}}{(1 - 2\tilde{\rho})} \sigma^{++} \\ &\quad - \left[\frac{\tilde{\rho}^2(1 - 2\tilde{\rho})}{(1 - \tilde{\rho})^2((1 - \delta\tilde{\rho})^2 - \tilde{\rho}^2)} + 1 \right] \frac{(1 - \tilde{\rho})}{(1 - 2\tilde{\rho})} \sigma^{+-} \\ \sigma^5 &= \frac{\tilde{\rho}(2 - (1 + \delta)\tilde{\rho})}{(1 - \tilde{\rho})(1 - 2\tilde{\rho})} \sigma^{++} - \frac{(1 - \tilde{\rho})(1 - \delta\tilde{\rho}) + \tilde{\rho}^2}{(1 - \tilde{\rho})(1 - 2\tilde{\rho})} \sigma^{+-}. \end{aligned} \quad (4.40)$$

The above expressions for the σ 's are not particularly interesting (since we do not know the "coarse-grained" values of the parameters anyway) but it is important to note, that they are all positive definite in the physical range of the parameters, within the stability limit of the homogeneous phase. Also, they are diagonal but generically not expected to be proportional to the unit matrix. Now, referring the details of the integrations to

Appendix B, the transforms can be carried out exactly. We define

$$\begin{aligned}
E(\mathbf{x}) &\equiv \frac{\Gamma\left(\frac{d}{2}-1\right)}{4\pi^{\frac{d}{2}}} \frac{1}{r^{d-2}} \\
F_1(\mathbf{x}) &\equiv \frac{\cosh(mx_{\parallel})}{(2\pi)^{\frac{d}{2}}} \left(\frac{m}{r}\right)^{\frac{d-2}{2}} K_{\frac{d-2}{2}}(mr) \\
F_2(\mathbf{x}) &\equiv \frac{\sinh(mx_{\parallel})}{(2\pi)^{\frac{d}{2}}} \left(\frac{m}{r}\right)^{\frac{d-2}{2}} K_{\frac{d-2}{2}}(mr),
\end{aligned} \tag{4.41}$$

where $\Gamma(z)$ is the Gamma function and $K_{\nu}(z)$ is the modified Bessel function. Then the results are:

$$G^{++}(\mathbf{x}) = -\nabla\sigma^1\nabla E(\mathbf{x}) + \nabla\sigma^2\nabla F_1(\mathbf{x}) \tag{4.42}$$

$$G_e^{+-}(\mathbf{x}) = -\nabla\sigma^3\nabla E(\mathbf{x}) + \nabla\sigma^4\nabla F_1(\mathbf{x}) \tag{4.43}$$

$$G_o^{+-}(\mathbf{x}) = \frac{\varepsilon\Gamma_{\parallel}^{\frac{1}{2}}}{2m} \nabla\sigma^5\nabla F_2(\mathbf{x}), \tag{4.44}$$

where $G_{e,o}^{+-}$ are the parts of G^{+-} even or odd in x_{\parallel} , being the transforms of the real and imaginary parts of S^{+-} . The full correlation is, of course,

$$G^{+-}(\mathbf{x}) = G_e^{+-}(\mathbf{x}) + G_o^{+-}(\mathbf{x}). \tag{4.45}$$

This decomposition simply reflects the symmetries of the system in the presence of the field (4.7).

The first terms in (4.42) and (4.43), being proportional to r^{-d} , are the well known power law decays [13] due to ‘‘FDT-violation’’ [48]. The second terms in (4.42) and (4.43) and the single term in (4.44) produce an exponential decay for large r , *except* along the field. This can be easily deduced, since, for large r_{\parallel} , the exponentials of the hyperbolic and Bessel functions cancel. Leaving the detailed asymptotic expansions of the terms in (4.42-4.44) to Appendix C, we illustrate the main results as $mr \rightarrow \infty$.

For $r_{\perp} \neq 0$:

$$\begin{aligned}
G^{++}(\mathbf{x}) &\propto \frac{\sigma_{\parallel}^1 - \sigma_{\perp}^1}{r^d} \left[\frac{r_{\perp}^2 - (d-1)r_{\parallel}^2}{r^2} \right] + \dots \\
G^{+-}(\mathbf{x}) \simeq G_e^{+-}(\mathbf{x}) &\propto \frac{\sigma_{\parallel}^3 - \sigma_{\perp}^3}{r^d} \left[\frac{r_{\perp}^2 - (d-1)r_{\parallel}^2}{r^2} \right] + \dots,
\end{aligned} \tag{4.46}$$

where the ... represent exponential, short-ranged tails. In this form, we emphasize the three key ingredients of the ‘‘FDT-violating’’ power law decays, namely, the dependence

on $\sigma_{\parallel} \neq \sigma_{\perp}$ (or $\sigma_{\parallel}/\Gamma_{\parallel} \neq \sigma_{\perp}/\Gamma_{\perp}$ before rescaling the noise matrices), the dipole amplitude and, of course, the r^{-d} . Also, note that the part of G^{+-} odd in x_{\parallel} is found to be only short-ranged, as indirectly indicated in (4.46).

The more interesting limit is for $r_{\perp} = 0$. Then, in addition to the above power laws, we have another power, $r_{\parallel}^{-(d+1)/2}$:

$$\begin{aligned} G^{++}(\mathbf{0}, x_{\parallel}), G_e^{+-}(\mathbf{0}, x_{\parallel}) &\propto -r_{\parallel}^{-\frac{d+1}{2}} + \mathcal{O}\left(\max\left\{r_{\parallel}^{-d}, r_{\parallel}^{-\frac{d+3}{2}}\right\}\right) \\ G_o^{+-}(\mathbf{0}, x_{\parallel}) &\propto -\text{sgn}(\varepsilon x_{\parallel}) r_{\parallel}^{-\frac{d+1}{2}} + \mathcal{O}\left(r_{\parallel}^{-\frac{d+3}{2}}\right). \end{aligned} \quad (4.47)$$

For all $d > 1$, this power will dominate over the ‘‘FDT-violating’’ component. In fact, if we study $d > 3$ systems, even the *next* leading term, related to the asymptotic expansion of $K_{\frac{d-2}{2}}$, will be more important than r^{-d} . Note that in (4.47), to emphasize the sign of the amplitude of the leading power, we included explicit factors of (-1) , so that the proportionality constants in (4.47) are positive. In conclusion, the spatial correlations are dominated by the expected r^{-d} power law, except along the field, where a novel $r_{\parallel}^{-(d+1)/2}$ decay takes over. This new power law comes from the coupling between the two species as a result of the excluded volume constraint and the opposite bias.

4.3.3 The $\gamma = 1$ case

All formulas simplify tremendously when we set $\gamma = 1$, yet they still capture the essence of this two species model, namely, the non-trivial correlations between opposite charges:

$$\begin{aligned} S^{++}(\mathbf{k}) &= \frac{\mathbf{k}\boldsymbol{\sigma}^{++}\mathbf{k}}{k^2} \\ \text{Re}\{S^{+-}(\mathbf{k})\} &= (\mathbf{k}\boldsymbol{\sigma}^{+-}\mathbf{k}) \frac{k^2}{k^4 + 4m^2 k_{\parallel}^2} \\ \text{Im}\{S^{+-}(\mathbf{k})\} &= (\mathbf{k}\boldsymbol{\sigma}^{+-}\mathbf{k}) \frac{-\text{sgn}(\varepsilon) 2m k_{\parallel}}{k^4 + 4m^2 k_{\parallel}^2}, \end{aligned} \quad (4.48)$$

where now $4m^2 = (1 - 2\bar{\rho})^2 \varepsilon^2 \Gamma_{\parallel}$. It is also clear from the formulas above that no instabilities are possible (at $\bar{\rho} = 1/2$ the system becomes equivalent to the driven one species model). Also note that the form of the $++$ structure factor is the same as in the one species model, as a result of the fact that $+$'s cannot distinguish between $-$'s and holes at the microscopic level. The difficult question is, of course, whether the $\boldsymbol{\sigma}$'s (especially $\boldsymbol{\sigma}^{++}$) are proportional to the unit matrix or not. Unfortunately, without renormalization group analysis we have to rely on simulations to answer these questions. Based on the results of the previous subsection, it is clear that only $S^{++}(\mathbf{k})$ could produce the r^{-d} power law. However, having

seen our simulation results, we believe that the internal symmetry of the system, at this particular value of γ , restores FDT for either species (the first equation in (4.21)). This is entirely consistent with the fact that the microscopic steady state distribution of either species is uniform, as we mentioned earlier. Thus, correlations are going to be short ranged (δ -function for identical species and exponential decay for opposite charges), except in the field direction, between opposite species, where:

$$G^{+-}(\mathbf{0}, x_{\parallel}) \simeq 2 \Theta(\varepsilon x_{\parallel}) \sigma_{\perp}^{+-} \frac{\sqrt{\frac{\pi}{2}}}{(2\pi)^{\frac{d}{2}}} \left\{ \frac{d-1}{2m} \left(\frac{m}{r_{\parallel}} \right)^{\frac{d+1}{2}} + \mathcal{O} \left(\frac{1}{r_{\parallel}^{\frac{d+3}{2}}} \right) \right\}. \quad (4.49)$$

Here $\Theta(x)$ is the step function and also note that σ_{\perp}^{+-} is always negative. Thus, this novel $r_{\parallel}^{-(d+1)/2}$ power law survives even in this extreme case, in the cross correlation. This is the feature which characterizes this two species model and, in fact, it is the existence of transverse dimensions (i.e. $d > 1$) that makes it possible to generate this novel power law decay along the longitudinal direction.

4.3.4 Distribution of structure factors

Now, we seek the *probability distributions* of the density-density operators, following the method of [52]. Thus, for each \mathbf{k} vector, we construct the marginal distributions separately for $\frac{\chi^+(\mathbf{k}, t)\chi^+(-\mathbf{k}, t)}{V}$, $\frac{\text{Re}[\chi^+(\mathbf{k}, t)\chi^-(-\mathbf{k}, t)]}{V}$ and $\frac{\text{Im}[\chi^+(\mathbf{k}, t)\chi^-(-\mathbf{k}, t)]}{V}$, represented by s^{++} , s_r^{+-} and s_i^{+-} :

$$\begin{aligned} P^{++}(s^{++}; \mathbf{k}) &= \left\langle \delta \left(\frac{\chi^+(\mathbf{k}, t)\chi^{+*}(\mathbf{k}, t)}{V} - s^{++} \right) \right\rangle \\ P_r^{+-}(s_r^{+-}; \mathbf{k}) &= \left\langle \delta \left(\frac{\text{Re}[\chi^+(\mathbf{k}, t)\chi^{-*}(\mathbf{k}, t)]}{V} - s_r^{+-} \right) \right\rangle \\ P_i^{+-}(s_i^{+-}; \mathbf{k}) &= \left\langle \delta \left(\frac{\text{Im}[\chi^+(\mathbf{k}, t)\chi^{-*}(\mathbf{k}, t)]}{V} - s_i^{+-} \right) \right\rangle. \end{aligned} \quad (4.50)$$

The normalization by V helps to avoid infinities in the expectation values of s^{++} , s_r^{+-} , s_i^{+-} as can be seen from (4.28) and by noting that $(2\pi)^d \delta(\mathbf{k} = \mathbf{0}) = V$ in the infinite volume limit. Also note that we used $\chi^{\pm}(-\mathbf{k}, t) = \chi^{\pm*}(\mathbf{k}, t)$, since the densities $\chi^{\pm}(\mathbf{r}, t)$ are real. For our purposes, we need both the density fluctuations and the explicit distribution of the noise, in the (\mathbf{k}, t) domain. Within the linear stability regime of the disordered phase, each matrix element of $((L^{-1})^{\alpha\beta})$ has two poles in the positive ω half-plane corresponding to two stable eigenvalues of $(\mathcal{L}^{\alpha\beta})$ as we saw earlier in eq. (4.29). Thus, from (4.24) we find:

$$\chi^{\alpha}(\mathbf{k}, t) = \int_{-\infty}^t dt' \left[\int_{-\infty}^{\infty} \frac{d\omega}{2\pi} e^{i\omega(t-t')} (L^{-1})^{\alpha\beta} \right] i\mathbf{k}\boldsymbol{\eta}^{\beta}(\mathbf{k}, t') \quad (4.51)$$

with

$$P[\eta_i^\alpha(\mathbf{k}, t)] \propto \exp \left\{ -\frac{1}{2} \int dt d^d k \eta_i^\alpha(\mathbf{k}, t) \frac{(D^{-1})_{ij}^{\alpha\beta}}{(2\pi)^d} \eta_j^{\beta*}(\mathbf{k}, t) \right\}, \quad (4.52)$$

where $D_{ij}^{\alpha\beta} \equiv 2\sigma_{ij}^{\alpha\beta}$ in our model. Due to translational invariance, fields with different \mathbf{k} vectors are decoupled, so we will suppress \mathbf{k} in the following. Then (4.51) can be written as

$$\chi^\alpha(t) = v_j^{\alpha\beta}(t, t') \eta_j^\beta(t') \quad (4.53)$$

where

$$v_j^{\alpha\beta}(t, t') = \Theta(t - t') \left[\int_{-\infty}^{\infty} \frac{d\omega}{2\pi} e^{i\omega(t-t')} (L^{-1})^{\alpha\beta} \right] ik_j. \quad (4.54)$$

Note that summation over repeated indices also includes an integral over t' in (4.53).

We start with the probability distribution of $\frac{\chi^+(t)\chi^{+*}(t)}{V}$ by first finding its characteristic function, i.e.,

$$\tilde{P}^{++}(\Omega) = \int_{-\infty}^{\infty} ds^{++} e^{i\Omega s^{++}} P^{++}(s^{++}) = \left\langle e^{i\Omega \frac{\chi^+(t)\chi^{+*}(t)}{V}} \right\rangle. \quad (4.55)$$

When performing the average in (4.55), all integrations over the noise are trivial, except those associated with $\pm\mathbf{k}$. Thus, we need to evaluate the following integral:

$$\tilde{P}^{++}(\Omega) = \int \prod_{t', \gamma, j} d\eta_j^\gamma(t') d\eta_j^{\gamma*}(t') P[\eta_i^\alpha(t), \eta_i^{\alpha*}(t)] e^{i\Omega \frac{\chi^+(t)\chi^{+*}(t)}{V}} \quad (4.56)$$

where $\eta_j^\gamma(t')$ and $\eta_j^{\gamma*}(t')$ are the \mathbf{k} and $-\mathbf{k}$ components of the noise, respectively, yielding the only non-trivial integrations. Inserting (4.53) into (4.56), we still have a Gaussian integrand, controlled by the quadratic form:

$$\eta_\mu \left((D^{-1})_{\mu\nu} - i\Omega v_\mu^+ v_\nu^{+*} \right) \eta_\nu^*, \quad (4.57)$$

where the indices μ, ν include all the degrees of freedom left over, namely, time, charge, and spatial component. The corresponding path integrals lead to

$$\tilde{P}^{++}(\Omega) = \frac{\det[(D^{-1})_{\mu\nu}]}{\det[(D^{-1})_{\mu\nu} - i\Omega v_\mu^+ v_\nu^{+*}]} = \frac{1}{\det[\delta_{\mu\nu} - i\Omega D_{\mu\gamma} v_\gamma^+ v_\nu^{+*}]}, \quad (4.58)$$

where the numerator in the middle expression originates in the normalization factor ensuring $\tilde{P}^{++}(0) = 1$. Exploiting the formula $\det(\delta_{\mu\nu} + a_\mu b_\nu) = 1 + a_\mu b_\mu$, as a special case of a more general one (see Appendix D), we obtain

$$\tilde{P}^{++}(\Omega) = \frac{1}{1 - i\Omega v_\mu^+ D_{\mu\nu} v_\nu^{+*}}. \quad (4.59)$$

Note that the coefficient of $i\Omega$ is simply the ‘++’ structure factor:

$$v_\mu^+ D_{\mu\nu} v_\nu^{+*} = \left\langle \frac{\chi^+(\mathbf{k}, t) \chi^{+*}(\mathbf{k}, t)}{V} \right\rangle = S^{++}(\mathbf{k}). \quad (4.60)$$

Taking the inverse transform to obtain P^{++} , the single pole $-i/S^{++}(\mathbf{k})$ in the lower half Ω -plane yields an exponential distribution for the non-negative variable s^{++} , i.e.,

$$P^{++}(s^{++}; \mathbf{k}) = \begin{cases} \frac{1}{S^{++}(\mathbf{k})} e^{-s^{++}/S^{++}(\mathbf{k})} & \text{if } s^{++} \geq 0 \\ 0 & \text{if } s^{++} < 0 \end{cases} \quad (4.61)$$

We will refer to $1/S^{++}(\mathbf{k})$ as the ‘decay factor’ of the exponential.

Next, we consider the distribution of $\frac{\text{Re}[\chi^+(t)\chi^{-*}(t)]}{V}$. Following the same steps, we see that the quadratic form controlling the Gaussian integrand is

$$\eta_\mu \left((D^{-1})_{\mu\nu} - \frac{i\Omega}{2} (v_\mu^+ v_\nu^{-*} + v_\mu^- v_\nu^{+*}) \right) \eta_\nu^*, \quad (4.62)$$

leading to

$$\tilde{P}_r^{+-}(\Omega) = \frac{1}{\det \left[\delta_{\mu\nu} - \frac{i\Omega}{2} (D_{\mu\gamma} v_\gamma^+ v_\nu^{-*} + D_{\mu\gamma} v_\gamma^- v_\nu^{+*}) \right]}. \quad (4.63)$$

Using the formula $\det(\delta_{\mu\nu} + a_\mu b_\nu + c_\mu d_\nu) = 1 + [a_\mu b_\mu + c_\mu d_\mu] + [(a_\mu b_\mu)(c_\nu d_\nu) - (a_\mu d_\mu)(b_\nu c_\nu)]$ (Appendix D), we arrive at

$$\tilde{P}_r^{+-}(\Omega) = \frac{1}{1 - i\Omega \text{Re}[S^{+-}(\mathbf{k})] + \frac{\Omega^2}{4} [|S^{++}(\mathbf{k})|^2 - |S^{+-}(\mathbf{k})|^2]}, \quad (4.64)$$

where, similarly to (4.60), we have used

$$v_\mu^+ D_{\mu\nu} v_\nu^{-*} = \left\langle \frac{\chi^+(\mathbf{k}, t) \chi^{-*}(\mathbf{k}, t)}{V} \right\rangle = S^{+-}(\mathbf{k}). \quad (4.65)$$

Unlike the previous case, $\tilde{P}_r^{+-}(\Omega)$ has two poles: one (Ω_-) being on the negative, and the other (Ω_+) on the positive, imaginary axis:

$$\Omega_{\mp} = \frac{2i}{\Delta} \left(\text{Re}[S^{+-}(\mathbf{k})] \mp \sqrt{\Delta + (\text{Re}[S^{+-}(\mathbf{k})])^2} \right) \quad (4.66)$$

where $\Delta \equiv |S^{++}(\mathbf{k})|^2 - |S^{+-}(\mathbf{k})|^2 > 0$. In general, their magnitudes are different. Thus, the inverse transform yields an *asymmetric* exponential distribution, characterized by two distinct decay factors $|\Omega_+|$ and $|\Omega_-|$:

$$P_r^{+-}(s_r^{+-}; \mathbf{k}) = \begin{cases} \frac{1}{N} e^{-|\Omega_-|s_r^{+-}} & \text{if } s_r^{+-} \geq 0 \\ \frac{1}{N} e^{|\Omega_+|s_r^{+-}} & \text{if } s_r^{+-} < 0 \end{cases} \quad (4.67)$$

		fit parameters:
$S^{++}(\mathbf{k})$:	$\frac{\sigma_{\parallel}^1}{\Gamma_{\parallel}} / \frac{\sigma_{\perp}^1}{\Gamma_{\perp}} = 0.833$	$\Gamma_{\parallel} / \Gamma_{\perp} = 0.712$ $m = 0.0442$
	$\frac{\sigma_{\parallel}^2}{\Gamma_{\parallel}} / \frac{\sigma_{\perp}^2}{\Gamma_{\perp}} = 0.658$	
$\text{Re}\{S^{+-}(\mathbf{k})\}$:	$\frac{\sigma_{\parallel}^3}{\Gamma_{\parallel}} / \frac{\sigma_{\perp}^3}{\Gamma_{\perp}} = 0.732$	
	$\frac{\sigma_{\parallel}^4}{\Gamma_{\parallel}} / \frac{\sigma_{\perp}^4}{\Gamma_{\perp}} = 0.764$	
$\text{Im}\{S^{+-}(\mathbf{k})\}$:	$\frac{\sigma_{\parallel}^5}{\Gamma_{\parallel}} / \frac{\sigma_{\perp}^5}{\Gamma_{\perp}} = 0.780$	

Table 4.1: Fitting the analytical results to simulation data of an $L = 100$ system at $\gamma = 0.02$, $E = 0.279$ and $\bar{\rho} = 0.175$. Fitted curves are plotted in Fig. 4.2, together with simulation data. Note that with the mean-field parameters, m would be $m_{mf} = 0.0716$.

with $N = \sqrt{\Delta + (\text{Re}[S^{+-}(\mathbf{k})])^2}$. To obtain the distribution of $\frac{\text{Im}[x^+(t)x^{-*}(t)]}{V}$ we simply interchange $\text{Re}[S^{+-}(\mathbf{k})]$ and $\text{Im}[S^{+-}(\mathbf{k})]$ in eqs. (4.66,4.67).

One important consequence of (4.61) and (4.67) is that their standard deviations always take a value *greater or equal* than the average. In particular

$$\begin{aligned}
\sqrt{(s^{++})^2 - (\overline{s^{++}})^2} &= S^{++}(\mathbf{k}) \\
\sqrt{(s_r^{+-})^2 - (\overline{s_r^{+-}})^2} &= \sqrt{(\text{Re}[S^{+-}(\mathbf{k})])^2 + \frac{\Delta}{2}} \\
\sqrt{(s_i^{+-})^2 - (\overline{s_i^{+-}})^2} &= \sqrt{(\text{Im}[S^{+-}(\mathbf{k})])^2 + \frac{\Delta}{2}}.
\end{aligned} \tag{4.68}$$

Thus, when measuring structure factors in the *disordered* phase, fluctuations comparable to the average should not come as a surprise. We also emphasize that formulas (4.61) and (4.67) are completely independent of the specific model and can be derived in any multicomponent system. The only necessary conditions are linear Langevin equations with Gaussian noise.

4.4 Discussion

Finally, let us turn to comparisons with simulation results. Typically, we find that power law tails are difficult to observe, in relatively small systems such as ours. Thus, we focus on the structure factors. We fitted our analytical results (eqs. (4.39) and (4.48) before rescaling) to our simulation data, and the relevant parameters (with choosing $\Gamma_{\perp} = 1$)

	fit parameters:
$S^{++}(\mathbf{k})$:	$\sigma^{++} = \bar{\rho}(1 - \bar{\rho})\Gamma$
$\text{Re}\{S^{+-}(\mathbf{k})\}$:	$\frac{\sigma_{\parallel}^{+-}}{\Gamma_{\parallel}} / \frac{\sigma_{\perp}^{+-}}{\Gamma_{\perp}} = 1.12 \quad \Gamma_{\parallel}/\Gamma_{\perp} = 0.559$
$\text{Im}\{S^{+-}(\mathbf{k})\}$:	$m = 0.331$

Table 4.2: Fitting the analytical results to simulation data of an $L = 100$ system at $\gamma = 1$, $E = \infty$ and $\bar{\rho} = 0.25$. Fitted curves are plotted in Fig. 4.3, together with simulation data. Note that with the mean-field parameters, m would be $m_{mf} = 0.353$.

are summarized in Table 4.1 and Table 4.2. The agreement is quite good, but note the following: for the $\gamma = 0.02$ case (Fig. 4.2), despite being in the homogeneous phase, the system was relatively close to the continuous transition, with $m \sim 4 \times 10^{-2}$ corresponding to a correlation length $\xi \sim 25$ in the units of lattice constant. In particular, “longitudinal parameters”, such as the σ_{\parallel} ’s and Γ_{\parallel} seem to suffer considerable renormalizations here. On the other hand, “transverse components” seem to obey the relation in (4.21) which can be seen as follows. Combining (4.21) with the explicit form of the structure factors (4.31) for $k_{\parallel} = 0$ yields the exact “finite size” amplitudes, completely independent of \mathbf{k}_{\perp} , for the transverse structure factors: $S^{++}(\mathbf{k}_{\perp}, 0) = \bar{\rho}(1 - \bar{\rho})$ and $S^{+-}(\mathbf{k}_{\perp}, 0) = -\bar{\rho}^2$, in perfect agreement with the simulations. As a result of the coarse-graining effect in the field direction, we generically found $\sigma_{\parallel}/\Gamma_{\parallel} \neq \sigma_{\perp}/\Gamma_{\perp}$ for the rescaled noise matrices (Table 4.1). In particular we had $\sigma_{\parallel}^1/\Gamma_{\parallel} = 0.833 \sigma_{\perp}^1/\Gamma_{\perp}$, predicting the typical FDT-violating power law.

For $\gamma = 1.00$ (Fig. 4.3), as we expected, $S^{++}(\mathbf{k})$ is completely flat, indicating that $\sigma_{\parallel}^{++}/\Gamma_{\parallel} = \sigma_{\perp}^{++}/\Gamma_{\perp}$. Moreover, the value of this constant $S^{++}(\mathbf{k})$ is just $\bar{\rho}(1 - \bar{\rho})$, again consistent with (4.21). On the other hand, $S^{+-}(\mathbf{k})$ clearly exhibits the structure of eqs. (4.48). Here the system is far from transitions ($\xi \sim 3$), so that critical fluctuations are completely avoided. Consequently, using $m = \frac{1}{2}(1 - 2\bar{\rho})|\varepsilon|\Gamma_{\parallel}^{\frac{1}{2}}$ with the mean-field parameters produces the mass closely matching the one obtained from the fit.

Now, we turn to a comparison of the analytical results for the structure factor distributions with the simulations, summarized in Figs. 4.6 and 4.7, for the two smallest wave vectors, respectively. The control parameters were the same as those of Fig. 4.2. This is another way to test the framework, in which the above structure factors and corresponding spatial correlations were calculated. The ‘++’ histograms show the usual exponential decay [52], while the ‘+-’ histograms clearly represent asymmetric exponential distributions. To test the predictions of our Gaussian theory, namely, that the slopes of the histograms are determined by the structure factor averages themselves, we simply measured these averages, i.e., S^{++} , $\text{Re}S^{+-}$ and $\text{Im}S^{+-}$. The ‘++’ case is particularly simple since the decay factor

$\mathbf{k} = \frac{2\pi}{L}(0, 1)$	Measured averages:		
	$S^{++}(\mathbf{k}) = 0.209$	$\text{Re}\{S^{+-}(\mathbf{k})\} = 0.109$	$\text{Im}\{S^{+-}(\mathbf{k})\} = 0.0704$
	Calculated decay factors of the theoretical distributions:		
	$P^{++}(s^{++}; \mathbf{k}):$	$P_r^{+-}(s_r^{+-}; \mathbf{k}):$	$P_i^{+-}(s_i^{+-}; \mathbf{k}):$
positive s axis:	$1/S^{++}(\mathbf{k}) = 4.78$	$ \Omega_- = 6.53$	$ \Omega_- = 8.03$
negative s axis:	" ∞ "	$ \Omega_+ = 22.69$	$ \Omega_+ = 18.45$

Table 4.3: Calculated decay factors of the theoretical distributions for $\mathbf{k} = \frac{2\pi}{L}(0, 1)$.

$\mathbf{k} = \frac{2\pi}{L}(1, 0)$	Measured averages:		
	$S^{++}(\mathbf{k}) = 0.143$	$\text{Re}\{S^{+-}(\mathbf{k})\} = -0.0371$	$\text{Im}\{S^{+-}(\mathbf{k})\} = 0.00252$
	Calculated decay factors of the theoretical distributions:		
	$P^{++}(s^{++}; \mathbf{k}):$	$P_r^{+-}(s_r^{+-}; \mathbf{k}):$	$P_i^{+-}(s_i^{+-}; \mathbf{k}):$
positive s axis:	$1/S^{++}(\mathbf{k}) = 7.00$	$ \Omega_- = 18.92$	$ \Omega_- = 14.24$
negative s axis:	" ∞ "	$ \Omega_+ = 11.11$	$ \Omega_+ = 14.77$

Table 4.4: Calculated decay factors of the theoretical distributions for $\mathbf{k} = \frac{2\pi}{L}(1, 0)$.

is just the inverse of S^{++} itself. For the two '+-' distributions, we inserted the *measured* averages into the non-trivial *theoretical* relationship (4.66), to find the decay factors $|\Omega_{\mp}|$. The normalization factors were simply obtained by fitting the distributions at the origin. We summarize the above procedure in Table 4.3 and 4.4, for $\mathbf{k} = \frac{2\pi}{L}(0, 1)$ and $\mathbf{k} = \frac{2\pi}{L}(1, 0)$. The results are plotted together with the histograms found in simulations, in Fig. 4.6 and 4.7. The agreement between simulation results and theory is remarkably good, indicating that linearized Langevin equations are quite acceptable in this regime. While the external field, E , may obviously generate renormalizations, these can be absorbed in the effective parameters of the theory, namely the diffusion matrix, the noise matrix, the average density and the coarse-grained bias, leaving the *form* of the structure factor distributions invariant. However, we must avoid critical fluctuations since the linear approximation will fail to capture their effects correctly.

To summarize, using both simulation and analytic techniques, we have examined the structure factors in a simple model of biased diffusion of two species. Then we calculated the corresponding spatial correlations, and we find the expected power law decay, r^{-d} , typical of non-equilibrium steady states of a system with anisotropy and subjected to a conservation law. In addition, a novel power, $r_{\parallel}^{-(d+1)/2}$, is found for correlations along the bias. The general agreement between simulations and a simple coarse-grained description

is surprisingly good, while we await a renormalization group analysis of the continuum theory of the model in order to make detailed comparisons for the universal quantities of the system.

Chapter 5

Summary and Outlook

In this Dissertation, we focused on a simple non-equilibrium model exhibiting a rich phase diagram and non-equilibrium steady states. We considered two species of particles on a regular lattice (empty lattice sites are labeled as holes). Referring to the particles as $+$'s and $-$'s, they are driven in opposite directions with jump rates against the force being exponentially suppressed, subject to periodic boundary conditions in two dimensions. To keep the model simple, only the excluded volume constraint is taken into account. In the simplest scenario "charge" ($+-$) exchange is not allowed. Earlier studies, in particular Monte Carlo simulations and mean-field approaches showed that there is a transition, controlled by overall particle density \bar{m} and drive E , from a spatially homogeneous (disordered) phase to a charge segregated one, where the excluded volume constraint and the opposite bias lead to the mutual blocking of particles. We found that if one softens the excluded volume constraint - by allowing exchange between nearest neighbor, oppositely charged particles on a much slower time scale (γ) than the particle-hole exchange, - the above transition still survives.

By using both Monte Carlo simulations and continuum mean-field theory techniques, we mapped out the (\bar{m}, E, γ) phase diagram, determined the order of the phase transitions and studied density profiles. A single sheet of transitions was found in the (\bar{m}, E, γ) space. The nature of the transitions is first order on parts of this sheet and continuous on other parts, with a line of multicritical points as the common boundary. The adiabatic elimination of the fast modes provided us with a Ginzburg-Landau type equation for the (complex) amplitude of the slow mode, yielding a good qualitative phase diagram including the existence of multicritical points.

In the disordered phase, where translational invariance is preserved, we analyzed structure factors, their distributions and spatial correlations, employing both MC simulations and field theory methods. We found a finite discontinuity singularity in the structure factors at the origin which translates to power law decays in spatial correlations. Furthermore,

by analyzing the full probability distributions of structure factors, one obtains model independent information about general multi-species systems, namely, how the parameters of those distributions depend on the average structure factors themselves.

Possible extensions of this research include the following projects:

(i.) The region near complete filling at non-zero field has not been explored in detail. It is here that the competition between ordering, mediated by the combination of bias and excluded volume constraint, and disordering, by virtue of charge exchange, may well be at its most subtle. The system is known to be disordered at $\bar{m} = 1$, where the model can be mapped to the biased diffusion of a single species. Simulation results for our relatively small (30×30) system indicate that for small γ and large E , the removal of just two particles (i.e., introducing a single pair of holes) suffices to induce spatial inhomogeneities, with the two holes performing a biased random walk which leaves a charge segregated region in its wake. The holes act as catalysts for the charge segregation process, creating a domain of predominantly positive charge separated by a sharp interface from a similar, negatively dominated region. Expelled from either region, the holes remain *localized* at the interface. We should be able to learn more about this “self-trapping” mechanism by tracing the time evolution of the hole-hole correlation function. Furthermore, a simple description of the steady state distribution should be possible based on the above attractive effective interaction between holes. Work is in progress to understand whether the transition line meets the $\bar{m} = 1$ line at some finite, γ -dependent E , or whether a finite region of disordered phase remains, for all E . In the latter case the system would display reentrant behavior. To decide whether a finite number or a finite density of holes is sufficient to induce spatial inhomogeneities, clearly requires a detailed finite size analysis in this region.

(ii.) A second interesting issue concerns the *universality class* of the continuous transition. We already mentioned in Chapter 2 that if one performs the adiabatic elimination procedure for the corresponding Langevin equations then our two dimensional simulations will be described by an effective theory in one (transverse) dimension for a complex order parameter, which nevertheless exhibits a phase transition. Clearly, this cannot be understood in terms of an equivalent $O(2)$ or XY model in one dimension, since those models do not exhibit a phase transition below three dimensions. Also, as a result of the elimination of the fast modes, both additive and multiplicative noise terms will be present in the equation of motion for the slow mode and their roles in inducing transitions should be investigated.

(iii.) So far we have studied two dimensional systems. On the other hand, a one dimensional version of the two species model has been solved exactly and indicates that the steady state is always disordered: although there are particle clusters in the system, their typical length does not scale with the system size, thus, no long range order results. The question naturally arises: what is the *role of the transverse dimension*, i.e., what is the consequence of allowing particles to pass each other? Our preliminary results indicate that, surprisingly, even a two column ($2 \times L$) system already orders into a spatially inhomogeneous steady

state, at appropriate values of the control parameters. On the analytic side, using the steady state results for the one dimensional case, one may consider the transverse jumps as a perturbation by introducing a small transverse overall hopping rate (fast rate limit). Then it should be possible to analyze how instabilities cause the breaking of translational invariance.

(iv.) Viewed from a different perspective, the two species model without a bias can also serve as a simple model for the dynamics of corrosion. We consider two species of particles, initially separated by a perfectly sharp interface and a few highly mobile impurities (holes) localized at the interface. Clearly, the system evolves toward a completely disordered (mixed) configuration as the holes perform random walks and eventually the interface will be completely destroyed by these *Brownian vacancies*. Analyzing the time evolution of the appropriate “disorder” parameter, we observed convincing dynamical scaling, exhibiting three time regimes separated by two crossover times. Clearly, numerous other effects such as, e.g., those due to interaction between particles, can be investigated.

To summarize, we used standard techniques to study non-equilibrium phase transitions and steady states in a simple three-state driven stochastic lattice gas. Through our study, we explored generic non-equilibrium features as well as novel behavior. We managed to establish an analytical description of the problem, first, in terms of a simple mean-field theory, then later, in terms of a set of Langevin equations, so that our simulation observations were compared to analytic results in most cases. We believe that our findings help to understand collective behavior in many-particle systems far from equilibrium.

Bibliography

- [1] J.W. Gibbs, *The Elementary Principles in Statistical Mechanics*, (Scribner, N.Y., 1902)
- [2] S.R. de Groot and P. Mazur, *Non-equilibrium Thermodynamics*, (North Holland, Amsterdam, 1962)
- [3] E. Ising, *Z. Phys.* **31** (1925) 253.
- [4] L. Onsager, *Phys. Rev.* **65** (1944) 117.
- [5] L.P. Kadanoff, *Physics* **2** (1966) 263; M.E. Fisher, *Rep. Prog. Phys.* **30** (1967) 615; K.G. Wilson, *Rev. Mod. Phys.* **47C** (1975) 773.
- [6] K. Binder, D.W. Heermann, *Monte Carlo Simulations in Statistical Physics* (Springer-Verlag, Berlin, 1988); *Finite Size Scaling and Numerical Simulations of Statistical Systems* ed. V. Privman (World Scientific, Singapore, 1990).
- [7] S. Katz, J.L. Lebowitz and H. Spohn, *Phys. Rev.* **B28** (1983) 1655; *J. Stat. Phys.* **34** (1984) 497 .
- [8] K. Kawasaki, *Phys. Rev.* **148** (1966) 375 and *Phase Transitions and Critical Phenomena* Vol. 2, eds. C. Domb and M.S. Green, (Academic Press, N.Y., 1972).
- [9] N. Metropolis, A.W. Rosenbluth, M.M Rosenbluth, A.H. Teller and E. Teller, *J. Chem. Phys.* **21** (1953) 1087.
- [10] P.C. Martin, E.D. Siggia and H.H. Rose, *Phys. Rev.* **A8** (1973) 423; H.K. Janssen, *Z. Phys.* **B23** (1976) 377; C. de Dominicis, *J. Phys. (Paris) Colloq.* **37** (1976) C247; R. Bausch, H.K. Janssen and H. Wagner, *Z. Phys.* **B24** (1976) 113.
- [11] H.K. Janssen and B. Schmittmann, *Z. Phys.* **B64** (1986) 503; K.-t Leung and J.L.Cardy, *J. Stat. Phys.* **44** (1986) 567 and (1986) 1087.
- [12] K.-t. Leung, *Phys. Rev. Lett.* **66** (1991) 453 and *Int. J. Mod. Phys.* **C3** (1992) 367.

- [13] M.Q. Zhang, J.-S. Wang, J.L. Lebowitz and J.L. Vallés, *J. Stat. Phys.* **52** (1988) 1461.
- [14] R. Kubo, *Rep. Progr. Phys.* **29** (1966) 255.
- [15] B. Schmittmann and R.K.P. Zia, *Phase Transitions and Critical Phenomena* Vol. 17, eds. C. Domb and J.L. Lebowitz, (Academic Press, N.Y., 1995).
- [16] *Solid Electrolytes*, ed. S. Geller, *Topics in Applied Physics* Vol. 21 (Springer, Heidelberg, 1979); *Fast Ionic Transport in Solids*, eds. J.B. Bates and G.C. Farrington (North Holland, N.Y., 1981); *The Physics of Superionic Conductors and Electrode Materials*, ed. J.W. Perram (Plenum, N.Y., 1983).
- [17] See e.g., S. Chandra, *Superionic Solids. Principles and Applications* (North Holland, Amsterdam 1981)
- [18] H.-F. Eicke, M. Borkovec and B. Das-Gupta, *J. Chem. Phys.* **93** (1989) 314.
- [19] P.G. de Gennes, *J. Chem. Phys.* **55** (1971) 572; M. Rubinstein, *Phys. Rev. Lett.* **59** (1987) 1946; T.A.J. Duke, *Phys. Rev. Lett.* **62** (1989) 2877; B. Widom, J.L. Viovy and A.D. Desfontaines, *J. Phys I (France)* **1** (1991) 1759.
- [20] J.W. Jorgenson, *New Directions in Electrophoretic Methods* ACS Symposium Series No. 335, American Chemical Society, Washington, D.C. (1987)
- [21] Y. Schnidman, *Mathematics in Industrial Problems IV*, ed. A. Friedman (Springer, Berlin 1991).
- [22] O. Biham, A.A. Middleton, and D. Levine, *Phys. Rev.* **A46** (1992) R6128; K.-t. Leung, *Phys. Rev. Lett.* **73** (1994) 2386.
- [23] R.B. Potts, *Proc. Camb. Phil. Soc.* **48** (1952) 106; F.Y. Wu, *Rev. Mod. Phys.* **54** (1982) 235.
- [24] M. Blume, V.J. Emery and R.B. Griffiths, *Phys. Rev.* **A4** (1971) 1071.
- [25] M. Aertsens and J. Naudts, *J. Stat. Phys.* **62** (1990) 609.
- [26] B. Schmittmann, K. Hwang and R.K.P. Zia, *Europhys. Lett.* **19** (1992) 19.
- [27] D.P. Foster, C. Godrèche, *J. Stat. Phys.* **76** (1994) 1129.
- [28] I. Vilfan, R.K.P. Zia and B. Schmittmann, *Phys. Rev. Lett.* **73** (1994) 2071.
- [29] K.E. Bassler, B. Schmittmann and R.K.P. Zia, *Europhys. Lett.* **24** (1993) 115

- [30] H.K. Janssen and B. Schmittmann, *Z. Phys.* **B63** (1986) 517; H. van Beijeren, R. Kutner and H. Spohn, *Phys. Rev. Lett.* **54** (1985) 2026.
- [31] G. Korniss, B. Schmittmann and R.K.P. Zia, *Europhys. Lett.* **32** (1995) 49 and *J. Stat. Phys.* **86** (1997) 721.
- [32] B. Derrida, S.A. Janowsky, J.L. Lebowitz and E.R. Speer, *Europhys. Lett.* **22** (1993) 651 and *J. Stat. Phys.* **73** (1993) 813.
- [33] S. Sandow, C. Godrèche private communications, to be submitted.
- [34] M.R. Evans, D.P. Foster, C. Godrèche and D. Mukamel, *Phys. Rev. Lett.* **78** (1995) 208 and *J. Stat. Phys.* **80** (1995) 69.
- [35] F. Spitzer, *Adv. Math.* **5** (1970) 246.
- [36] K.-t. Leung and R.K.P. Zia, *Drifting Spatial Structures in a System with Oppositely Charged Driven Species* (preprint, 1997).
- [37] R.K.P. Zia and B. Schmittmann, *Novel Goldstone Modes in Biased Diffusion of Two Species*, to be published.
- [38] H. Haken, *Synergetics, An Introduction* (Springer, Berlin, 3rd edition, 1983).
- [39] N. Goldenfeld, *Lectures on Phase Transitions and the Renormalization Group* (Addison-Wesley, N.Y., 1992).
- [40] M. Kosterlitz and D. Thouless, *J. Phys.* **C6** (1974) 1181.
- [41] A. D. Fokker, *Ann. Physik* **43** (1914) 810.
- [42] M. Planck, *Sitzber. Preuß. Akad. Wiss.* (1917) 324.
- [43] P. Langevin, *Comptes Rendus* **146** (1908) 530.
- [44] N. van Kampen, *Adv. Chem. Phys.* **34** (1976) 245.
- [45] B. Schmittmann, *Diploma Thesis*, 65 pp., University of Aachen, 1981
- [46] H. Risken, *The Fokker-Planck Equation* (Springer-Verlag, Berlin, 1989).
- [47] D. Beysens and M. Gbadamassi, *Phys. Rev.* **A22** (1980) 2250; H. Kiefte, M.J. Clouter and R. Penney, *Phys. Rev.* **B30** (1984) 4017; B.M. Law, P.N. Segrè, R.W. Gammon and J.V. Sengers, *Phys. Rev.* **A41** (1990) 816; P.N. Segrè, R.W. Gammon, J.V. Sengers and B.M. Law, *Phys. Rev.* **A45** (1992) 714; P.N. Segrè, R. Schmitz and J.V. Sengers, *Physica* **A195** (1993) 31.

- [48] R.K.P. Zia, K. Hwang, B. Schmittmann and K.-t Leung , *Physica* **A194** (1993) 183.
- [49] J.C. Dainty, *Laser Speckle and Related Phenomena* (Springer, Berlin, 2rd edition, 1984).
- [50] G. Korniss, B. Schmittmann and R.K.P. Zia, to appear in *Physica* **A239** (May, 1997) and accepted in *J. Phys. A*.
- [51] G. Korniss, B. Schmittmann and R.K.P. Zia, to be submitted to *Phys. Rev. E*.
- [52] M.S. Rudzinsky and R.K.P. Zia, *J. Phys.* **A29** (1996) 6717.
- [53] see e.g. G. Parisi, *Statistical Field Theory* (Addison-Wesley, N.Y., 1988).
- [54] I.S. Gradshteyn and I.M. Ryzhik, *Table of Integrals, Series and Products* (Academic Press, N.Y., 1994).

Appendix B

Momentum-space Integrals for the Correlation Functions

From eqns. (4.39) we see that we need three basic type of integrals. Although the first one is well known, for completeness we include it in this Appendix as well:

$$E(\mathbf{x}) \equiv \int \frac{d^d k}{(2\pi)^d} \frac{e^{i\mathbf{k}\mathbf{x}}}{k^2} = \frac{\Gamma\left(\frac{d}{2} - 1\right)}{4\pi^{\frac{d}{2}}} \frac{1}{r^{d-2}}, \quad (\text{B.1})$$

as it can be found in standard field theory textbooks [53]. Then it is easy to find

$$\nabla \boldsymbol{\sigma} \nabla E(\mathbf{x}) = -\sigma_{\perp} \delta(\mathbf{x}) - (\sigma_{\parallel} - \sigma_{\perp}) \frac{\Gamma\left(\frac{d}{2}\right)}{2\pi^{\frac{d}{2}}} \frac{r_{\perp}^2 - (d-1)r_{\parallel}^2}{r^{d+2}}, \quad (\text{B.2})$$

where $\boldsymbol{\sigma}$ is diagonal matrix and isotropic in the $d - 1$ dimensional transverse subspace.

B.1 A Formal Way

Next, we will show a formal way to obtain the other two momentum integrals we need. We define F_1 and F_2 as follows:

$$\begin{aligned} F_1(\mathbf{x}) &\equiv \int \frac{d^d k}{(2\pi)^d} \frac{e^{i\mathbf{k}\mathbf{x}} k^2}{k^4 + 4m^2 k_{\parallel}^2} \\ F_2(\mathbf{x}) &\equiv \int \frac{d^d k}{(2\pi)^d} \frac{e^{i\mathbf{k}\mathbf{x}} (-2m) i k_{\parallel}}{k^4 + 4m^2 k_{\parallel}^2}. \end{aligned} \quad (\text{B.3})$$

Then it is worthwhile to realize that the integrands (without the exponential) are simply the convolutions of two functions, i.e.:

$$\begin{aligned}\frac{k^2}{k^4 + 4m^2k_{\parallel}^2} &= \int \frac{d^d k'}{(2\pi)^d} F(\mathbf{k}') C(\mathbf{k} - \mathbf{k}') \\ \frac{-2m i k_{\parallel}}{k^4 + 4m^2k_{\parallel}^2} &= \int \frac{d^d k'}{(2\pi)^d} F(\mathbf{k}') S(\mathbf{k} - \mathbf{k}') ,\end{aligned}\tag{B.4}$$

where

$$\begin{aligned}F(\mathbf{k}) &= \frac{1}{k^2 + m^2} \\ C(\mathbf{k}) &= \frac{(2\pi)^d}{2} \delta(\mathbf{k}_{\perp}) \left[\delta(k_{\parallel} + im) + \delta(k_{\parallel} - im) \right] \\ S(\mathbf{k}) &= \frac{(2\pi)^d}{2} \delta(\mathbf{k}_{\perp}) \left[\delta(k_{\parallel} + im) - \delta(k_{\parallel} - im) \right] .\end{aligned}\tag{B.5}$$

The δ -functions with complex arguments should only be understood in an operational sense. What is important is that the Fourier inverse transforms of these functions are known [53] or simple:

$$\begin{aligned}F(\mathbf{x}) &= F(r) \equiv \frac{1}{(2\pi)^{\frac{d}{2}}} \left(\frac{m}{r} \right)^{\frac{d-2}{2}} K_{\frac{d-2}{2}}(mr) \\ C(\mathbf{x}) &= \cosh(mx_{\parallel}) \\ S(\mathbf{x}) &= \sinh(mx_{\parallel}) .\end{aligned}\tag{B.6}$$

Thus, using the convolution theorem, we trivially get

$$\begin{aligned}F_1(\mathbf{x}) &= \cosh(mx_{\parallel}) F(r) \\ F_2(\mathbf{x}) &= \sinh(mx_{\parallel}) F(r) .\end{aligned}\tag{B.7}$$

Note, that $F(r)$ is the solution of

$$\left(-\nabla^2 + m^2 \right) F(r) = \delta(\mathbf{x}) .\tag{B.8}$$

Then using some algebra and (B.8), we can translate $\nabla \sigma \nabla$ into differentiation with respect to x_{\parallel} :

$$\begin{aligned}\nabla \sigma \nabla F_1(\mathbf{x}) &= \\ &= -\sigma_{\perp} \delta(\mathbf{x}) + \sigma_{\perp} 2m \partial_{\parallel} \left\{ \sinh(mx_{\parallel}) F(r) \right\} + (\sigma_{\parallel} - \sigma_{\perp}) \partial_{\parallel}^2 \left\{ \cosh(mx_{\parallel}) F(r) \right\} =\end{aligned}$$

$$\begin{aligned}
& -\sigma_{\perp}\delta(\mathbf{x}) + \sigma_{\perp}2m\partial_{\parallel}F_2(\mathbf{x}) + (\sigma_{\parallel} - \sigma_{\perp})\partial_{\parallel}^2F_1(\mathbf{x}) \\
\nabla\sigma\nabla F_2(\mathbf{x}) = & \\
& \sigma_{\perp}2m\partial_{\parallel}\left\{\cosh(mx_{\parallel})F(r)\right\} + (\sigma_{\parallel} - \sigma_{\perp})\partial_{\parallel}^2\left\{\sinh(mx_{\parallel})F(r)\right\} = \\
& \sigma_{\perp}2m\partial_{\parallel}F_1(\mathbf{x}) + (\sigma_{\parallel} - \sigma_{\perp})\partial_{\parallel}^2F_2(\mathbf{x}).
\end{aligned} \tag{B.9}$$

These forms are particularly useful when we calculate the corresponding long distance behaviour.

B.2 A Rigorous Way

Finding $F_1(\mathbf{x})$:

$$F_1(\mathbf{x}) = \int \frac{d^d k}{(2\pi)^d} \frac{e^{i\mathbf{k}\mathbf{x}} k^2}{k^4 + 4m^2 k_{\parallel}^2} = \int \frac{d^{d-1} k_{\perp}}{(2\pi)^{d-1}} e^{i\mathbf{k}_{\perp}\mathbf{x}_{\perp}} \int_{-\infty}^{\infty} \frac{dk_{\parallel}}{2\pi} \frac{e^{ik_{\parallel}x_{\parallel}}(k_{\perp}^2 + k_{\parallel}^2)}{(k_{\parallel}^2 + \beta^2)(k_{\parallel}^2 + \gamma^2)}, \tag{B.10}$$

where

$$\begin{aligned}
\beta^2 &= 2m^2 + k_{\perp}^2 + 2m\sqrt{m^2 + k_{\perp}^2} \\
\gamma^2 &= 2m^2 + k_{\perp}^2 - 2m\sqrt{m^2 + k_{\perp}^2}.
\end{aligned} \tag{B.11}$$

First, using the residue theorem, we carry out the integration with respect to k_{\parallel} as implied in (B.10), which results in

$$F_1(\mathbf{x}) = \cosh(mx_{\parallel}) \int \frac{d^{d-1} k_{\perp}}{(2\pi)^{d-1}} e^{i\mathbf{k}_{\perp}\mathbf{x}_{\perp}} \frac{e^{-mr_{\parallel}u}}{2mu} \tag{B.12}$$

with

$$u \equiv \sqrt{1 + \frac{k_{\perp}^2}{m^2}}. \tag{B.13}$$

The remaining integral is axially symmetric in the $d - 1$ dimensional subspace and the integration with respect to the corresponding solid angle is well known:

$$\begin{aligned}
F_1(\mathbf{x}) = & \\
& \cosh(mx_{\parallel}) \int_0^{\infty} \frac{dk_{\perp} k_{\perp}^{d-2}}{(2\pi)^{d-1}} \frac{e^{-mr_{\parallel}u}}{2mu} \int d\Omega^{(d-1)} e^{ik_{\perp}r_{\perp}\cos\theta} = \\
& \cosh(mx_{\parallel}) \int_0^{\infty} \frac{dk_{\perp} k_{\perp}^{d-2}}{(2\pi)^{d-1}} \frac{e^{-mr_{\parallel}u}}{2mu} \frac{(2\pi)^{\frac{d-1}{2}}}{(k_{\perp}r_{\perp})^{\frac{d-3}{2}}} J_{\frac{d-3}{2}}(k_{\perp}r_{\perp}) = \\
& \frac{\cosh(mx_{\parallel})}{(2\pi)^{\frac{d-1}{2}} r_{\perp}^{\frac{d-3}{2}}} \int_0^{\infty} dk_{\perp} k_{\perp}^{\frac{d-1}{2}} \frac{e^{-mr_{\parallel}u}}{2mu} J_{\frac{d-3}{2}}(k_{\perp}r_{\perp}).
\end{aligned} \tag{B.14}$$

Defining a new variable according to (B.13), the above integral can be done [54]:

$$\begin{aligned}
F_1(\mathbf{x}) &= \\
& \frac{\cosh(mx_{\parallel})}{(2\pi)^{\frac{d-1}{2}} r_{\perp}^{\frac{d-3}{2}}} \frac{m^{\frac{d-1}{2}}}{2} \int_1^{\infty} du \left(\sqrt{u^2-1}\right)^{\frac{d-3}{2}} e^{-mr_{\parallel}u} J_{\frac{d-3}{2}}\left(mr_{\perp}\sqrt{u^2-1}\right) = \quad (\text{B.15}) \\
& \frac{\cosh(mx_{\parallel})}{(2\pi)^{\frac{d-1}{2}} r_{\perp}^{\frac{d-3}{2}}} \frac{m^{\frac{d-1}{2}}}{2} \frac{\sqrt{\frac{2}{\pi}}(mr_{\perp})^{\frac{d-3}{2}}}{\left(m\sqrt{r_{\perp}^2+r_{\parallel}^2}\right)^{\frac{d-2}{2}}} K_{\frac{d-2}{2}}\left(m\sqrt{r_{\perp}^2+r_{\parallel}^2}\right) = \cosh(mx_{\parallel}) F(r) ,
\end{aligned}$$

where $F(r)$ is obviously the same function as in (B.6).

Finding $F_2(\mathbf{x})$:

$$F_2(\mathbf{x}) = \int \frac{d^d k}{(2\pi)^d} \frac{e^{i\mathbf{k}\mathbf{x}} (-2m)ik_{\parallel}}{k^4 + 4m^2k_{\parallel}^2} = \int \frac{d^{d-1}k_{\perp}}{(2\pi)^{d-1}} e^{i\mathbf{k}_{\perp}\mathbf{x}_{\perp}} \int_{-\infty}^{\infty} \frac{dk_{\parallel}}{2\pi} \frac{e^{ik_{\parallel}x_{\parallel}} (-2m)ik_{\parallel}}{(k_{\parallel}^2 + \beta^2)(k_{\parallel}^2 + \gamma^2)} . \quad (\text{B.16})$$

Again, first carrying out the integration with respect to k_{\parallel} , using the residue theorem, yields

$$F_2(\mathbf{x}) = \sinh(mx_{\parallel}) \int \frac{d^{d-1}k_{\perp}}{(2\pi)^{d-1}} e^{i\mathbf{k}_{\perp}\mathbf{x}_{\perp}} \frac{e^{-mr_{\parallel}u}}{2mu} , \quad (\text{B.17})$$

where u is the same as defined in (B.13). Then the remaining integral in the $d-1$ dimensional subspace is exactly the same as for $F_1(\mathbf{x})$, thus, we finally obtain

$$F_2(\mathbf{x}) = \sinh(mx_{\parallel}) F(r) . \quad (\text{B.18})$$

Appendix C

Long Distance Asymptotic Behavior of the Correlation Functions

To obtain the long distance behaviour for $\nabla\sigma\nabla E(\mathbf{x})$, we just have to omit the first term in (B.2), which is a δ -function:

$$\nabla\sigma\nabla E(\mathbf{x})|_{\mathbf{x}\neq\mathbf{0}} = -(\sigma_{\parallel} - \sigma_{\perp}) \frac{\Gamma\left(\frac{d}{2}\right) r_{\perp}^2 - (d-1)r_{\parallel}^2}{2\pi^{\frac{d}{2}} r^{d+2}}. \quad (\text{C.1})$$

This is the typical "FDT-violating" power law, provided that σ is not a simple multiple of the unit matrix. Otherwise, the amplitude of this term would be zero.

Using the "large z " asymptotic expansion of the modified Bessel function [54]

$$K_{\nu}(z) \simeq \sqrt{\frac{\pi}{2z}} e^{-z} \left\{ 1 + \left(\nu^2 - \frac{1}{4} \right) \frac{1}{2z} + \mathcal{O}\left(\frac{1}{z^2}\right) \right\}, \quad (\text{C.2})$$

we can obtain the long distance behavior for $\nabla\sigma\nabla F_1(\mathbf{x})$ and $\nabla\sigma\nabla F_2(\mathbf{x})$ as $m = \text{const.} > 0$ and $r \rightarrow \infty$. Due the strong anisotropies in these functions, we consider three different scenarios:

(i.) $r_{\parallel} = 0$, $r_{\perp} \rightarrow \infty$:

Combining (B.9) and the asymptotic form of $F(r)$ (through $K_{\frac{d-2}{2}}(mr)$) we find:

$$\begin{aligned} \partial_{\parallel} F_2(\mathbf{x})|_{x_{\parallel}=0} &= mF(r)|_{x_{\parallel}=0} \simeq \frac{\sqrt{\frac{\pi}{2}}}{(2\pi)^{\frac{d}{2}}} e^{-mr_{\perp}} \left\{ \left(\frac{m}{r_{\perp}} \right)^{\frac{d-1}{2}} + \mathcal{O}\left(\frac{1}{r_{\perp}^{\frac{d+1}{2}}} \right) \right\} \\ \partial_{\parallel}^2 F_1(\mathbf{x})|_{x_{\parallel}=0} &= m^2 F(r)|_{x_{\parallel}=0} + \frac{1}{r} \frac{\partial F(r)}{\partial r} \Big|_{x_{\parallel}=0} \simeq \\ & m \frac{\sqrt{\frac{\pi}{2}}}{(2\pi)^{\frac{d}{2}}} e^{-mr_{\perp}} \left\{ \left(\frac{m}{r_{\perp}} \right)^{\frac{d-1}{2}} + \mathcal{O}\left(\frac{1}{r_{\perp}^{\frac{d+1}{2}}} \right) \right\}, \end{aligned} \quad (\text{C.3})$$

while $\partial_{\parallel} F_1(\mathbf{x})$ and $\partial_{\parallel}^2 F_2(\mathbf{x})$ are simply zero at $x_{\parallel} = 0$, since they are odd functions of x_{\parallel} . Thus, finally we have

$$\begin{aligned}\nabla\sigma\nabla F_1(\mathbf{x})|_{x_{\parallel}=0} &\simeq (\sigma_{\perp} + \sigma_{\parallel}) m \frac{\sqrt{\frac{\pi}{2}}}{(2\pi)^{\frac{d}{2}}} e^{-mr_{\perp}} \left\{ \left(\frac{m}{r_{\perp}}\right)^{\frac{d-1}{2}} + \mathcal{O}\left(\frac{1}{r_{\perp}^{\frac{d+1}{2}}}\right) \right\} \\ \nabla\sigma\nabla F_2(\mathbf{x})|_{x_{\parallel}=0} &= 0\end{aligned}\tag{C.4}$$

(ii.) $r_{\parallel} \rightarrow \infty$, $r_{\perp} \neq 0$:

In addition to the asymptotic form of $F(r)$, now we can also write $\cosh(mx_{\parallel}) \simeq \frac{1}{2}e^{mx_{\parallel}}$ and $\sinh(mx_{\parallel}) \simeq \text{sgn}(x_{\parallel})\frac{1}{2}e^{mx_{\parallel}}$. For the next set of equations, we keep the second leading power in $1/r$ for reasons to become clear when discussing the next case. We need

$$\begin{aligned}\partial_{\parallel} F_2(\mathbf{x}) &\simeq \frac{\sqrt{\frac{\pi}{2}}}{(2\pi)^{\frac{d}{2}}} \frac{e^{mr_{\parallel}}}{2} e^{-mr} \left\{ \left(1 - \frac{r_{\parallel}}{r}\right) \left(\frac{m}{r}\right)^{\frac{d-1}{2}} \right. \\ &\quad \left. + \frac{d-1}{8m^2} \left((d-3) - (d+1)\frac{r_{\parallel}}{r} \right) \left(\frac{m}{r}\right)^{\frac{d+1}{2}} + \mathcal{O}\left(\frac{1}{r^{\frac{d+3}{2}}}\right) \right\} \\ \partial_{\parallel}^2 F_1(\mathbf{x}) &\simeq m \frac{\sqrt{\frac{\pi}{2}}}{(2\pi)^{\frac{d}{2}}} \frac{e^{mr_{\parallel}}}{2} e^{-mr} \left\{ \left(1 - \frac{r_{\parallel}}{r}\right)^2 \left(\frac{m}{r}\right)^{\frac{d-1}{2}} \right. \\ &\quad \left. + \frac{d+1}{8m^2} \left((d-5) - 2(d-1)\frac{r_{\parallel}}{r} + (d+3)\frac{r_{\parallel}^2}{r^2} \right) \left(\frac{m}{r}\right)^{\frac{d+1}{2}} + \mathcal{O}\left(\frac{1}{r^{\frac{d+3}{2}}}\right) \right\} \\ \partial_{\parallel} F_1(\mathbf{x}) &\simeq \text{sgn}(x_{\parallel}) \partial_{\parallel} F_2(\mathbf{x}) \\ \partial_{\parallel}^2 F_2(\mathbf{x}) &\simeq \text{sgn}(x_{\parallel}) \partial_{\parallel}^2 F_1(\mathbf{x}).\end{aligned}\tag{C.5}$$

Thus, when indeed $r_{\perp} \neq 0$, in leading order, we have

$$\begin{aligned}\nabla\sigma\nabla F_1(\mathbf{x}) &\simeq m \frac{\sqrt{\frac{\pi}{2}}}{(2\pi)^{\frac{d}{2}}} \frac{e^{mr_{\parallel}}}{2} e^{-mr} \left\{ \left((\sigma_{\perp} + \sigma_{\parallel}) - 2\sigma_{\parallel} \frac{r_{\parallel}}{r} + (\sigma_{\parallel} - \sigma_{\perp}) \frac{r_{\parallel}^2}{r^2} \right) \left(\frac{m}{r}\right)^{\frac{d-1}{2}} \right. \\ &\quad \left. + \mathcal{O}\left(\frac{1}{r^{\frac{d+1}{2}}}\right) \right\} \\ \nabla\sigma\nabla F_2(\mathbf{x}) &\simeq \text{sgn}(x_{\parallel}) \nabla\sigma\nabla F_1(\mathbf{x}).\end{aligned}\tag{C.6}$$

(iii.) $r_{\parallel} \rightarrow \infty$, $r_{\perp} = 0$:

When deriving formulas for the previous case, the only thing we exploited was that $r_{\parallel} \rightarrow \infty$. Setting $r_{\perp} = 0$ has two important consequences: since now $r = r_{\parallel}$, the exponential decays cancel, and also the amplitude of the $(1/r)^{\frac{d-1}{2}}$ term will vanish (that was the reason for

keeping powers up to next leading order in (C.5)). Thus,

$$\begin{aligned}
\nabla \boldsymbol{\sigma} \nabla F_1(\mathbf{x})|_{r_\perp=0} &\simeq -\sigma_\perp \frac{\sqrt{\frac{\pi}{2}}}{(2\pi)^{\frac{d}{2}}} \left\{ \frac{d-1}{2m} \left(\frac{m}{r_\parallel} \right)^{\frac{d+1}{2}} + \mathcal{O} \left(\frac{1}{r_\parallel^{\frac{d+3}{2}}} \right) \right\} \\
\nabla \boldsymbol{\sigma} \nabla F_2(\mathbf{x})|_{r_\perp=0} &\simeq \text{sgn}(x_\parallel) \nabla \boldsymbol{\sigma} \nabla F_1(\mathbf{x})|_{r_\perp=0} .
\end{aligned} \tag{C.7}$$

Appendix D

A Special Determinant

We want to find the determinant of $(\delta_{ij} + a_i b_j + c_i d_j)$ where the Kronecker-symbol represents an $N \times N$ unit matrix and a_i, b_i, c_i, d_i are N -component vectors (N is arbitrary). From the definition of the determinant, it is

$$\begin{aligned} \det(\delta_{ij} + a_i b_j + c_i d_j) = & \\ & \epsilon^{i_1 i_2 \dots i_N} (\delta_{1i_1} + a_{1i_1} b_{1i_1} + c_{1i_1} d_{1i_1}) (\delta_{2i_2} + a_{2i_2} b_{2i_2} + c_{2i_2} d_{2i_2}) \dots \\ & \dots (\delta_{Ni_N} + a_{Ni_N} b_{Ni_N} + c_{Ni_N} d_{Ni_N}) , \end{aligned} \quad (\text{D.1})$$

where summation over repeated indices is implied and $\epsilon^{i_1 i_2 \dots i_N}$ is the fully antisymmetric unit matrix, i.e.,

$$\epsilon^{i_1 i_2 \dots i_N} = \begin{cases} +1 & \text{if } (i_1, i_2, \dots, i_N) \text{ is an even permutation of } (1, 2, \dots, N) \\ -1 & \text{if } (i_1, i_2, \dots, i_N) \text{ is an odd permutation of } (1, 2, \dots, N) \\ 0 & \text{otherwise} \end{cases} . \quad (\text{D.2})$$

First, before the summation is taken over i_1, i_2, \dots, i_N , we multiply each term by each term among the different parentheses on the right hand side of (D.1), which yields 3^N terms. If two or more of the ‘‘same pair’’ is chosen, e.g. $\dots a_k b_{i_k} \dots a_l b_{i_l} \dots$, where \dots ’s can be any possible combination of ab ’s, cd ’s or the δ ’s, and perform the summation over i_k, i_l , it yields:

$$\epsilon^{i_1 \dots i_k \dots i_l \dots i_N} \dots a_k b_{i_k} \dots a_l b_{i_l} \dots = 0 . \quad (\text{D.3})$$

since $b_{i_k} b_{i_l}$ is symmetric, while $\epsilon^{i_1 i_2 \dots i_N}$ is antisymmetric in all pairs of indices. When we pick 3 or more ab ’s or cd ’s and $N - 3$ or less δ ’s, there will always be a symmetric bb or dd pair in the product, yielding zero. Thus, we only have to consider three cases, namely the ones with N , $N - 1$, and $N - 2$ δ ’s. When we chose N δ ’s it is trivial:

$$\epsilon^{i_1 i_2 \dots i_N} \delta_{1i_1} \delta_{2i_2} \dots \delta_{Ni_N} = \epsilon^{12 \dots N} = 1 . \quad (\text{D.4})$$

There are N different cases with $N - 1$ δ 's and we have to sum over them explicitly:

$$\begin{aligned} & \sum_k \epsilon^{i_1 \dots i_{k-1} i_k i_{k+1} \dots i_N} \delta_{1i_1} \dots \delta_{k-1 i_{k-1}} (a_k b_{i_k} + c_k d_{i_k}) \delta_{k+1 i_{k+1}} \dots \delta_{Ni_N} = \\ & \sum_k \epsilon^{1 \dots k-1 i_k k+1 \dots N} (a_k b_{i_k} + c_k d_{i_k}) = \sum_k (a_k b_k + c_k d_k) = (a_k b_k + c_k d_k) . \end{aligned} \quad (\text{D.5})$$

Similarly, there are $N(N - 1)/2$ cases with $N - 2$ δ 's:

$$\begin{aligned} & \sum_k \sum_{m>k} \epsilon^{i_1 \dots i_k \dots i_l \dots i_m \dots i_N} \delta_{1i_1} \dots (a_k b_{i_k} + c_k d_{i_k}) \dots \delta_{li_l} \dots (a_m b_{i_m} + c_m d_{i_m}) \dots \delta_{Ni_N} = \\ & \sum_k \sum_{m>k} \epsilon^{1 \dots i_k \dots l \dots i_m \dots N} (a_k b_{i_k} + c_k d_{i_k}) (a_m b_{i_m} + c_m d_{i_m}) = \\ & \sum_k \sum_{m>k} \epsilon^{1 \dots i_k \dots l \dots i_m \dots N} (a_k b_{i_k} a_m b_{i_m} + c_k d_{i_k} c_m d_{i_m}) + \\ & \qquad \qquad \qquad \sum_k \sum_{m>k} \epsilon^{1 \dots i_k \dots l \dots i_m \dots N} (a_k b_{i_k} c_m d_{i_m} + c_k d_{i_k} a_m b_{i_m}) = \quad (\text{D.6}) \\ & 0 + \sum_k \sum_{m>k} \epsilon^{1 \dots i_k \dots l \dots i_m \dots N} (a_k b_{i_k} c_m d_{i_m} + c_k d_{i_k} a_m b_{i_m}) = \\ & \sum_k \sum_{m>k} (a_k b_k c_m d_m - a_k b_m c_m d_k + c_k d_k a_m b_m - c_k d_m a_m b_k) = \\ & \sum_{k,m} [(a_k b_k)(c_m d_m) - (a_k d_k)(b_m c_m)] = (a_k b_k)(c_m d_m) - (a_k d_k)(b_m c_m) . \end{aligned}$$

Finally, combining (D.4), (D.5) and (D.6) we have

$$\det(\delta_{ij} + a_i b_j + c_i d_j) = 1 + [a_i b_i + c_i d_i] + [(a_i b_i)(c_j d_j) - (a_i d_i)(b_j c_j)] . \quad (\text{D.7})$$

Vita

György Korniss

Personal Data:

Date of Birth: January 14, 1969
Place of Birth: Budapest, Hungary

Education:

1993-97 Ph.D. in Physics, Virginia Tech, Blacksburg, VA
1989-93 Diploma (M.S.) in Physics, Eötvös Loránd University, Budapest, Hungary
1988-89 Physics Major at Kossuth Lajos University, Debrecen, Hungary

Experience:

1994-97 Graduate Research Assistant, Virginia Tech
1993-96 Graduate Teaching Assistant, Virginia Tech
1992-93 Diploma Research Assistant, Central Research Institute
for Physics, Budapest, Hungary

Research Interest:

Statistical Mechanics of Non-equilibrium Systems
One Dimensional Quantum Spin Systems